WIDE AREA DIFFERENTIAL OPERATION OF THE GLOBAL POSITIONING SYSTEM : EPHEMERIS AND CLOCK ALGORITHMS

A DISSERTATION

SUBMITTED TO THE DEPARTMENT OF MECHANICAL ENGINEERING

AND THE COMMITTEE ON GRADUATE STUDIES

OF STANFORD UNIVERSITY

IN PARTIAL FULFILLMENT OF THE REQUIREMENTS

FOR THE DEGREE OF

DOCTOR OF PHILOSOPHY

By

Yeou-Jyh Tsai

August 1999

I certify that I have read this dissertation and that in my opinion it is fully adequate, in scope and quality, as a dissertation for the degree of Doctor of Philosophy.

Per K. Enge
(Principal Advisor)

I certify that I have read this dissertation and that in my opinion it is fully adequate, in scope and quality, as a dissertation for the degree of Doctor of Philosophy.

Daniel B. DeBra

I certify that I have read this dissertation and that in my opinion it is fully adequate, in scope and quality, as a dissertation for the degree of Doctor of Philosophy.

J. David Powell

I certify that I have read this dissertation and that in my opinion it is fully adequate, in scope and quality, as a dissertation for the degree of Doctor of Philosophy.

Todd Walter

Approved for the University Committee on Graduate Studies:

Abstract

The Global Positioning System (GPS) provides great potential benefit for commercial aviation because of its low-cost and seamless navigation. While accuracy requirements can be achieved, several technical challenges have to be resolved in order to use GPS as the primary navigation system. Among them, the stringent requirements for integrity, availability and continuity of service have demanded a new level of GPS navigation performance.

The Wide Area Augmentation System (WAAS) is being deployed by the Federal Aviation Administration (FAA) to augment GPS. WAAS will aid GPS with the following three services. First, WAAS uses nationwide ground reference stations to monitor the health of all satellites over the national airspace system (NAS) and flag situations which may cause an integrity threat to flight safety. Secondly, WAAS uses the ground network to generate vector differential corrections which will improve navigation accuracy. Thirdly, it uses geostationary satellite(s) to broadcast differential corrections and integrity flags at the GPS L_1 frequency. These ranging signals will be combined with the GPS ranging signals to improve time availability and continuity of service.

This research work describes the ephemeris and clock algorithms which generate the differential corrections and their confidence values. These corrections and

user differential range error (UDRE) estimates are capable of achieving accuracy requirements for Category I precision approach. Furthermore, integrity monitoring algorithms are implemented to examine navigation performance under system failure modes. This work shows that navigation performance (accuracy, availability and integrity) can be maintained even in the presence of some specific failures we examined. This robustness is demonstrated using real data and simulations.

Acknowledgments

I would like to thank my advisor, Professor Per K. Enge, for giving me the opportunity to pursue this research and for guiding me through it. His comprehensive knowledge and clear guidance not only made this thesis possible, but also educated me in conducting research in general. His insight and enthusiasm had always inspired me through the difficult part of this research. I will always be grateful for the wonderful student-faculty relationship.

I would also like to thank my defense and reading committee, including Professor Daniel B. DeBra, Professor J. David Powell and Dr. Todd Walter. Professor DeBra, my academic advisor in the Mechanical Engineering department, had offered great help in my academic life. Professor Powell generously offered his Piper Dakota for the flight tests described in this dissertation and was our pilot! Dr. Walter, manager of the Wide Area Differential GPS Laboratory, provided many valuable instructions and discussions. Special thanks go to Professor Bradford Parkinson for creating the excellent GPS research environments at Stanford.

I would like to thank research associates and graduate students at the Stanford WADGPS Laboratory for their assistance and encouragement throughout my research, especially Dr. Changdon Kee and Dr. YC Chao. I would like to express my gratitude to the fellow graduate students: Jennifer Evans, Awele Ndili, Andrew

Barrows, Jock Christie, Andrew Hansen, Donghai Dai, Ping-Ya Ko, Keith Alter and Rich Fuller.

Thanks are also due to the Ministry of Education in Taiwan, Republic of China, for supporting my first three years of study at Stanford. The U.S. Federal Aviation Administration research grant supported Stanford WAAS research. I gratefully acknowledge the support and assistance of the FAA Satellite Program Office, FAA Technical Center and FAA personnel at Arcata, CA, Elko, NV and San Diego, CA.

Last but not least, I would like to thank my parents for the support and understanding they have given me during my doctoral studies at Stanford and throughout my academic life.

Contents

List of Tables

List of Figures

Chapter 1

Introduction

The Global Positioning System (GPS) will revolutionize aircraft navigation. While GPS alone can and has been used as the primary means of navigation service for en-route, terminal and non-precision approach phases of flight, augmentation is still necessary to meet stringent performance requirements on availability, accuracy and integrity. The Wide Area Augmentation System (WAAS), currently being implemented by the Federal Aviation Administration (FAA), is aimed at providing seamless navigation guidance for all phases of flight down to the Category I decision height of 200 feet.

The general goal of this research is to design, develop and demonstrate the capability of the WAAS to provide seamless navigation for all phases of flight down to this Category I decision height. The specific focus is to design and develop the ephemeris and clock estimation algorithms that provide the required accuracy and integrity performance for the WAAS. These algorithms also need to perform well when the system experiences GPS and WAAS degradations or component failures.

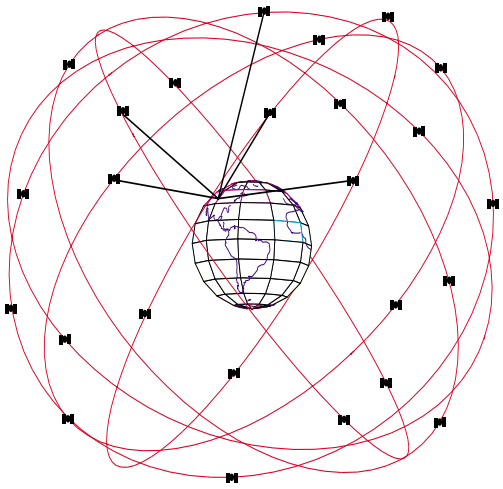

Figure 1.1: The Global Positioning System (GPS)

1.1 The Global Positioning System

The Global Positioning System, developed and implemented by the Department of Defense (DOD), is a passive satellite ranging system. GPS provides continuous, all-weather and global coverage with a constellation of 24 space vehicles (Figure 1.1) [AIAAGPS] [Kaplan].

The Global Positioning System became fully operational in 1995. GPS is composed of three segments:

1. Space segment: The system is designed to operate with 24 (three active spares) satellites on six orbital planes with a period of about 12 hours to provide three dimensional, 24 hour coverage. Actually, the number of satellites may vary. Currently there are 27 satellites on orbit.

2. Control segment: Five global monitoring stations are used to determine the satellite ephemerides and clock offsets, upload navigation messages, and monitor the health of the satellites.

3. User segment: Current user applications include surveying, land vehicle and aircraft navigation. Future use will only be limited by our imagination.

GPS, initially designed for military use, provides two different services. The Precise Positioning Service (PPS), is available only to users authorized by the U.S. Department of Defense. The Standard Positioning Service (SPS), instead, is available to all civilian users. The SPS signals are intentionally degraded through a dithering of the satellite clocks, where this dithering is known as Selective Availability (SA). Although SA on satellite ephemeris can be implemented, it has not been observed yet.

The GPS signal consists of two components, L_1 at a center frequency of 1575.42 MHz and L_2 at a center frequency of 1227.60 MHz. The L_1 signal is modulated by both a 10.23 MHz clock rate precision P/Y code and by a 1.023 MHz clock rate C/A code to be used by the civil users [Spilker,a].

Each C/A code chip is approximately 293 meters long while each cycle of the L_1 carrier frequency is about 19 cm long. These are the features of the GPS signals which GPS receivers measure. Typically, a good receiver can measure either feature with a precision of a fraction of one percent. Therefore, positioning using carrier phase measurements will be much more precise than positioning using code phase measurements [Lawrence] [Pervan]. However, real-time systems rarely use carrier-phase navigation because of the problem of carrier cycle ambiguity (see Chapter 2).

The Global Positioning System provides great potential benefit for commercial

aviation because it provides low-cost and seamless navigation. With the SPS service, the vertical accuracy is about 156 meters, 95 percent of the time [SPS]. GPS is now being used for en-route, terminal and non-precision approach phases of flight (for aircraft with Class B3 and Class C3 equipment) [TSOC129a] when the airborne equipment can provide a level of GPS integrity equivalent to that provided by Receiver Autonomous Integrity Monitoring (RAIM). In addition, GPS is also being used worldwide for Visual Flight Rules (VFR) navigation extensively. While GPS has already been used as the primary navigation sensor for en-route, terminal and non-precision approach, its level of accuracy and availability is far from being acceptable for precision approach.

Although accuracy requirements can be achieved by augmenting GPS, several additional technical challenges must be resolved to use GPS as the primary navigation system for all phases of flight. Among them, the stringent requirements for integrity, availability and continuity of service demand a new level of GPS navigation performance. These requirements will be described in the next section.

1.2 Required Navigation Performance

The FAA's objective of using GPS is to provide enhanced service and to reduce infrastructure cost for aircraft navigation. To be used as a primary-means navigation system, the Required Navigation Performance (RNP) for integrity, availability, accuracy and continuity must be met [Kelly]. Required Navigation Performance is a measure of the navigation system performance within a defined airspace, route, or procedure, including the operating parameters of the navigation systems used within that airspace. Primary means of navigation refers to the capability of planning an

operation around scheduled outages so that the system is available for a particular flight and the operational continuity, availability and accuracy requirements are met [MOPS]. The four parameters for the RNP are defined below.

1. Accuracy: The degree of conformance between the estimated or measured position and/or velocity of a platform at a given time and its true position and/or velocity.

2. Integrity: The ability of a navigation system to provide timely warnings to users when the system should not be used for navigation. Values stated are the probability that a system does "not" have integrity.

3. Continuity: The probability that the signal supports navigation accuracy and integrity requirements for the duration of the intended operation (approach or landing), given that the capability was available at the beginning of the operation. The continuity requirement is expressed as a loss of continuity per unit of time.

4. Availability: The probability that the navigation and fault detection functions are operational and that the signal accuracy, integrity, and continuity of function requirements are met. This is typically expressed as a fraction of time.

Precision landing systems are separated into three categories of operations, based on the cloud ceiling (decision height, DH) and runway visibility. Table 1.1 details the navigation performance required for each category of precision landing [JHU]. This table shows International Civil Aviation Organization (ICAO) threshold and objective requirements and the acceptable values for the Continental United States (CONUS). Vertical accuracy is the 95-percent vertical navigation error and Vertical

Alert Limit (VAL) is the vertical position error alert limit. Once the decision height is reached, the landing must continue by visual means, otherwise a missed approach is executed.

Operation Category	Vertical Accuracy	Integrity (per approach)	Vertical Alert Limit	Continuity	Availability
I	7.7 m	$2x10^{-7}$	10-15 m	$5x10^{-5}$/approach	0.99999
II	2.0 m	$2x10^{-9}$	5.3 m	$4x10^{-6}$/15 sec	0.99999
III	2.0 m	$2x10^{-9}$	5.3 m	$1x10^{-7}$/15 sec	0.99999

Table 1.1: NAS Performance Requirements

The goal of the WAAS is to provide seamless navigation guidance for all phases of flight down to the Category I decision height of 200 feet. WAAS is not capable of meeting Category II or Category III requirements. For those operations, the FAA is developing a Local Area Augmentation System (LAAS) [Swider].

1.3 Differential GPS

Some GPS augmentations use ground reference station(s) to provide *differential* corrections which cancel the errors in GPS signals. Accuracy is obtained by reducing the errors in the GPS measurements. The application of differential GPS (DGPS) also improves integrity compared to "stand-alone" GPS positioning.

There are two types of differential GPS approaches, local area DGPS (LADGPS) and wide area DGPS (WADGPS), and these are now discussed.

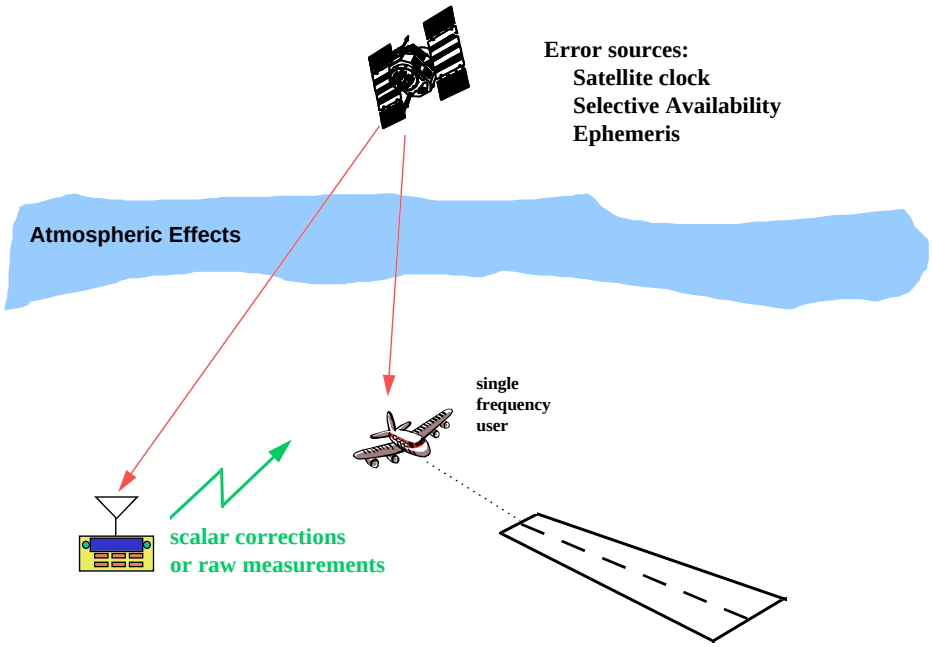

Figure 1.2: Local Area Differential GPS

1.3.1 Local Area Differential GPS

A local area differential GPS (LADGPS) system uses only one ground reference station and transmits either scalar corrections or raw measurements to the near-by users. Because the users are close to the reference station, common mode errors can be canceled and better accuracy can be achieved [Chou].

The basic idea is shown in Figure 1.2. The location of the reference receiver is precisely surveyed. LADGPS broadcasts either corrections or raw measurements from the ground reference receiver to its users via any suitable data link. Typically, UHF or VHF is used. Because LADGPS is trying to cancel the common mode errors for the reference station and the user, accuracy depends on their separation. As the user moves away from the LADGPS reference station, spatial decorrelation in the ephemeris errors, tropospheric and ionospheric errors cause accuracy degradation.

Depending on the accuracy requirements, either a code-phase DGPS or a carrier-phase DGPS can be implemented. Achieved accuracy ranges from a few meters for a code-phase DGPS system to several centimeters for a carrier-phase DGPS system. Several carrier-phase DGPS techniques for aircraft precision landing have been demonstrated [Lawrence] [Pervan].

Approximately 100 U.S. airports nationwide require either Category II or Category III landing guidance. The LADGPS system is capable of providing the required accuracy and integrity for all three categories of precision landing. Consequently, the FAA is developing a LADGPS called local area augmentation system for such applications [Swider].

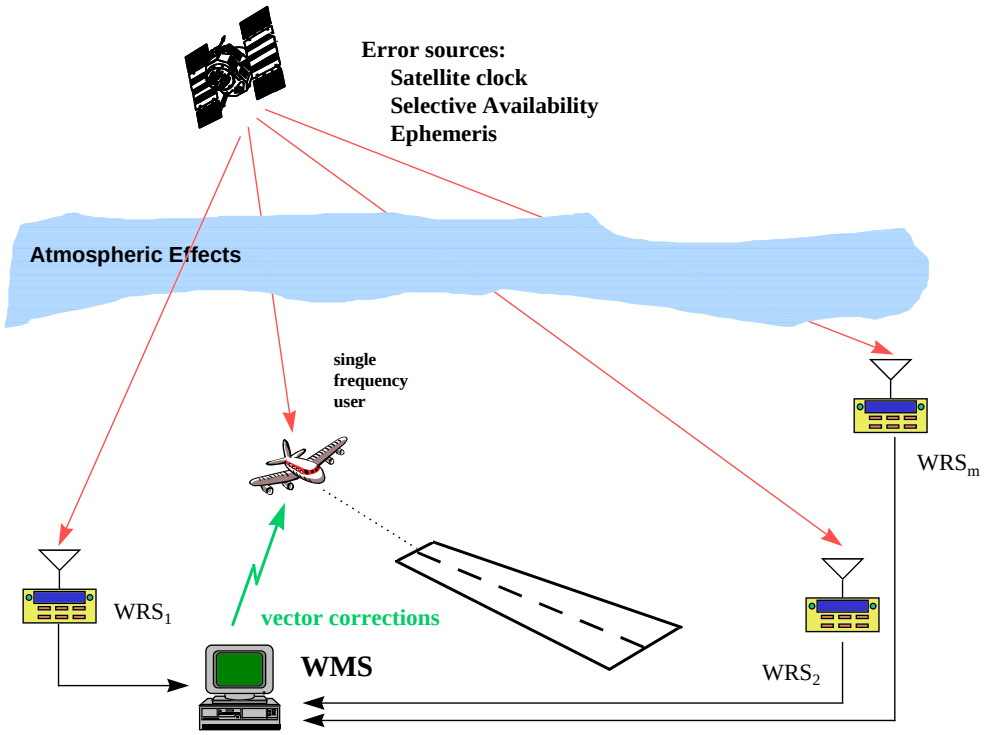

Figure 1.3: Wide Area Differential GPS

1.3.2 Wide Area Differential GPS

Approximately 1000 runways in the U.S. currently have an Instrument Landing System (ILS) Category I facility. While LAAS can provide the nationwide Category I capability, it would require implementation at all 1000 Category I airports. Such a widespread deployment would be difficult to procure, operate and maintain. A cost effective alternative is the wide area differential GPS.

As developed by Dr. Kee and Prof. Parkinson at Stanford University [Kee,a], the wide area differential GPS approach uses multiple ground reference stations to monitor GPS satellites and generate vector corrections which include satellite clock errors, satellite ephemeris errors and ionospheric delays (Figure 1.3). Because of these vector corrections, WADGPS users will not suffer the spatial decorrelation problem characteristic of LADGPS. Approximately two meter accuracy (95%) can be achieved over continental areas. The WADGPS provides a cost effective design to serve Category I landing guidance because only about 20 reference stations are necessary to serve the entire continental United States.

The Wide Area Augmentation System, an extension of the WADGPS concept, is being deployed by the FAA. It is a safety critical system consisting of a ground network of reference and integrity monitoring data processing sites to assess current GPS performance, as well as a space segment which broadcasts that assessment to its users. The operational goals of the WAAS are to augment the Department of Defense GPS SPS so that GPS/WAAS is the only radionavigation equipment required onboard the aircraft to meet aviation radionavigation performance requirements for oceanic, remote area and domestic en-route, terminal, non-precision, and Category I precision phases of flight [MOPS].

The WAAS signal provides the augmentation to GPS to obtain the required accuracy improvement for precision approaches, as well as integrity, continuity, and availability of navigation for all phases of flight. Within the service volume, the level of service will be dependent on the user's equipment. The WAAS will augment GPS in three ways:

1. Vector corrections will increase accuracy.
2. Confidence bounds and "use/don't use" messages will enhance integrity.
3. An additional ranging signal-in-space will augment the availability and continuity.

The vector corrections include the satellite ephemeris and clock errors for observed GPS satellites, and a grid of vertical ionospheric delays. Confidence indexes will also be generated along with the corrections to enhance integrity and provide the weighting factors for the user's navigation solution computation. A detailed description of a prototype WAAS will be given in Chapter 2.

1.4 Problem Statement

WADGPS should be a cost effective approach to provide adequate accuracy for all phases of flight down to a Category I decision height. However, several issues still require investigation. These include:

WAAS Bandwidth Constraints The WAAS was designed to separate the error components in the GPS ranging signals. These errors include satellite ephemeris errors, satellite clock errors and errors caused by the ionosphere. The WAAS data

link has to broadcast corrections for all GPS satellites in orbit and corrections for predefined ionospheric grids with a data rate of only 250 bits per second [Enge,c]. Greater bit rates would require the received signal power from the geostationary WAAS satellites to be greater than the received power from the GPS satellites - an undesirable outcome. In addition, the magnitudes of the generated corrections have to be constrained such that they can not be arbitrarily large [MOPS]. Can the WAAS meet the RNP with this bandwidth limitation?

Category I Accuracy Requirements In addition to the bandwidth constraints, data quantization and latency also affect accuracy and integrity. These limitations also need to be studied to verify that Category I accuracy can be achieved with WAAS.

Integrity Monitoring Detection and isolation of WAAS component failures are even more important than accuracy. Detection of failures in the WAAS is necessary to provide timely warnings and integrity for the users while successful isolation of failures guarantees continuous navigation service.

1.5 Previous Work

1.5.1 Geometeric Ephemeris Error Estimator

Parkinson and Kee pioneered the research of the wide area differential GPS in 1990. They used a full state approach to estimate and separate the satellite's error components [Kee,a] [Kee,b]. Their approach solves for the satellite ephemeris errors, satellite clock errors and reference station clock errors simultaneously with a least-squares estimator. This approach is computationally intense because all satellites

are processed with a single large matrix inversion. While groundbreaking, this early study did not consider the bandwidth limitation or the impact of data latency due to message broadcast. Their approach does separate the fast and slow error components as required to meet the bandwidth limitation [Chao,d]. Using this approach, both satellite ephemeris errors and satellite clock errors have to be sent as fast corrections.

The WADGPS is capable of providing an accuracy level similar to traditional DGPS systems over a wide area. The accuracy has been demonstrated using collected data [Kee,c] and simulation [Pullen]. Simulation studies have shown that geometric ephemeris error estimators can achieve the required Category I precision approach accuracy [Enge,a] [Pullen].

1.5.2 Dynamic Ephemeris Estimation

The International GPS Service for Geodynamics (IGS) organization regularly provides post-processed precise GPS orbits with observation data collected using its global monitoring network [IGS]. Approximately 24 hours of data is required to reconstruct the satellite's orbit. A precise yet complicated satellite dynamic model is necessary [Colombo] [Litchen] [Pogorelc].

This dynamic approach uses carrier phase as the measurements and therefore must resolve the phase ambiguity. Accuracy for the generated orbit is claimed to be better than one meter in all three directions (radial, along-track and cross-track) [Litchen]. This accuracy degrades if the monitoring network is not global [Ceva].

The dynamic model improves accuracy in the ephemeris error estimates and is capable of real time operation [JPL]. However, the processing is complicated because the dynamic model is complex and cycle ambiguity resolution is required. In addition,

integrity monitoring capability has not been well understood with the dynamic approach. Raytheon Systems Company, FAA's WAAS contractor, is using the dynamic model approach.

1.5.3 Flight Trials

The FAA has been pursuing the WAAS as a precision landing system down to Category I decision height. The FAA Technical Center (FAATC) has established the test bed for the development and testing of augmentation to GPS. A cross-country flight test in December of 1993 demonstrated near seamless operation from Atlantic City, NJ to Crows Landing, CA [Wullschleger].

The flight test was the first of its kind to demonstrate a continuous WAAS data link coverage during a coast to coast flight. However, lumped clock and ephemeris corrections were broadcast (fast messages only) instead of separating clock and ephemeris corrections into fast and slow messages.

1.6 Thesis Contributions

The main goal of the Stanford WADGPS research is to design and prototype a WAAS system that meets Category I precision approach requirements. This requires a complete implementation of the WAAS ground algorithms and avionics processing algorithms.

This dissertation contributes in the following specific areas.

1.6.1 Snapshot Ephemeris Error Estimation

With the inverse geometry approach employed in the past, neither the least-squares (LS) nor weighted least-squares (WLS) methods can provide a reasonable estimate for the ephemeris errors when the system becomes over-determined. I incorporate the *a priori* information of the ephemeris errors and use a minimum-variance estimator to overcome this problem. This approach can be used whether the system is under-determined or over-determined. Generated ephemeris error estimates fit into the 250 bps WAAS message. These error corrections provide the required accuracy.

1.6.2 Ephemeris And Clock Algorithms

I devised the real time ephemeris and clock algorithms which not only provide separation of fast and slow error components but also provide smoothed estimates of the ephemeris and clock errors. In addition, confidence estimates of these corrections are generated. The error corrections and confidence estimates can be broadcast within 250 bps data rate.

A simple kinematic model is used for the satellite ephemeris errors. The achieved user navigation performance is nearly equivalent to that using a more complicated dynamic model to estimate the ephemeris errors.

1.6.3 UDRE Estimation

I also designed and implemented algorithms to generate the User Differential Range Error (UDRE) estimates together with the ephemeris/clock error estimates. The UDRE are quantized to a discrete UDRE indicator (UDREI) and sent to the users. Users rely on these values for integrity and their weighted least-squares position fix.

WAAS not only provides wide-area differential corrections for improved positioning accuracy but also provides bounds on the positioning error. In the vertical direction, it is the Vertical Protection Limit (VPL) which allows users to verify the integrity of the corrections and of their own measurements. The quantized UDRE estimates are incorporated by the users to compute the VPL.

1.6.4 Category I Accuracy Demonstration

The Stanford WAAS team is the first to demonstrate that Category I accuracy can be achieved both for static users and in dynamic flight trials using the prototype WAAS. As part of this effort, I developed the original WAAS message scheduling, message packing and unpacking, as well as the navigation software for our airborne user.

1.6.5 Integrity Monitoring

I investigated prototype WAAS performance in the presence of GPS and WAAS degradations. The WAAS, with a network of ground reference stations, is responsible for providing integrity data for monitored satellites. To understand better the effect of GPS and WAAS degradations, I investigated the following two fault modes:

- GPS space segment degradations, which include satellite ephemeris and satellite clock problems.
- WAAS ground segment degradations, which involve receiver clock drifts. Master clock degradations have a very different effect than any other reference clock failures. Therefore, they are studied separately.

Detecting and isolating outlying measurement(s) significantly increases computation load for the master station because computation using subsets of the measurements

and statistical hypothesis testing have to be executed. To reduce the computational burden, I derived the general formula for measurement downdating which gives the relationship between the estimate using *all* measurements versus the estimate using *subsets* of the measurements.

1.6.6 Prototype WAAS Performance Under Failures

Throughout this thesis, faulted performance will refer to prototype WAAS performance in the presence of the various signal and clock degradations described above. I have evaluated faulted performance using both real data with maneuvering satellites and real data with overlaid simulated failures. I have demonstrated that even with these failures, my algorithms are capable of maintaining required performance for integrity, availability and accuracy. Other possible integrity threats, such as WMS software bugs, have not been investigated.

1.7 Thesis Outline

Chapter 2 describes the details of the a prototype Wide Area Augmentation System, including its reference stations and master stations. Stanford WAAS research starts with three reference stations on the west coast. The National Satellite Test Bed (NSTB), a prototype WAAS with more than 20 reference stations, is maintained by the FAA. Measurement pre-processing algorithms are described, which include master clock estimation and common view time transfer. This pre-processing generates the measurements required for ephemeris and clock error estimation algorithms. Developed algorithms and the results presented throughout this dissertation are referred to either our 3-station WAAS system or the NSTB prototype system. Raytheon Systems

Company is also building a WAAS system under the contract with the FAA.

Chapter 3 describes the ephemeris algorithms, which include snapshot and sequential filtering approaches to generate ephemeris error estimates. Studies of ephemeris failures are presented for real data with maneuvering satellites to demonstrate that the implemented algorithms detect the failure, flag the troublesome satellite as "don't use" and isolate the outlying measurements so that they do not corrupt the correction generation algorithms.

Chapter 4 details the satellite clock algorithms, which also include snapshot and sequential filtering approaches. It also describes the generation of the user differential range error (UDRE) estimate, which provides confidence estimates of the combined WAAS ephemeris and clock error corrections. Detection and isolation of satellite clock failures are also described with results from simulations.

Chapter 5 presents the navigation performance in terms of three RNP parameters: integrity, availability and accuracy. The results will include both static and dynamic users. Fault-free performance results using real data will be presented first, followed by faulted performance results which used real data containing maneuvering satellites, simulated satellite clock failures and simulated reference station clock failures. Comparisons of fault-free and faulted performance results are given to demonstrate the robustness of the implemented algorithms to system component failures.

Chapter 6 summarizes the accomplished work and provides some thoughts on the direction for future research.

Chapter 2

A Prototype Wide Area Augmentation System

2.1 Introduction

GPS is already providing great benefits to aviation users, but compared to its potential, these benefits are just the beginning. The contributions of GPS to aviation promise to be revolutionary. With air traffic nearly doubling by the turn of the century, GPS can be the basis for the future air traffic management (ATM) system which will maintain high levels of safety and increase airway capacity while reducing delays. The objective of the Federal Aviation Administration (FAA) is to establish and maintain a satellite based navigation capability for all phases of flight.

The Wide Area Augmentation System (WAAS) is being deployed by the FAA to augment GPS. The WAAS will aid GPS with the following three services. First, the WAAS (Figure 2.1) uses nationwide ground reference stations to monitor the health of all satellites over the National Airspace System (NAS) and flag situations which may

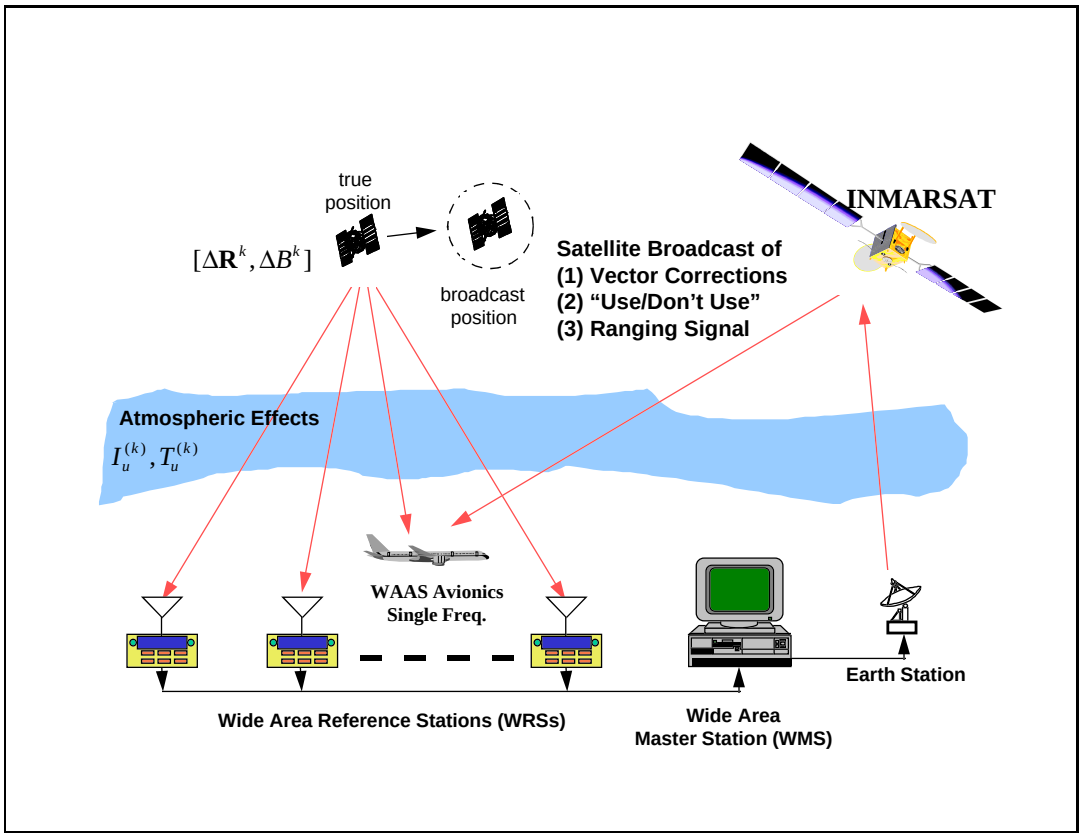

Figure 2.1: Wide Area Augmentation System

cause an integrity threat to flight safety. Second, the WAAS uses the ground network to generate vector differential corrections and associated error bounds which will improve navigation accuracy and integrity. Third, it uses geostationary satellite(s) to broadcast differential corrections and integrity flags at the GPS L_1 frequency. These ranging signals will be combined with the GPS ranging signals to improve time availability and continuity of service.

The prototype WAAS is the National Satellite Test Bed (NSTB), implemented by the FAA (Figure 2.2). The NSTB has three experimental master stations and two uplink stations. The NSTB includes 18 reference stations throughout the Continental U.S., 3 reference stations in Canada, 5 in Alaska and 2 in Hawaii. More testbed

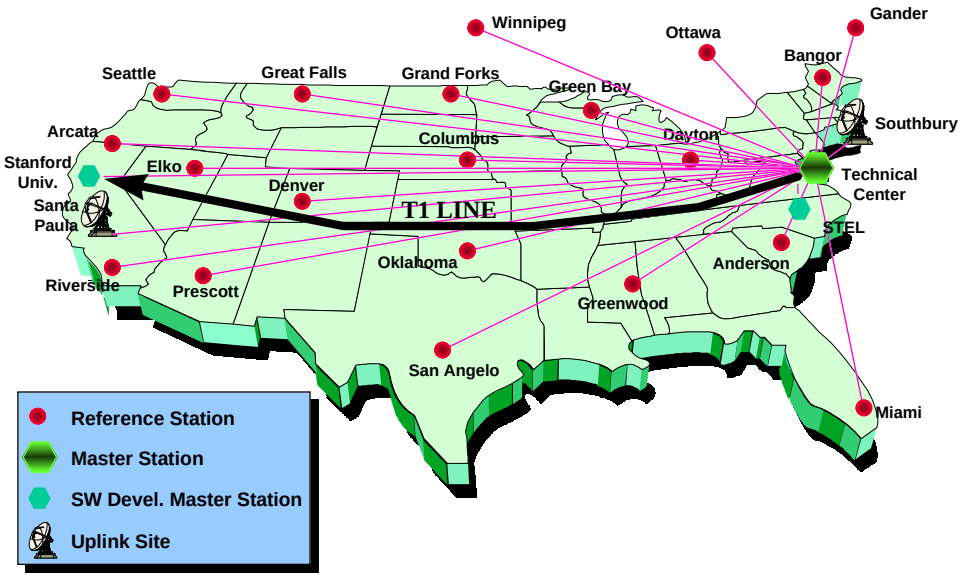

Figure 2.2: National Satellite Test Bed (NSTB)

reference stations are being established overseas through international cooperation. The WAAS generated messages will be sent to the two uplink stations which are located in Southburry, CT and Santa Paula, CA. Each testbed reference station (TRS) transmits the data, which includes raw GPS measurements, receiver flags and meteorological measurements, in real time to the FAA Technical Center (FAATC).

Through the NSTB, the FAA will ensure the success of the WAAS and a future seamless global navigation satellite system. Primary objectives of the NSTB are:

1. Provision of a test signal-in-space.

2. Data collection to support research and development.

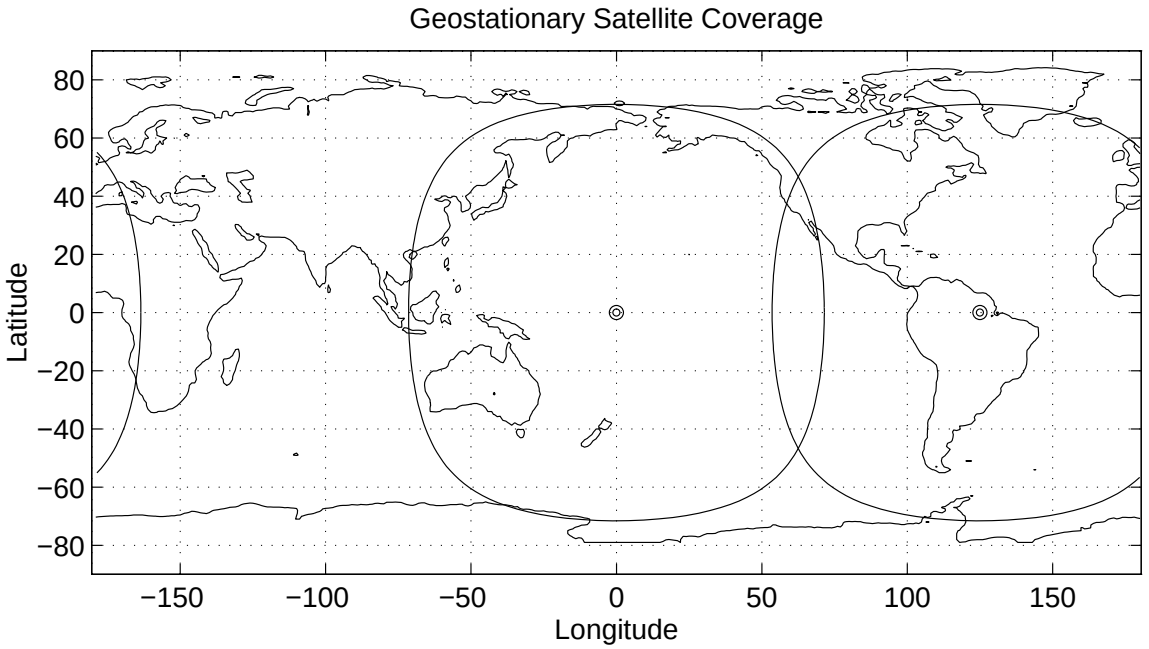

Figure 2.3: Coverage of the Inmarsat-3 Satellites

Coverage of the POR (180 degrees East) and AORW (55 degrees West) satellites is shown. Elevation mask angle of 10 degrees is used.

3. Validation of WAAS requirements and performance.

4. International cooperation and testing.

Measurements from the NSTB reference stations are transmitted to master stations at the FAA Technical Center, NJ. Three algorithm development and validation master stations receive these data over a T1 line. Currently, there are two uplink stations to upload the WAAS messages to Inmarsat III satellites.

Figure 2.3 shows the coverage of the Inmarsat-3 satellites that are located over the Pacific Ocean Region (POR, 180 degrees east) and the Atlantic Ocean Region (AOR-W, 55 degrees west) with an elevation mask of 10 degrees. Actual service coverage area depends on how the ground monitoring stations are distributed. Positioning

accuracy will be able to provide radionavigation guidance for all phases of flight. Category I accuracy is generally available within the network of the ground reference stations. Denser reference station deployment will provide better system redundancy and also reduce the system's sensitivity to data loss.

2.2 Wide-Area Reference Station

The Wide-Area Reference Stations (WRSs) use dual frequency (cross-correlating) receivers to obtain code and carrier phase measurements at both L_1 and L_2 frequencies. Multipath effects are reduced by using careful siting, narrow correlator technology, and a software-based mitigation algorithm [Dai]. Rubidium oscillators are located at each WRS to provide stable frequency standards. Raw GPS measurements, including pseudoranges and carrier phases, are sent thru a T1 line to the master stations. These measurements are described next.

2.2.1 GPS Observations

GPS observations from the TRSs can be expressed as follows:

$$\rho^j_{m,L_1} = D^j_m + I^j_m + T^j_m + b_m - B^j + v^j_{m,L_1} \quad (2.1)$$

$$\rho^j_{m,L_2} = D^j_m + \gamma\, I^j_m + T^j_m + b_m - B^j + v^j_{m,L_2} \quad (2.2)$$

$$\Phi^j_{m,L_1} = D^j_m - I^j_m + T^j_m + b_m - B^j + N_1\, \lambda_1 + e^j_{m,L_1} \quad (2.3)$$

$$\Phi^j_{m,L_2} = D^j_m - \gamma\, I^j_m + T^j_m + b_m - B^j + N_2\, \lambda_2 + e^j_{m,L_2} \quad (2.4)$$

where $\gamma = \frac{L_1^2}{L_2^2} = 1.647$, ρ^j_{m,L_1} is the L_1 pseudorange and Φ^j_{m,L_1} is the L_1 carrier phase for the j^{th} satellite at the m^{th} WRS. D^j_m is the geometric range from the station to

the satellite. I_m^j is the delay (code) or advance (carrier) caused by the ionosphere. T_m^j is the delay due to the troposphere. b_m is the receiver clock error and B^j is the satellite clock error. v_m^j is the pseudorange measurement noise and e_m^j is the carrier phase measurement noise. N_1 is the integer phase ambiguity for Φ_{m,L_1}^j and N_2 is the integer phase ambiguity for Φ_{m,L_2}^j. λ is the wavelength.

Ionospheric delays have opposite sign on the pseudorange and carrier phase. In addition, ionospheric delay is inversely proportional to signal frequency [Klobuchar], and so the delay caused by the ionosphere can be estimated using observations on L_1 and L_2. Besides GPS measurements, reference station data also contains temperature, pressure and relative humidity information, measured with a meteorological station. These measurements are used to model signal delay caused by the troposphere [Chao,c]. The modeling and estimation in the delays of the ionosphere and troposphere will be discussed later.

2.2.2 GPS Error Sources

GPS error sources are summarized as follows:

1. Satellite Clock Errors: Satellite clock errors can be calibrated using broadcast clock parameters. In spite of that, there are remaining errors which contain both real residual clock errors and intentional degradation implemented by the Department of Defense known as Selective Availability (SA). The clock errors are on the order of 22 meters (one sigma) in the range domain, mainly caused by SA [Parkinson] [van Graas].

2. Satellite Ephemeris Errors: GPS users rely on the broadcast ephemeris parameters to compute the geometric range from the receiver to the satellite. Because

these broadcast ephemeris parameters are not perfect, they will introduce errors in the geometric range computation. These errors are on the order of 3-4 meters in the range domain [DoDOrbit] [Zumberge].

3. Ionospheric Effect: As GPS signals travel through the ionosphere, the code phase is delayed and the carrier phase is advanced. The amount of delay is proportional to the total electron content (TEC) in the ionosphere. The electron density is a function of local time, magnetic latitude, and sunspot cycle. It reaches a peak at about 2:00 PM local time. The delay is inversely proportional to signal frequency and is elevation dependent and is typically on the order of several meters [Klobuchar]. The WRS can measure this delay with measurements on both frequencies.

4. Tropospheric Delay: This delay is caused when the signal travels through the atmosphere. These delays are a function of elevation angle. The errors are on the order of 2-25 meters [Spilker,b].

5. Multipath Effect: Multipath is the phenomenon wherby a signal arrives at a receiver via multiple paths which can be attributed to reflection and diffraction. It distorts the signal modulation and degrades accuracy in differential systems. Multipath affects both pseudoranges and carrier phases [Braasch].

6. Receiver Noise: This error comes from the thermal noise in the receiver front end. It can be modeled approximately as a normally distributed white noise. These errors are on the order of a few meters for code-phase measurements and a few millimeters for carrier-phase measurements.

Inter-frequency bias (IFB), caused by the timing difference between the frequency response of filtering the GPS L_1 and L_2 signals, is another error source which shows

up at the GPS observations of our reference station dual frequency GPS receivers. The inter-frequency biases, which exist in both the reference station receivers and the GPS satellites, need to be calibrated. IFB calibration is important for the ionospheric delay estimation and also affects the estimation of GPS ephemeris and clock errors. IFB calibration improves both the mean and the standard deviation of the navigation accuracy [Chao,b].

2.2.3 Reference Station Data Processing

The following paragraphs describe data processing conducted on the reference measurements (Figure 2.4), where these techniques are aimed at either removing or reducing the error sources described above.

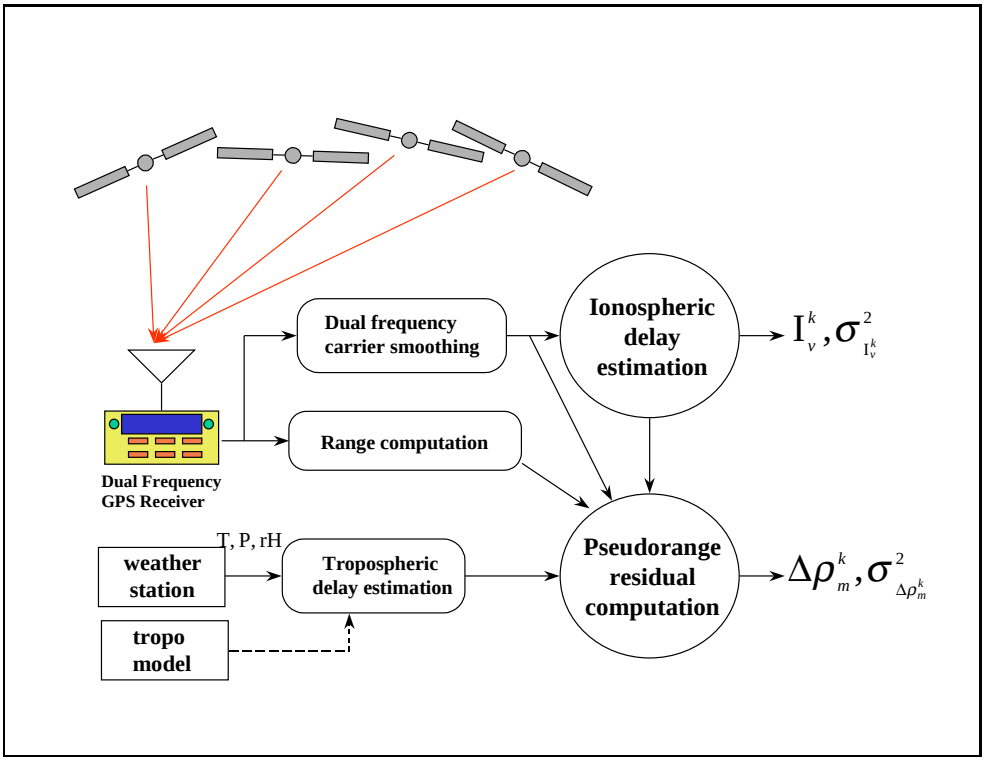

Figure 2.4: Reference Station Data Processing

Cycle Slip Detector A cycle slip occurs when the receiver loses lock in carrier tracking and has to re-acquire the lock. A cycle slip causes carrier-phase measurement to be discontinuous (the integer ambiguity N changes) and any carrier smoothing processes must be re-initialized. Raw measurements from each reference station have to be screened before they are used for later processing. Among the screens, cycle slip detection is the most important since a carrier smoothing technique (next topic) is employed and is fundamental in the WAAS processing.

Our previous approach for cycle slip detection used one past carrier-phase measurement and the current Doppler measurement to detect cycle slip. Figure 2.5 shows the synchronized pseudorange residuals of PRN 31 from our NSTB reference stations. The curves in Figure 2.5 should match each other very closely because the synchronized pseudorange residuals contain errors caused by the satellite clock errors and by the satellite ephemeris errors projected into the line of sight direction (synchronized pseudorange residual will be discussed in more details later). Given the distance separation of the NSTB reference stations, difference on the errors caused by the ephemeris errors in the range domain should be very small. However, the data from Greenwood (dashed line) is inconsistent with the data from the other reference stations. This discrepancy exists because Greenwood's Doppler measurements are noisier and more false alarms of cycle slip have occurred.

Each time the old algorithm detects a cycle slip, the carrier smoothing process has to be re-started. This is why Greenwood's curve (dashed line) diverges from the other curves at a few points in the figure. The diverged curve will eventually converge to the other curves once the smoothing process converges until another false alarm of cycle slip occurs. In a time span of about 40 minutes in Figure 2.5, there are 10 false cycle slip detections for Greenwood's data. The effect is that data from Greenwood

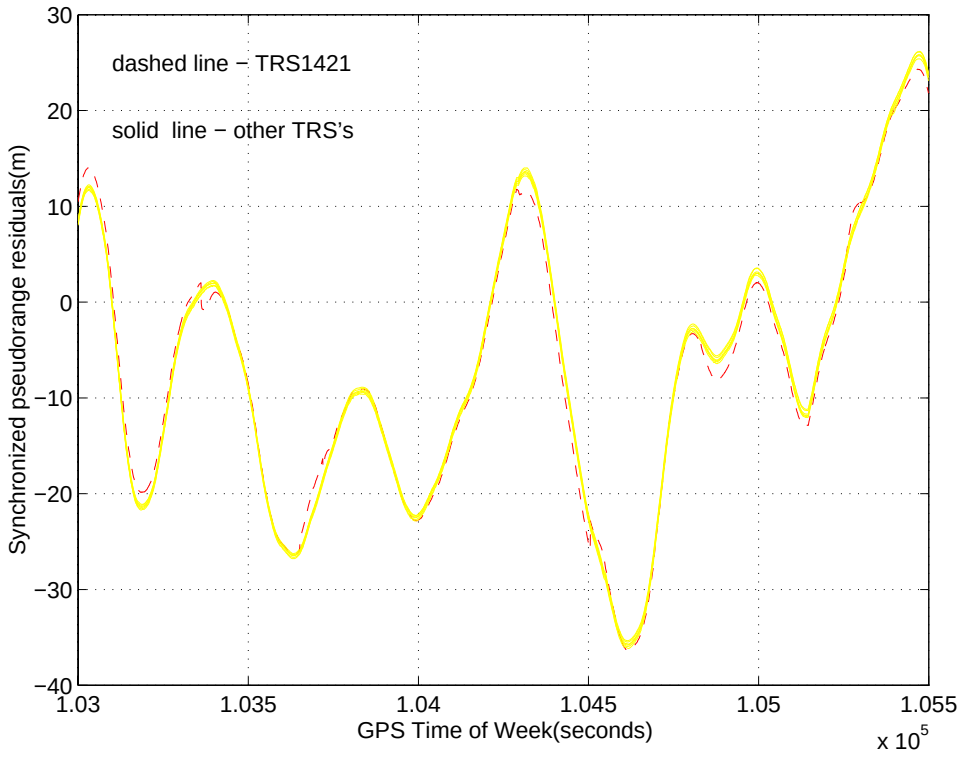

Figure 2.5: False Cycle Slip Detections Using Old Approach

Each false cycle slip detection causes the measurements from the Greenwood station (dashed line) to be inconsistent with the measurements from the other reference stations (solid lines). After implementing the LS quadratic cycle slip detector, this problem is solved.

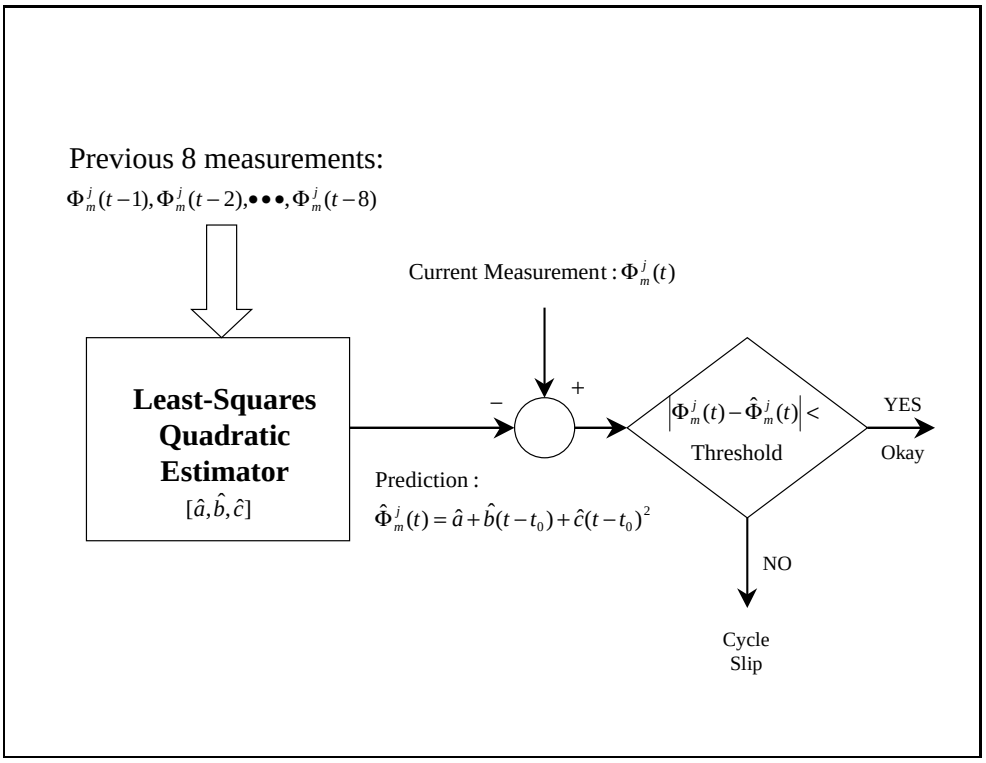

Figure 2.6: Least-squares Quadratic Cycle Slip Detection

will be weighted less or even excluded in later data processing.

To solve this problem, I implemented a least-squares quadratic phase predictor for cycle slip detection. This approach uses the previous eight carrier-phase measurements to fit a quadratic curve

$$\Phi(t_k) \;=\; a \;+\; b\,(t_k - t_0) \;+\; c\,(t_k - t_0)^2 \tag{2.5}$$

These quadratic coefficients $[a, b, c]$ are estimated using a least-squares estimator. Predicted carrier-phase is computed as follows

$$\hat{\Phi}(t) \;=\; \hat{a} \;+\; \hat{b}\,(t - t_0) \;+\; \hat{c}\,(t - t_0)^2 \tag{2.6}$$

A cycle slip is detected if the difference between the current measurement $\Phi(t)$ and the predicted value $\hat{\Phi}(t)$ exceeds a predefined threshold. The threshold is chosen to be one wavelength. A block diagram for this LS quadratic cycle slip detector is shown in Figure 2.6.

After we implemented the LS quadratic cycle slip detector and reprocessed the data, false cycle slip detection did not occur again (as compared to 10 false detections in Figure 2.5). Consequently, the data from Greenwood becomes usable.

This approach is straightforward and easy to implement. Furthermore, it is also robust to data dropout and can maintain prediction accuracy for several seconds. In addition, it is independent of reference sites and receiver types.

Dual Frequency Carrier Smoothing Since the carrier phase contains much smaller measurement errors than the pseudoranges while containing nearly the same information, the carrier phase can be used to smooth the pseudorange to reduce its noise level. When the signal travels through the ionosphere, the code phase is delayed and the carrier phase is advanced. This phenomenon is called code-carrier divergence. By combining measurements on both frequencies, the code-carrier divergence problem can be avoided. Cycle slips have to be reliably detected so that patching or re-initializing of the smoothed estimate can be executed. A detailed description of the Stanford dual frequency carrier smoothing algorithm can be found in [Chao,d].

The smoothed L_1 pseudorange is denoted as $\hat{\rho}^j_{m,L_1}$. $\hat{\rho}^j_{m,L_1}$ is similar to ρ^j_{m,L_1} of Equation (2.1) but with smaller noise level.

Ionospheric Delay Estimation The measurements from dual frequency receivers are used to separate the ionospheric delay from other error sources. This is done by

combining dual frequency pseudoranges and carrier phases as follows:

$$I^j_{m,\rho} = \frac{\rho^j_{m,L_2} - \rho^j_{m,L_1}}{\gamma - 1} \tag{2.7}$$

$$I^j_{m,\Phi} = \frac{\Phi^j_{m,L_1} - \Phi^j_{m,L_2}}{\gamma - 1} \tag{2.8}$$

$I^j_{m,\rho}$ is noisy and $I^j_{m,\Phi}$ is very precise though biased by the integer ambiguity terms. A better estimate of $I^j_{m,\rho}$ is obtained by smoothing (using $I^j_{m,\Phi}$). More details can be found in [Chao,d].

The smoothed ionospheric delay estimate is denoted as $\hat{I}^j_m$.

Tropospheric Delay Estimation The WRS uses a meteorological station to calibrate the pseudorange error caused by the troposphere. Temperature, pressure and relative humidity provide the inputs for estimating the vertical tropospheric delay. This is then converted to the range domain by multiplying a mapping function to derive the tropospheric delay estimate. The mapping function is approximately $1/\sin(El)$, where El is the elevation angle. As shown in Figure 2.4, a standard tropospheric model (bottom left with dashed line) can be used alternatively to estimate the delay.

The tropospheric delay estimate is denoted as $\hat{T}^j_m$.

Geometric Range and Satellite Clock Bias Computation Broadcast satellite ephemeris and clock parameters [SPS] are used to compute satellite position, $\hat{\mathbf{R}}^j$, and satellite clock bias, $\hat{B}^j$, at the time of signal transmission. The range from the WRS to the satellite, $\hat{D}^j_m$, is computed based on the computed satellite position, $\hat{\mathbf{R}}^j$, and

the precisely surveyed location of the WRS antenna, $\mathbf{R}_m$.

$$\hat{D}_m^j = \left|\mathbf{R}^j - \mathbf{R}_m\right| \tag{2.9}$$

Pseudorange Residual Computation Pseudorange residual is computed by removing geometric range, satellite clock bias, ionospheric delay, and tropospheric delay from the carrier smoothed pseudorange as follows:

$$\Delta\rho_m^j = \hat{\rho}_m^j - \hat{D}_m^j - \hat{I}_m^j - \hat{T}_m^j + \hat{B}^j$$

Because $\mathbf{R}^j = \hat{\mathbf{R}}^j + \Delta\mathbf{R}^j$ where $\Delta\mathbf{R}^j$ is the ephemeris error, we can simplify the above equation to be

$$\Delta\rho_m^j = \Delta\mathbf{R}^j \cdot \mathbf{1}_m^j + b_m - \Delta B^j + v_m^j \tag{2.10}$$

where ΔB^j is the clock error for the j^{th} satellite, b_m is the clock error of the m^{th} WRS and v_m^j is the measurement noise which accounts for the error in carrier smoothing, ionospheric delay estimation and tropospheric delay estimation. $\mathbf{1}_m^j$ is the unit line of sight vector from the reference station to the satellite.

The sigma values for $\Delta\rho_m^j$ are computed as follows

$$\sigma^2_{\rho_m^j} = \sigma^2_{\hat{\rho}_m^j} + \sigma^2_{\hat{I}_m^j} + \sigma^2_{\hat{T}_m^j} \tag{2.11}$$

The measurement in Equation (2.10) contains the nuisance parameter, b_m, which causes measurement coupling between the satellites and is of no interest to the WAAS users. This nuisance parameter will be eliminated in later processing. The confidence values of these pseudorange residuals will be used to form the covariance matrix for

the measurement noise.

In summary, the pseudorange residuals are derived as follows:

- Carrier smoothing is accomplished using measurements on both frequencies.
- Ionospheric delay is measured and removed.
- Tropospheric delay is modeled and removed.
- Geometric range and satellite clock bias are computed and removed.

2.3 Wide-Area Master Station

The Wide-Area Master Station (WMS) receives and processes the data from all of the WRSs and generates vector corrections and integrity information for: vertical ionospheric delays for a grid of predefined locations, satellite ephemeris errors and satellite clock errors. Ionospheric delay modeling and estimation can be found in [Chao,a] [Hansen,a] [Mitre] and is not the subject of this dissertation.

This section describes the WMS data processing algorithms which generate the measurements to be used later for ephemeris and clock error estimation. Figure 2.7 details the overall data processing flow of our master station algorithms. The algorithms developed for the master station data processing include: a master clock filter to generate a common reference for all reference stations, a common view time transfer (CVTT) filter to synchronize the measurements and decouple them from satellite to satellite, an ephemeris error estimator, a satellite clock error estimator and a UDRE estimator. My WMS algorithms for ephemeris and clock error estimation are detailed in Chapters 3 and 4.

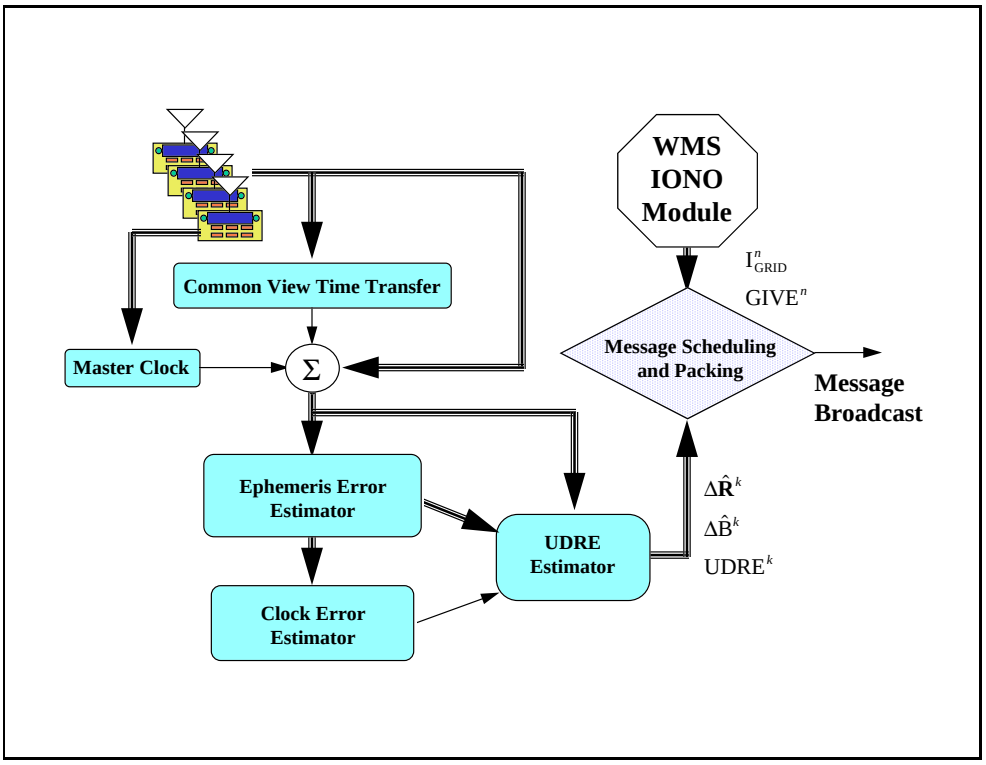

Figure 2.7: Master Station Data Processing

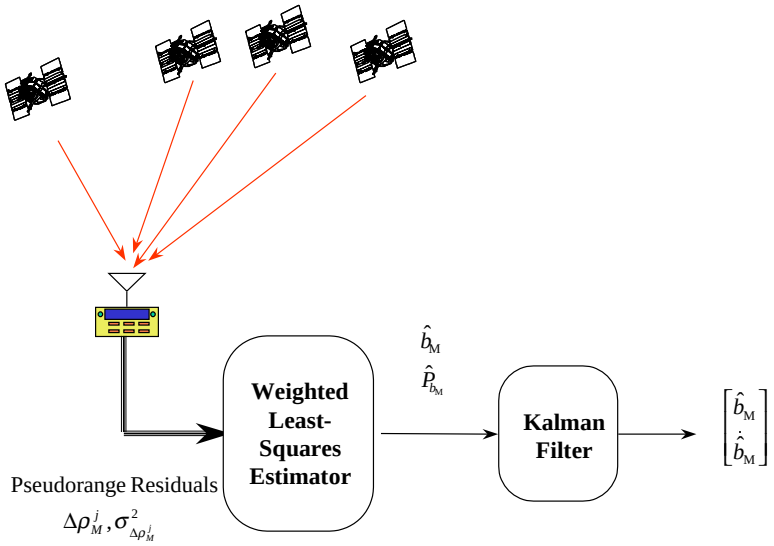

Figure 2.8: Master Clock Filter

The input measurements used are the smoothed pseudorange residuals from all the reference stations. These measurements are coupled between satellites because of receiver's clock terms, which are of no interest to the users. These nuisance parameters can be removed using estimates from a master clock filter and common view time transfer.

2.3.1 Master Clock Filter

A stable frequency reference is required to provide a slowly varying time base at the reference station. The purpose of this clock filter is to provide a common reference for pseudorange residuals. This can be an ensemble clock (composite clock) or simply one of the reference station clocks. We choose the latter because it is simpler to

implement the clock filter and less complicated to detect and isolate possible outlying measurements. An ensemble clock would provide better smoothing of the clock noise but will be more complex in the filter implementation and outlier isolation.

The measurements are smoothed pseudorange residuals, $\Delta\rho_M^j$, for all satellites observed by the master station, together with their variances, $\sigma^2_{\Delta\rho_M^j}$. First, a weighted least-squares (WLS) estimator is used. Its estimate and variance are

$$\hat{b}_M = \left(\sum_{j=1}^{j=N} \frac{\Delta\rho_M^j}{\sigma^2_{\Delta\rho_M^j} + (\mathrm{U}RA^j)^2} \right) / \hat{\mathbf{P}}_{\hat{b}_M} \tag{2.12}$$

$$\hat{P}_{\hat{b}_M} = \left(\sum_{j=1}^{j=N} \frac{1}{\sigma^2_{\Delta\rho_M^j} + (\mathrm{U}RA^j)^2} \right)^{-1} \tag{2.13}$$

where N is number of satellites observed by the master station. Satellites with smaller broadcast user range accuracy (URA) are weighted more heavily.

Any discontinuities in this WLS clock estimates, which might be due to rising or setting of the satellites, have to be avoided. Therefore, a sequential filter is required to provide smoothing. Figure 2.8 shows the processing flow of our master clock filter.

This WLS estimate of the master clock offset, $\hat{b}_M$, is used as an input for a Kalman filter. This Kalman filter generates smoothed and continuous estimates even when there is temporary data loss. The Kalman filter has a time constant of about 120 seconds.

Note that this estimate is not accurate since pseudorange residuals are corrupted by SA. However, the error in $\hat{b}_M$ is common to all satellites and therefore this error will be absorbed in the user's receiver clock error estimate. Nevertheless, this estimate can not be larger than the range allowed by the WAAS message format (Section 2.4).

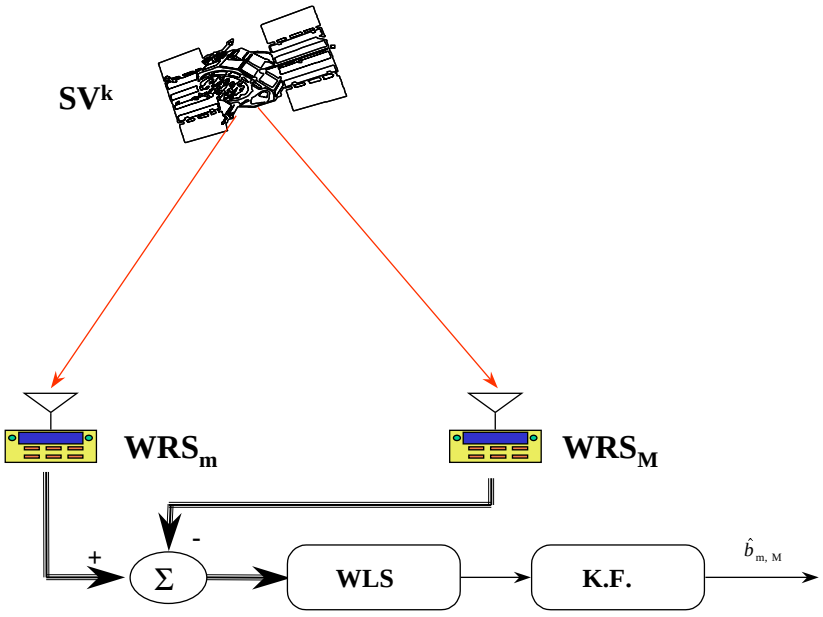

Figure 2.9: Common View Time Transfer

2.3.2 Common View Time Transfer

Common View Time Transfer (CVTT) is used to remove the nuisance parameter, b_m, in Equation (2.10) when combined with the master clock estimate, $\hat{b}_M$. We wish to find the difference between the clock bias of the m^{th} reference receiver and the clock bias of the master station. CVTT first differences the pseudorange residuals from two sites as follows:

$$\begin{aligned} \Delta^j_{m,M} &= \Delta\rho^j_m - \Delta\rho^j_M \\ &= \Delta\mathbf{R}^j \cdot (\mathbf{1}^j_m - \mathbf{1}^j_M) + \Delta b_{m,M} + v^j_{m,M} \end{aligned} \tag{2.14}$$

The line of sight difference, $(\mathbf{1}_m^j - \mathbf{1}_M^j)$, is small because of the size of the NSTB network. The ephemeris error, $\Delta\mathbf{R}^j$, is also small because of the quality of the GPS broadcast ephemeris. For these two reasons, the first term in Equation (2.14) is very small. A good estimate of the clock difference can be achieved as follows:

$$\Delta\hat{b}_{m,M} = \frac{1}{K_{m,M}} \sum_{j=1}^{K_{m,M}} \Delta_{m,M}^j \tag{2.15}$$

where $K_{m,M}$ is the number of satellites in the common view of both WRSs.

This estimator averages the clock differences as computed from all of the satellites jointly observed by both WRSs. Using multiple common satellites reduces the error introduced by the measurement noise and the ephemeris errors. In addition, our estimate is averaged over time to take advantage of the well behaved characteristics of the Rubidium clocks at our WRSs. A Kalman filter, with a time constant of about 300 seconds, is implemented. Figure 2.9 shows the implementation of the common view time transfer technique.

The estimate of single differenced receiver clock bias is then used to eliminate the b_m term in Equation (2.10). Thus we have all of the measurements in terms of one common clock. The synchronized pseudorange residuals are

$$\begin{aligned} \Delta\tilde{\rho}_m^j &= \Delta\rho_m^j - \hat{b}_{m,M} - \hat{b}_M \\ &= \Delta\mathbf{R}^j \cdot \mathbf{1}_m^j - \Delta B^j + v_m^j \end{aligned} \tag{2.16}$$

The sigma values for $\Delta\tilde{\rho}_m^j$ are computed as follows

$$\sigma^2_{\tilde{\rho}_m^j} = \sigma^2_{\tilde{\rho}_m^j} + \sigma^2_{\hat{b}_{m,M}} + \sigma^2_{\hat{b}_M} \tag{2.17}$$

These synchronized pseudorange residuals are the fundamental inputs to the satellite ephemeris and clock error estimation algorithms.

The common view synchronization is important because the measurements are now decoupled from one satellite to another. As a consequence, it is now possible for the WMS to contain one small estimator for each of the satellites in view of the network. In contrast, if the residuals were not synchronized, then all of the observations are coupled together and a single large estimator must be used to solve for tens of unknowns [Kee,b]. It is easier to implement and perform error analysis on sequential algorithms when small and decoupled estimators are used.

2.3.3 Reference Station Clock Failures

This section gives a qualitative introduction of reference station clock failures. Satellite clock failures are discussed in Chapter 4. The end to end assessment of the impact of the reference station clock failures is described in Chapter 5.

Receiver clock failures have direct effects on the GPS measurements. Failure of the master clock impacts all of the pseudorange residuals since its estimate is used for synchronization. A TRS clock failure makes its measurement data unusable. These failures need to be investigated and an algorithm needs to isolate bad measurements caused by clock failures.

Our TRS and master clock studies were conducted by adding simulated errors to the real GPS measurements. The studies here are not intended to cover all possible clock failures but to investigate two most common types of clock failures:

- A ramp type clock failure that introduces the following error:

$$e_m(t) = \begin{cases} 0 & t < t_0 \\ \alpha\,(t - t_0) & t \geq t_0 \end{cases}$$

- A step type clock failure that introduces the following error:

$$e_m(t) = \begin{cases} 0 & t < t_0 \\ A & t \geq t_0 \end{cases}$$

where t_0 is the beginning time when the failure is introduced. $e_m(t)$ is added to the raw pseudoranges and carrier phases while α is added to the Doppler (ramp type failure only) from the m^{th} reference station. We will describe the TRS clock failures followed by the master clock failures.

TRS Clock Failures A reference station clock failure can be detected and identified when its measurements are combined for processing with the measurements from all other stations (in the CVTT filter and in later ephemeris and satellite clock filters). The following criteria are used to isolate one station's measurements:

- The CVTT estimate fails the chi-square test (Appendix A) for more than 120 seconds. This number is chosen such that the generated corrections will not be corrupted by the reference station clock failure and the 6 second time to alarm integrity requirement can be met [MOPS]. A counter is maintained to count the number of continuous alarms in the chi-square test of the CVTT filter. The counter is updated every second. If this counter exceeds 120 we will exclude this troubled TRS. The Studentized t test (Appendix B) would not help in isolation since all measurements from this TRS are corrupted by the clock failure.

- Estimated clock error rate is greater than 1.5 meters per second. For the Rubidium clocks used for our TRSs, this number should never be exceeded.

The measurements from the reference station will not be used if either of the above conditions happens.

Being able to isolate the measurements from a troubled reference station in the early stage of measurement processing reduces computational complexity. Since the bad measurements are already excluded from correction generation, further computation for outlier isolation in the ephemeris and clock estimation modules can be avoided.

I have investigated ramp-type and step-type reference station clock failures. Figure 2.10 shows the synchronized pseudorange residuals for PRN 26 from all the stations observing this satellite. At one point, a ramp type error of magnitude 0.5 m/s is introduced to the measurement data from the Miami station. Clearly, Miami's measurements deviate from other station's measurements. Other satellites observed by Miami show similar results. Before this clock failure is isolated, accuracy bounds for the satellites observed by Miami are increased because of the failed chi-square test. Eventually, measurements from Miami will be excluded from further processing.

Step-type failures are identified because once the error is first introduced to the measurements they cause a sudden jump in the pseudorange residuals for the TRS. This jump causes an alarm in the chi-square test and the estimate of the clock error rate increases abruptly. Our algorithm catches this phenomenon and declares the TRS unusable.

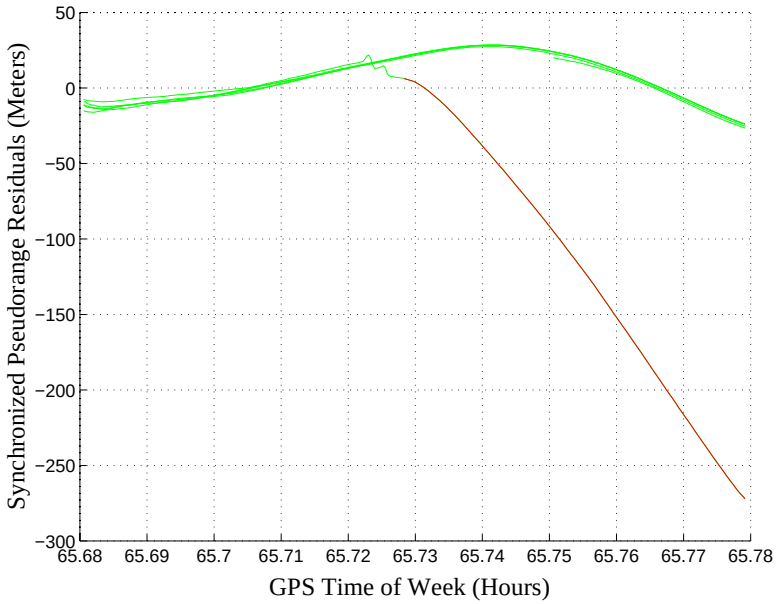

Figure 2.10: Ramp Type Reference Station Clock Failure

Synchronized pseudorange residuals for PRN 26 from all the TRSs are plotted. The Miami data includes a simulated ramp error that its curve diverges from the others. Miami's data are excluded from correction generation after its CVTT estimates fail the chi-square test continuously for 120 seconds.

Master Clock Failures Failures on the master clock will affect all station's measurements. This type of failure, if not identified, will invalidate ephemeris and clock corrections. Therefore, more stringent constraints are necessary in order to isolate the failure as early as possible. The constraints we implemented are:

- The master clock estimate fails the chi-square test for more than 60 seconds.
- Estimated clock error rate is greater than 1.5 meters per second.

Once either of the above conditions happens, the location of the master clock needs to be switched. This master clock switching was also implemented on our TMS. We have also tested our algorithm using both simulated ramp-type and step-type failures. In either case, the failure is identified using the above criteria and the master clock is changed.

Here only a qualitative introduction of the reference station clock failures is given. The end to end quantitative study of the impact of the TRS clock failures on RNP performance is presented in Chapter 5.

2.4 RTCA Defined WAAS Messages

Special Committee 159 Working Group 2 of the Radio Technical Commission for Aeronautics (RTCA) has designed the WAAS signal specifications [WG2]. The RTCA has also delivered the Minimum Operational Performance Standards (MOPS) for WAAS avionics [MOPS].

For each GPS satellite, the WAAS message contains separate corrections for the quickly varying component of the pseudorange error (mostly satellite clock) and the slowly varying component of the pseudorange error (mostly satellite ephemeris). The

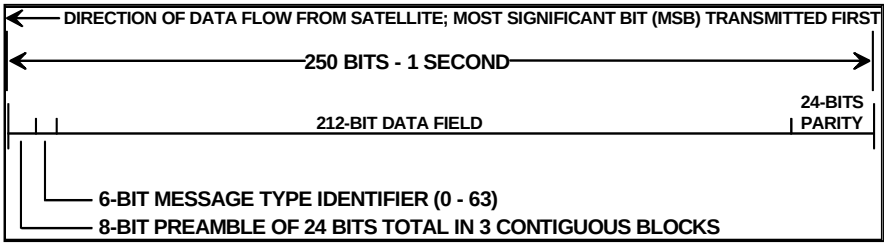

Figure 2.11: WAAS Data Block Format

WAAS message also carries estimates of the vertical ionospheric delay for a grid of locations.

The basic WAAS message is 250 bits in length. The data block format is shown in Figure 2.11. At the data rate of 250 bits per second, the duration of a WAAS message is one second, and the start of the message block is synchronous with a six second GPS time epoch. Each block consists of: an 8 bit (distributed) preamble, a 6 bit message type, a 212 bit data field, and a 24 bit cyclic redundancy check (CRC) parity [WG2].

The preamble is a 24-bit unique word, distributed over 3 successive blocks. An 8-bit preamble is adequate because the WAAS message is one second in duration and remains synchronized with the GPS time epoch of six seconds. The message type field is 6 bits long, which allows for 64 different messages. The currently defined message types are summarized in Table 2.1.

This WAAS message format serves an extremely ambitious goal: provide Category

Type	Contents	Max. Update Interval	Used
0	Don't use GEO for anything (for testing)		yes
1	PRN mask assignments	120 s	yes
2-5	Fast corrections	6 s	yes
6	Integrity information	6 s	yes
7	UDRE degradation factor	120 s	yes
8	Reserved for future messages		no
9	GEO navigation message	120 s	yes
10	Degradation parameters	120 s	yes
11	Reserved for future messages		no
12	WAAS Network Time/UTC offset parameters	300 s	no
13-16	Reserved for future messages		no
17	GEO satellite almanacs	300 s	yes
18	Ionospheric grid point masks	300 s	yes
19-23	Reserved for future messages		no
24	Mixed fast/long-term satellite error corrections	120 s	yes
25	Long-term satellite error corrections	120 s	yes
26	Ionospheric delay corrections	300 s	yes
27	WAAS Service Message	300 s	no
28-61	Reserved for future messages		no
62	Internal test Message		no
63	Null message		yes

Table 2.1: WAAS Message Types

The fast corrections (types 2-5) are sent every 6 seconds, the slow (long term) corrections (types 24-25) are sent every 120 seconds, and the ionospheric corrections are sent every 300 seconds.

I precision approach accuracy over a continental area using only a data rate of 250 bits per second. Indeed, greater bit rates would require the received signal power from the geostationary WAAS satellites to be greater than the received power from the GPS satellites - an undesirable outcome. Yet the WAAS message stream must carry corrections for all observed GPS satellites in orbit. In contrast, local area DGPS data links typically use several kilobits per second or more to provide a similar capability to ranges of two or three hundred kilometers. Moreover, local links need only carry corrections for the 6 to 12 satellites which are in view of a single reference station. The details of the WAAS message format are given in [Enge,a], [Enge,b], [WG2], and in [MOPS].

The WAAS message format basically achieves highly efficient use of very limited capacity as follows.

Masks A *mask* is used to designate which satellite belongs to which slot in the fast correction messages. A mask is used to assign slots so that satellite identifications need not be sent with every fast correction. A similar ionospheric mask is used to associate each slot in the ionospheric correction message with a geographic location. These mask messages have to be received before any differential corrections can be applied.

Fast and Slow Corrections Fast correction messages carry the quickly varying component of the pseudorange errors for each satellite (mostly clock error). They will also carry the *use/don't use* integrity data for each GPS satellite. As such, they must be sent much more frequently than any other message (every 6 seconds). They do not decorrelate spatially. Consequently, a single fast correction per satellite suffices for the entire footprint of the WAAS satellite. The GPS error components which

vary more slowly are separated from the fast components and can be sent much less frequently.

The WAAS signal specification constrains the ranges of the fast and slow corrections as follows [MOPS]:

- $-256.0 <$ Fast Correction < 255.875 (meters).
- Ephemeris Error $< \pm 127.875$ (meters).
- Ephemeris Error Rate $< \pm 0.0625$ (meters/sec).

No Rate Corrections Unlike most local area DGPS data formats, the WAAS carries no rate corrections for the quickly varying component of the satellite error. As shown in [Hegarty], it is more efficient for the user receiver to estimate the rate by differencing the most recent fast corrections.

Geostationary Navigation Message In contrast to the GPS satellites, the WAAS satellites are geostationary; so their location (X, Y, Z) need only be updated every 2 minutes or so.

Parity The WAAS uses a much stronger parity algorithm than the extended Hamming code used in the GPS navigation message (and typically used for the transmission of differential corrections). To reduce the probability of failing to detect a bit error, the parity scheme uses 24 bits and thus reduces the probability of failing to detect an interference burst to $2^{-24} = 5.96 \times 10^{-8}$. In contrast, GPS adds 6 parity bits to every 24 data bits for an overhead of $6/30 = 0.20$. The WAAS overhead is $24/250 \approx 0.096$.

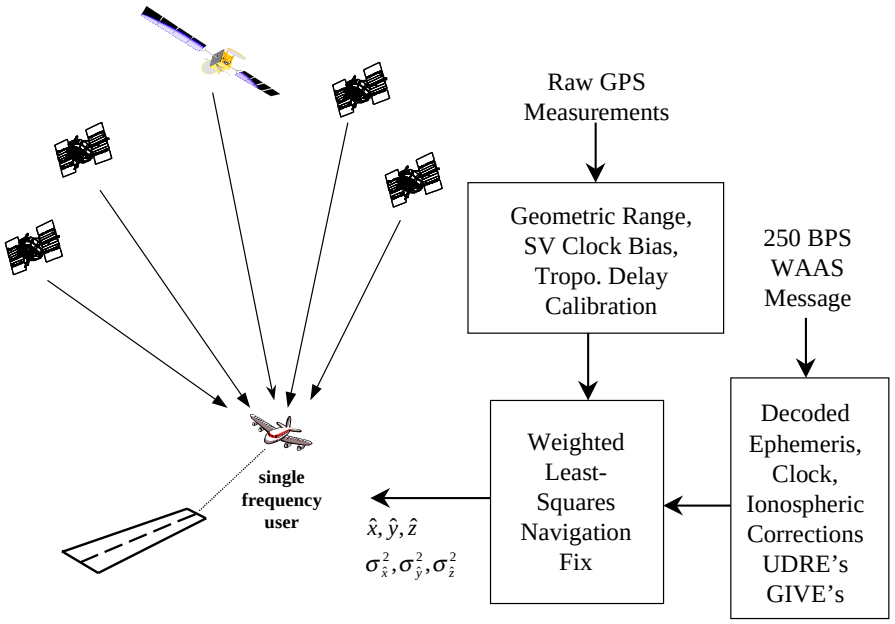

Figure 2.12: Data Processing for WAAS Avionics

2.5 WAAS Avionics

The WAAS is to serve airborne users that are equipped with single frequency GPS/WAAS receivers. The WAAS receivers will only need minimal modifications from current GPS receivers. They must be certified by the FAA and conform to the appropriate WAAS Technical Standard Order (TSO). This TSO will be based on the WAAS Minimum Operational Performance Standard already developed by the RTCA [MOPS].

A typical WAAS user is shown in Figure 2.12. Basically, a WAAS receiver is required to perform the following functions:

1. Receive GPS signals and make the uncorrected measurements of pseudorange, carrier phase, and Doppler.

2. Receive the WAAS signals and unpack the WAAS messages (Table 2.1).

3. Compute the geometric range and satellite clock bias using broadcast ephemeris/clock parameters.

4. Compute the tropospheric delay using a standard model described in [MOPS]. Because the tropospheric delay is a local phenomenon, the WAAS does not provide the tropospheric corrections. Instead, airborne receivers use a standard atmospheric model to calibrate this delay which should remove all but a very small part of the delay.

5. Apply the decoded WAAS corrections and integrity information. These corrections are applied to account for broadcast ephemeris errors, clock errors and ionospheric delays.

6. Compute the weighted least-squares (WLS) position fix as follows:

$$\hat{\mathbf{x}}_{user} = (\mathbf{H}^T\mathbf{W}^{-1}\mathbf{H})^{-1}\mathbf{H}^T\mathbf{W}^{-1}\mathbf{z} \tag{2.18}$$

where $\hat{\mathbf{x}}_{user}$ contains the linearized user position and clock. $\mathbf{W}$ is the weighting matrix whose elements are computed using the UDRE's, GIVE's provided by WAAS, and the receiver's estimate of error in the pseudorange measurement introduced by local noise, interference, and multipath. $\mathbf{z}$ is the linearized measurement vector and $\mathbf{H}$ is the design matrix whose row is composed of the unit line of sight vector from the receiver to the satellite and the clock element. Iteration is required until the solution converges. The receiver must also compute

the covariance matrix

$$\hat{\mathbf{P}}_{user} = (\mathbf{H}^T\mathbf{W}^{-1}\mathbf{H})^{-1} \tag{2.19}$$

Since no truth is available for the airborne receiver, this estimated sigma will be used to decide if the approach should be continued or a missed approach should be executed.

The WAAS fixed position estimate (Equation (2.18)) will be used for flight guidance. However, the covariance information (Equation (2.19)) is even more important since it determines whether or not an approach should or should not be continued. If the estimated sigma value $(\sigma_{\hat{x}}, \sigma_{\hat{y}}, \sigma_{\hat{z}})$ exceeds the alarm limits, horizontal protection limit (HPL) or vertical protection limit (VPL),

$$\begin{cases} 5.33\sqrt{\sigma_{\hat{x}}^2 + \sigma_{\hat{y}}^2} > \text{HPL} \\ 5.33\ \sigma_{\hat{z}} > \text{VPL} \end{cases}$$

a missed approach has to be executed [MOPS].

Chapter 3

Satellite Ephemeris Estimation Algorithms

Chapter 2 described the measurement pre-processing for the reference station data to generate the required inputs for ephemeris and clock error estimation. This chapter will detail how we compute the estimates and covariance matrix of the ephemeris errors for all satellites observed by the WAAS network. Chapter 4 will detail how we compute the estimates and covariance matrix of the satellite clock errors.

This chapter discusses the approaches we developed to generate estimates and the covariance matrix of ephemeris errors. A snapshot algorithm is developed first to solve for the ephemeris errors using a geometric approach. Although this estimate is capable of providing the necessary positioning accuracy, it is noisy and sensitive to observation geometry and data loss. Filtering is necessary to prevent large discontinuities and also to provide prediction when no measurements are available (e.g., network outages for a few seconds).

Outlier detection and isolation are also implemented to monitor satellite health in

real time. Our algorithms are also tested using data containing maneuvering satellites.

3.1 Ephemeris Error Measurements

As described in the previous chapter, the basic inputs for satellite ephemeris and clock error estimation are derived from the CVTT module. The pseudorange residuals from all reference stations are synchronized to a common clock, i.e., the master clock. This clock synchronization removes the coupling of pseudorange residuals so that the new measurements are independent from satellite to satellite. Each satellite will maintain its own filter which is much smaller than combining all satellites in a huge filter. In our case, a 6 x 6 matrix inversion is required for each satellite (3 states for (X, Y, Z) ephemeris error and 3 states for $(\dot{X}, \dot{Y}, \dot{Z})$ ephemeris error rate) as compared to a 6N x 6N matrix inversion if the measurements are coupled. N is the number of satellites observed by our network. Furthermore, outlier detection and isolation are simpler because of the measurement independence when we need to remove outlying measurements and re-do all the matrix computation.

The synchronized pseudorange residual measurement for the k^{th} satellite observed by the m^{th} reference station is re-written below:

$$\Delta\tilde{\rho}_m^k = \Delta\mathbf{R}^k \cdot \mathbf{1}_m^k - \Delta B^k + v_m^k$$

where $\Delta\mathbf{R}^k$ is the ephemeris error vector and $\mathbf{1}_m^k$ is the unit line of sight vector from the m^{th} reference station to the k^{th} satellite. ΔB^k is the satellite clock error which includes Selective Availability and real satellite clock error. It also contains the residual error of the master clock which is common to all satellites. v_m^k is the measurement noise, and includes multipath, natural noise and interference.

To separate the fast varying clock error from ephemeris error, single differencing is necessary [Chao,d]. Although directly solving for $\Delta\mathbf{R}^k$ and ΔB^k simultaneously is possible and the estimates can provide adequate accuracy for the users, doing so will not allow us to broadcast the fast/slow messages defined by the WAAS [WG2]. With such a direct solution, both ephemeris and clock errors have to be sent frequently and this will occupy too much of the WAAS broadcast bandwidth.

We use a single difference to remove the satellite clock error term (ΔB^k) as follows:

$$\Delta\tilde{\rho}_m^k - \Delta\tilde{\rho}_p^k = (\mathbf{1}_m^k - \mathbf{1}_p^k)\cdot\Delta\mathbf{R}^k + \epsilon_m^k$$

where subscript "p" denotes the pivotal reference station which has the smallest variance.

In matrix form, the above equation can be rewritten as

$$\mathbf{z} = \mathbf{H}\cdot\Delta\mathbf{R}^k + \mathbf{v} \tag{3.1}$$

where

$$\mathbf{z} = \begin{bmatrix} \Delta\tilde{\rho}_1^k - \Delta\tilde{\rho}_p^k \\ \vdots \\ \Delta\tilde{\rho}_M^k - \Delta\tilde{\rho}_p^k \end{bmatrix}$$

$$\mathbf{H} = \begin{bmatrix} \mathbf{1}_1^k - \mathbf{1}_p^k \\ \vdots \\ \mathbf{1}_M^j - \mathbf{1}_p^k \end{bmatrix}$$

$$\begin{aligned} E[(\epsilon_m^k)^2] &= E[(v_m^k)^2] + E[(v_p^k)^2] \\ &= (\sigma_m^k)^2 + (\sigma_p^k)^2 \end{aligned}$$

M is the number of synchronized pseudorange residual measurements. Measurement noise $\mathbf{v}$ is treated as zero mean with covariance $\mathbf{W}$. The number of measurements is $M-1$ because of the single difference.

Figure 3.1 shows a 24-hour plot of the ephemeris errors $\Delta\mathbf{R}^k$ (in meters) in the radial, along-track and cross-track directions for GPS space vehicle PRN 4. These errors are computed from the difference between IGS precise and broadcast ephemeris [IGS]. As shown, the ephemeris errors behave sinusoidally with a period of about 12 hours. Apparently there is no SA implemented on satellite ephemerides [Zumberge]. Each discontinuity in this figure comes from a new ephemeris broadcast but not every new ephemeris broadcast will cause this kind of discontinuity. New ephemeris parameters normally are broadcast every two hours. It is clear from this figure that the ephemeris errors vary slowly in all three components.

3.2 Snapshot Algorithms

To solve for satellite ephemeris error described by Equation (3.1), several mathematical approaches are available. The snapshot solution basically uses GPS upside down by solving for GPS satellite locations using ground based receivers. The geometric conditions are always good (Position dilution of precision, PDOP, is below 2.5 95% of the time [AIAAGPS]) for the GPS positioning case. The PDOP for the linear system described in Equation (3.1) is significantly worse (several hundreds or greater) because the satellite is very distant from the Earth and the observing network is small in size.

Several researchers have proven that snapshot estimates can provide the required accuracy for the WADGPS users [Kee,a] [Enge,a]. However, generated corrections

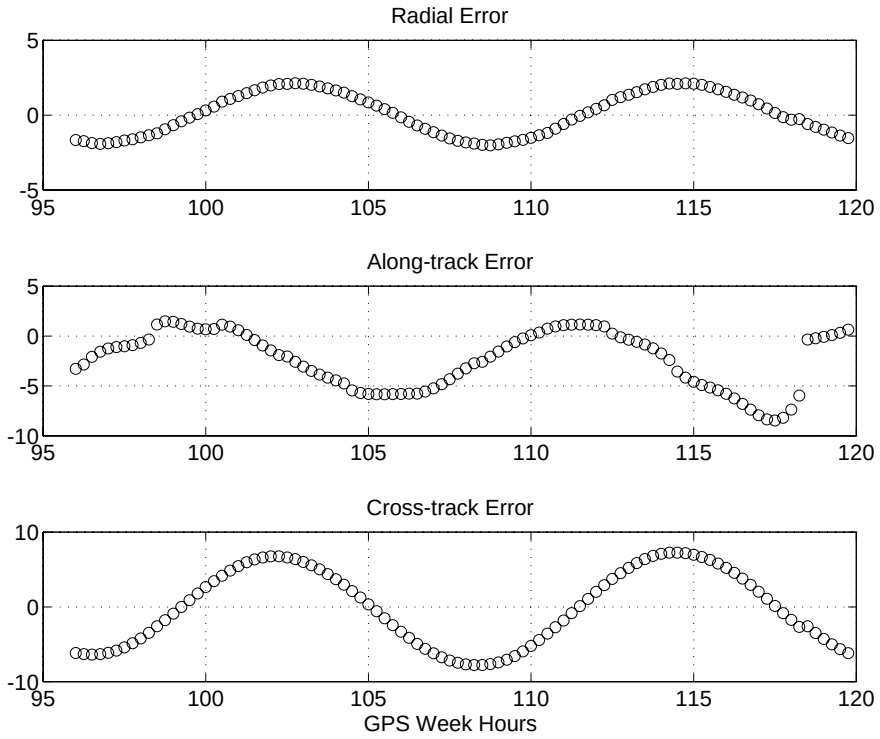

Figure 3.1: Ephemeris Errors (in meters) for Satellite PRN 4

Here shows a 24-hour plot of the ephemeris errors $\Delta\mathbf{R}^k$ in the radial, along-track and cross-track directions for GPS space vehicle PRN 4.

also have to follow the signal specifications defined in the Minimum Operational Performance Standards for WAAS [MOPS]. The MOPS requires the estimated ephemeris errors to be slowly varying with one update every 60 seconds and their magnitudes must be limited to 128 meters [WG2]. Several candidate algorithms will be explored; their advantages and disadvantages will be compared.

The snapshot algorithms have to deal with the situation of an under-determined or over-determined system because the number of reference stations viewing a satellite can change due to rising and setting of satellites. Traditional approaches such as minimum-norm (MN) and least-squares (LS) estimation algorithm will be discussed. In addition, we incorporate *a priori* statistical information about the state variables to be estimated and derive a minimum-variance solution that can be applied to either the under-determined or the over-determined case.

The minimum-norm and least-squares approaches (weighted and non-weighted) and their sensitivity to measurement noise vector will be described first. We then derive a minimum-variance solution for the linear system described by Equation (3.1), using the covariance matrix of measurement noise vector and the *a priori* information matrix about the state vector.

$\mathbf{x}$ will be used to denote the ephemeris error, $\Delta\mathbf{R}^k$, in the following discussions.

3.2.1 Under-determined Systems

When the number of measurements is less than the number of unknowns to be estimated, the traditional least-squares method cannot be used because the design matrix $\mathbf{H}$ is not of full rank. Instead, we can use the minimum-norm method to solve for $\mathbf{x}$. For the linear system of Equation (3.1), there exist an infinite number of possible solutions when the number of measurements M is less than the number of unknowns

N. The cost function for the Minimum-Norm (MN) method is described by

$$J_{MN} = \frac{1}{2}\mathbf{x}^{\mathrm{T}}\mathbf{x} \tag{3.2}$$

The solution which minimizes the above cost function can be described by the following equation

$$\hat{\mathbf{x}}_{MN} = \mathbf{H}^{\mathrm{T}}(\mathbf{H}\mathbf{H}^{\mathrm{T}})^{-1}\mathbf{z} \tag{3.3}$$

For an under-determined system, there are an infinite number of candidates which satisfy $\mathbf{z} = \mathbf{H}\,\mathbf{x}$. The MN estimate is the one with the minimum magnitude (norm). The fitting residue for a MN estimate is zero.

When Stanford started its west coast WAAS testbed in 1994, there were only four reference stations [Walter,a]. Moreover, the one at Stanford was used as a passive user, so its data were not used for correction generations. Therefore, the observations were always under-determined. The minimum-norm solution is sensible, because SA has not been applied to the satellite ephemeris and the GPS ephemeris errors are relatively small as compared to the satellite clock errors [Zumberge]. However, the poor observing geometry renders this estimate very sensitive to measurement noise, outlying measurement(s), data dropouts and the rising or setting of GPS satellites.

The assumption for an MN estimate is that there is no measurement noise ($\mathbf{z} = \mathbf{H}\,\hat{\mathbf{x}}_{MN}$) but measurement noise $\mathbf{v}$ is non-zero. Moreover, the variance of the measurement noise varies. The MN approach does not use this variance information at all.

3.2.2 Over-determined Systems

Either a least-squares (LS) or a weighted least-squares (WLS) estimator can be used when the linear system is over-determined. Both approaches will provide the best linear unbiased estimate (BLUE). Least-squares estimation will be discussed first.

Least-squares (LS) Estimator The cost function for a least-squares estimation problem can be written as follows:

$$J_{LS} = \frac{1}{2}(\mathbf{z} - \mathbf{H}\mathbf{x})^{\mathrm{T}}(\mathbf{z} - \mathbf{H}\mathbf{x}) \tag{3.4}$$

which is simply the sum of squares of the fitting residuals. The well-known solution for an LS estimate is given by the following equation

$$\hat{\mathbf{x}}_{LS} = (\mathbf{H}^{\mathrm{T}}\mathbf{H})^{-1}\mathbf{H}^{\mathrm{T}}\mathbf{z} \tag{3.5}$$

The error covariance matrix which describes the sensitivity of this estimate to the measurement error can be represented by

$$\begin{aligned} \hat{\mathbf{P}}_{LS} &= E[(\mathbf{x} - \hat{\mathbf{x}}_{LS})(\mathbf{x} - \hat{\mathbf{x}}_{LS})^{\mathrm{T}}] \\ &= (\mathbf{H}^{\mathrm{T}}\mathbf{H})^{-1}\mathbf{H}^{\mathrm{T}}Cov(\mathbf{v})\mathbf{H}(\mathbf{H}^{\mathrm{T}}\mathbf{H})^{-1} \end{aligned}$$

If we assume $Cov(\mathbf{v}) = \mathbf{I}\,\sigma_v^2$, then we will have the following equation

$$\hat{\mathbf{P}}_{LS} = (\mathbf{H}^{\mathrm{T}}\mathbf{H})^{-1}\,\sigma_v^2 \tag{3.6}$$

This error covariance matrix is often used in deriving the dilution of precision (DOP)

factors for the GPS navigation applications [Parkinson].

Though the LS estimate minimizes the magnitude of its fitting residuals, $\mathbf{z}-\mathbf{H}\,\hat{\mathbf{x}}_{LS}$, there is no constraint on the magnitude of $\hat{\mathbf{x}}_{LS}$. Unfortunately the LS estimate can exceed the WAAS correction range of ± 128 meters [WG2]. This can be seen from the following equation

$$\hat{\mathbf{x}}_{LS} = \mathbf{x} + (\mathbf{H}^{\mathrm{T}}\mathbf{H})^{-1}\mathbf{H}^{\mathrm{T}}\mathbf{v}$$

The measurement noise vector is amplified by the matrix $(\mathbf{H}^{\mathrm{T}}\mathbf{H})^{-1}\mathbf{H}^{\mathrm{T}}$. Because the geometric condition that is decided by the size of the network and the distance from the reference station to the satellite is poor, the LS estimate is sensitive to the noise. Although the LS algorithm is easy to implement and has been widely used, it is not a good candidate for our ephemeris error estimation problem.

Weighted Least-squares (WLS) Estimator Using the measurement covariance matrix, $\mathbf{W}$, as the weighting matrix, the cost function can be expressed as

$$J_{WLS} = \frac{1}{2}(\mathbf{z}-\mathbf{H}\mathbf{x})^{\mathrm{T}}\mathbf{W}^{-1}(\mathbf{z}-\mathbf{H}\mathbf{x}) \tag{3.7}$$

The corresponding weighted LS estimate is given by the following equation

$$\hat{\mathbf{x}}_{WLS} = (\mathbf{H}^{\mathrm{T}}\mathbf{W}^{-1}\mathbf{H})^{-1}\mathbf{H}^{\mathrm{T}}\mathbf{W}^{-1}\mathbf{z} \tag{3.8}$$

The error covariance matrix which describes the sensitivity of this solution to measurement errors is

$$\begin{aligned}\hat{\mathbf{P}}_{\mathrm{W}LS} &= E[(\mathbf{x}-\hat{\mathbf{x}}_{\mathrm{W}LS})(\mathbf{x}-\hat{\mathbf{x}}_{\mathrm{W}LS})^{\mathrm{T}}] \\ &= (\mathbf{H}^{\mathrm{T}}\mathbf{W}^{-1}\mathbf{H})^{-1}\mathbf{H}^{\mathrm{T}}\mathbf{W}^{-1}Cov(\mathbf{v})\mathbf{W}^{-1}\mathbf{H}(\mathbf{H}^{\mathrm{T}}\mathbf{W}^{-1}\mathbf{H})^{-1}\end{aligned}$$

Since the measurement covariance matrix $Cov(\mathbf{v}) = \mathbf{W}$, we have

$$\hat{\mathbf{P}}_{\mathrm{W}LS} = (\mathbf{H}^{\mathrm{T}}\mathbf{W}^{-1}\mathbf{H})^{-1} \tag{3.9}$$

The WLS method does use the measurement covariance matrix as a weighting factor for the fitting residuals, $\mathbf{z}-\mathbf{H}\,\hat{\mathbf{x}}_{\mathrm{W}LS}$. However, there is no constraint on the magnitude of $\hat{\mathbf{x}}_{\mathrm{W}LS}$. Similar to the LS case, the geometric condition is poor even with the weighting of the noise covariance matrix. This can be seen from the following equation

$$\hat{\mathbf{x}}_{\mathrm{W}LS} = \mathbf{x} + (\mathbf{H}^{\mathrm{T}}\mathbf{W}^{-1}\mathbf{H})^{-1}\mathbf{H}^{\mathrm{T}}\mathbf{W}^{-1}\mathbf{v}$$

Again, this WLS estimate also may exceed the ephemeris error correction range of ± 128 meters [WG2]. Therefore, it is not a good candidate for this ephemeris error estimation problem, although a WLS algorithm is also easy to implement and has been widely used.

3.2.3 Minimum-Variance Estimator

In the above approaches, the state vector, $\mathbf{x}$ ($\Delta\mathbf{R}^k$), was assumed to be an unknown vector. Presumably, these parameters could have assumed any value from $-\infty$ to ∞ and no *a priori* information exists. In many situations, however, we do have some *a*

priori information and it is perhaps more meaningful to regard the unknown vector $\mathbf{x}$ as a random vector with known mean and covariance matrix. If accurate, this *a priori* statistical information can be exploited to produce an estimate with lower error covariance than the minimum-variance (MV) unbiased estimate.

Suppose we have

$$\begin{aligned} E[\mathbf{x}] &= \bar{\mathbf{x}} \\ E[\mathbf{x}\mathbf{x}^{\mathrm{T}}] &= \Lambda \end{aligned}$$

The cost function for the minimum-variance estimation problem which includes Λ and $\mathbf{W}$ can be written as

$$J_{MV} = \frac{1}{2}(\mathbf{x}-\bar{\mathbf{x}})^{\mathrm{T}}\Lambda^{-1}(\mathbf{x}-\bar{\mathbf{x}}) + \frac{1}{2}(\mathbf{z}-\mathbf{H}\mathbf{x})^{\mathrm{T}}\mathbf{W}^{-1}(\mathbf{z}-\mathbf{H}\mathbf{x}) \tag{3.10}$$

Clearly this cost function constrains both the magnitude of $\mathbf{x}-\bar{\mathbf{x}}$ and the magnitude of $\mathbf{z}-\mathbf{H}\mathbf{x}$. The estimate satisfying the above cost function is described by

$$\hat{\mathbf{x}}_{MV} = (\Lambda^{-1} + \mathbf{H}^{\mathrm{T}}\mathbf{W}^{-1}\mathbf{H})^{-1}\mathbf{H}^{\mathrm{T}}\mathbf{W}^{-1}\mathbf{z} \tag{3.11}$$

The error covariance matrix that describes the sensitivity of this solution to measurement error is

$$\begin{aligned} \hat{\mathbf{P}}_{MV} &= E[(\mathbf{x}-\hat{\mathbf{x}}_{MV})(\mathbf{x}-\hat{\mathbf{x}}_{MV})^{\mathrm{T}}] \\ &= (\Lambda^{-1} + \mathbf{H}^{\mathrm{T}}\mathbf{W}^{-1}\mathbf{H})^{-1}(\mathbf{H}^{\mathrm{T}}\mathbf{W}^{-1})Cov(\mathbf{v})(\mathbf{W}^{-1}\mathbf{H})(\Lambda^{-1} + \mathbf{H}^{\mathrm{T}}\mathbf{W}^{-1}\mathbf{H})^{-1} \end{aligned}$$

Since $Cov(\mathbf{v}) = \mathbf{W}$, we have

$$\begin{aligned} \hat{\mathbf{P}}_{MV} &= (\Lambda^{-1} + \mathbf{H}^{\mathrm{T}}\mathbf{W}^{-1}\mathbf{H})^{-1}(\mathbf{H}^{\mathrm{T}}\mathbf{W}^{-1}\mathbf{H})(\Lambda^{-1} + \mathbf{H}^{\mathrm{T}}\mathbf{W}^{-1}\mathbf{H})^{-1} \\ &= (\Lambda^{-1} + \mathbf{H}^{\mathrm{T}}\mathbf{W}^{-1}\mathbf{H})^{-1} \end{aligned} \tag{3.12}$$

This $\hat{\mathbf{x}}_{MV}$ is an unbiased estimate of $\mathbf{x}$ [Bierman], and the estimate in Equation (3.11) is a minimum-variance estimate of $\mathbf{x}$ [Luenberger]. Using the matrix inversion lemma [Kailath,a] it can also be expressed as

$$\hat{\mathbf{x}}_{MV} = \Lambda\mathbf{H}^{T}(\mathbf{H}\Lambda\mathbf{H}^{T} + \mathbf{W})^{-1}\mathbf{z} \tag{3.13}$$

Similarly, the error covariance matrix can be rewritten as

$$\hat{\mathbf{P}}_{MV} = \Lambda - \Lambda\mathbf{H}^{\mathrm{T}}(\mathbf{H}\Lambda\mathbf{H}^{\mathrm{T}} + \mathbf{W})^{-1}\mathbf{H}\Lambda \tag{3.14}$$

A significant difference between the estimate in Equation(3.13) and those of Section 3.2.2 is that the number of observations, M, need not be at least as large as the number of unknowns, N. The estimate, $\hat{\mathbf{x}}_{MV}$, exists as long as the M x M matrix $(\mathbf{H}\Lambda\mathbf{H}^{\mathrm{T}} + \mathbf{W})$ is nonsingular. This is the case for any number of measurements $M > 0$ since $\mathbf{W}$ is positive definite. Since we treat $\mathbf{x}$ as a random vector, it is possible to form a meaningful estimate (namely zero) even with no measurements. Every new measurement simply provides additional information which may modify our original estimate.

The MV estimation approach is well suited for the ephemeris error estimation problem since it incorporates the *a priori* statistics of the ephemeris errors. As such, the MV estimate is less sensitive to the observing geometry, $\mathbf{H}$, and the measurement

noise because the magnitude of $\hat{\mathbf{x}}_{MV}$ is constrained to be near its *a priori* mean, $\bar{\mathbf{x}}$. This MV approach can be used for both under-determined and over-determined systems. In addition, the corrections fit into the WAAS 250 bps message and can be broadcast as a slow message every 120 seconds. For these reasons, we have implemented the MV approach for our snapshot ephemeris error estimation.

Table 3.1 gives the qualitative comparison and summary of the available snapshot methods, including their advantages and disadvantages.

Method	Implementation Complexity	Noise/Geometry Sensitivity	BW Required	UD or OD System	Dependence on Λ
MN	low	low/high	low	UD only	No
LS	low	high/high	high	OD only	No
WLS	low	high/high	high	OD only	No
MV	high	low/low	low	UD and OD	Yes

Table 3.1: Candidate Snapshot Algorithms for Ephemeris Error Estimation
This table gives comparisons for the candidate algorithms of the ephemeris estimation problem. "BW" stands for bandwidth,"OD" stands for over-determined, and "UD" stands for under-determined. Λ is the *a priori* information matrix for the ephemeris errors.

3.2.4 Outlier Detection and Isolation

To provide extremely high integrity corrections, outlying measurements have to be excluded from corrupting the estimates. For an over-determined system, a chi-square

test is employed to check if the snapshot estimate, $\hat{\mathbf{x}}_{\mathrm{MV}}$, is valid by computing

$$\chi^2 = \sum_{i=1}^{i=M} \frac{(z_i - \mathbf{H}_i \hat{\mathbf{x}}_{MV})^2}{\sigma_i^2}$$

The number of degrees of freedom of χ^2 is $M - N$ where M is the number of measurements and N is the number of unknowns. To perform an outlier detection, the system needs to be over-determined ($M > N$). If χ^2 exceeds the detection threshold, there could be outlying measurement(s). This threshold is set to give a probability of false alarm at 10^{-3}. A Studentized t test will be conducted when the chi-square test issues an alarm.

A Studentized t test first computes the chi-square and the "t" distribution by excluding one measurement at a time. The chi-square and the "t" which exclude the i^{th} measurement are

$$\begin{aligned} \chi^2_{(i)} &= \sum_{j=1, j\neq i}^{j=M} \frac{(z_j - \mathbf{H}_j \hat{\mathbf{x}}_{MV,(i)})^2}{\sigma_j^2} \\ t_{(i)} &= \frac{(z_i - \mathbf{H}_i \cdot \hat{\mathbf{x}}_{MV,(i)})}{\sigma_i} \Big/ \sqrt{\chi^2_{(i)}/(M - N - 1)} \end{aligned}$$

Here we use the subscript "(i)" to denote when the i^{th} measurement is excluded from the estimation. An outlier is identified if the following two conditions are both met:

$$\begin{cases} \chi^2_{(i)} < \chi^2_{\mathrm{THRESHOLD}}(M - N - 1) \\ t_{(i)} > t_{\mathrm{THRESHOLD}}(M - N - 1) \end{cases}$$

$\hat{\mathbf{x}}_{\mathrm{MV}}$ and $\hat{\mathbf{P}}_{\mathrm{MV}}$ will be then replaced by $\hat{\mathbf{x}}_{MV,(i)}$ and $\hat{\mathbf{P}}_{MV,(i)}$. The number of degrees of freedom (DOFs) for the chi-square distribution and t distribution is $M - N - 1$

(M has to be greater than $N-1$). If the i^{th} measurement is an outlier, $\chi^2_{(i)}$ should be small (less than the detection threshold) since $z_{c,i}$ has been excluded. However, $t_{(i)}$ will be large since $\hat{\mathbf{x}}_{MV,(i)}$ and $\chi^2_{(i)}$ are computed without using the outlier z_i. A detailed description of the computation of $\hat{\mathbf{x}}_{MV,(i)}$ and $\hat{\mathbf{P}}_{MV,(i)}$ is in Appendix C.

If no outlier can be identified, covariance for the MV estimate will be increased. In Section 3.5, we will study the ephemeris failures and show that these algorithms can reliably detect and exclude the failures.

3.3 Sequential Algorithm

Researchers in the field of geodynamics and surveying usually employ a full dynamic model to help estimate the satellite ephemeris parameters [Litchen]. These models include parameters for the Earth's gravity model and solar pressure. This approach normally requires solving for all satellites simultaneously, and uses observation data longer than one day. A huge amount of computation is involved and real-time processing is more difficult. Instead, we take advantage of the snapshot solutions and employ a new approach.

The snapshot minimum-variance method yields ephemeris error estimates which are still sensitive to measurement noise. For example, Figure 3.2 shows the minimum-variance estimates of the ephemeris errors for satellite PRN 1. However, the estimates do vary slowly and their magnitudes are constrained. In this dissertation, I use a snapshot minimum-variance solution to separate the error sources and then use a Kalman filter to smooth the ephemeris error and ephemeris error rate. Using this approach, the filtered estimates will follow the trends of the snapshot minimum-variance estimates shown in Figure 3.2. However, there won't be discontinuities,

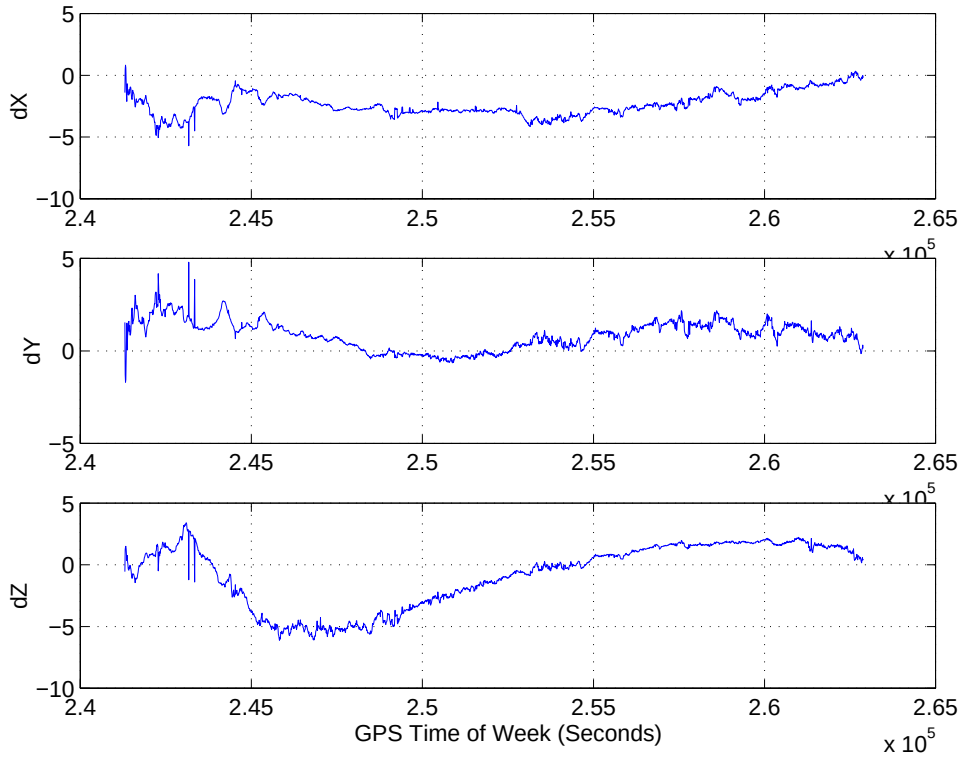

Figure 3.2: Ephemeris Error Estimation Results Using MV Method

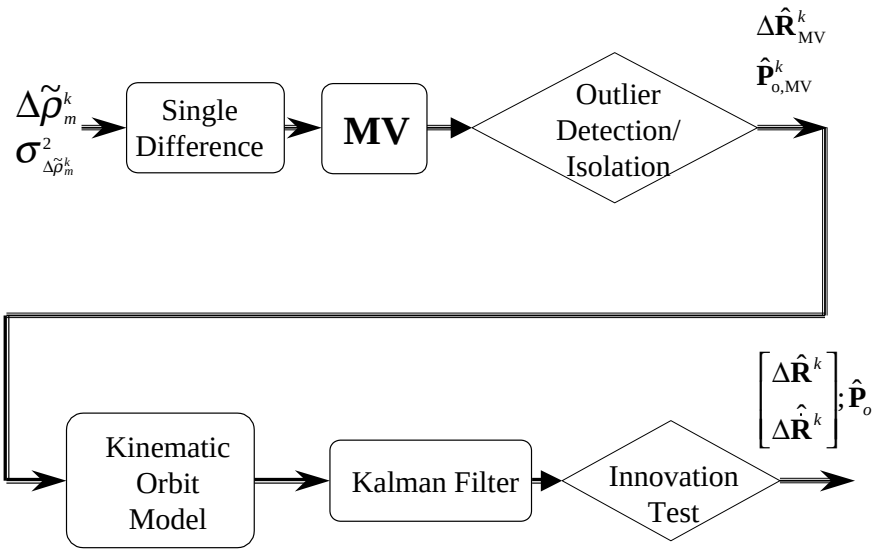

Figure 3.3: Ephemeris Algorithms

The upper part is the snapshot approach while the lower part shows the sequential approach.

which often occur with the snapshot solutions, when there are sudden changes in the number of WRSs viewing a particular satellite. We employ a kinematic model, which uses the estimates from the previous step and current measurements to generate the measurement updated estimate.

The method first uses the solution from the snapshot MV estimate, $\Delta\hat{\mathbf{R}}^k_{MV}$, as the input to a Kalman filter. These observations are then used as the basis for carrying out the sequential estimate of ephemeris and ephemeris velocity errors. The kinematic orbit model will be described first followed by the Kalman filter implementation. Results from the Kalman filter will be presented.

3.3.1 Kinematic Orbit Model

The following kinematic model is used for the ephemeris errors, where we use $\mathbf{X}$ to denote $\Delta\mathbf{R}^k$ and $\Delta\dot{\mathbf{R}}^k$

$$\begin{aligned} \mathbf{X}(k+1) &= \mathbf{X}(k) + \dot{\mathbf{X}}(k) * \mathrm{T} \\ \dot{\mathbf{X}}(k+1) &= \dot{\mathbf{X}}(k) + \mathbf{w}_d(k) \end{aligned}$$

where T is the sampling interval and $\mathbf{w}_d$ is the discrete process noise. The above equation represents a double integrator system driven by a white noise process. In the continuous time domain, it can be described as follows:

$$\ddot{\mathbf{X}}(t) = \mathbf{w}(t) \tag{3.15}$$

The state vector $\mathbf{X}$ represents the errors in the radial, along-track and cross-track directions. Process noise $\mathbf{w}$ accounts for the combined effects due to OCS modeling error in solar pressure [SolarP] and the Earth gravity model [Colombo] [Litchen]. Its autocorrelation function is

$$\begin{aligned} \mathbf{Q} &= E\left[\mathbf{w}\,\mathbf{w}^{\mathrm{T}}\right] \\ &= \begin{bmatrix} Q_{RAD} & \mathrm{X} & \mathrm{X} \\ \mathrm{X} & Q_{ATK} & \mathrm{X} \\ \mathrm{X} & \mathrm{X} & Q_{XTK} \end{bmatrix} \end{aligned}$$

where the off-diagonal terms (marked as X) are much smaller than the diagonal terms.

The above kinematic model for the ephemeris errors can be converted to the

following linear discrete-time system [Bryson]:

$$\mathbf{X}_o(k+1) \;=\; \Phi_o(k)\;\mathbf{X}_o(k) + \Gamma_o(k)\;\mathbf{w}_o(k) \tag{3.16}$$

and the measurement vector is written as

$$\mathbf{Z}_o(k) \;=\; \mathbf{H}_o(k)\;\mathbf{X}_o(k) + \mathbf{v}_o(k) \tag{3.17}$$

where

$$\begin{aligned}
\Phi_o(k) &= \begin{bmatrix} 1 & 0 & 0 & T & 0 & 0 \\ 0 & 1 & 0 & 0 & T & 0 \\ 0 & 0 & 1 & 0 & 0 & T \\ 0 & 0 & 0 & 1 & 0 & 0 \\ 0 & 0 & 0 & 0 & 1 & 0 \\ 0 & 0 & 0 & 0 & 0 & 1 \end{bmatrix} \\
\mathbf{H}_o(k) &= \begin{bmatrix} 1 & 0 & 0 & 0 & 0 & 0 \\ 0 & 1 & 0 & 0 & 0 & 0 \\ 0 & 0 & 1 & 0 & 0 & 0 \end{bmatrix} \\
\mathbf{X}_o &= \left[\Delta\mathbf{R}^k \;\; \Delta\dot{\mathbf{R}}^k\right]^{\mathrm{T}} \\
&= \left[\Delta X^k,\, \Delta Y^k,\, \Delta Z^k,\, \Delta\dot{X}^k,\, \Delta\dot{Y}^k,\, \Delta\dot{Z}^k\right]^{\mathrm{T}}
\end{aligned}$$

The subscript "o" denotes the ephemeris error (orbit), and is distinct from the subscript "c" used for the satellite clock error in Chapter 4. The measurement vector $\mathbf{Z}_o$ is available from the snapshot minimum-variance estimate. The linear system described by Equation (3.16) and (3.17) is time invariant since Φ_o, Γ_o and $\mathbf{H}_o$ are

constant matrices. $\Gamma_o(k)$ is an identity matrix [Bryson].

3.3.2 Kalman Filter Implementation

The Kalman filter is implemented with a measurement update followed by a time update [Brown] [Bryson] [Gelb]. The measurement update for the Kalman filter is the same as the minimum-variance estimate. The estimate for the state vector $\mathbf{X}_o$ at time t_k is

$$\hat{\mathbf{X}}_o(k) = \bar{\mathbf{X}}_o(k) + \mathbf{K}_o(k)(\,\mathbf{Z}_o(k) - \mathbf{H}_o\,\bar{\mathbf{X}}_o(k)\,) \tag{3.18}$$

where $\mathbf{K}_o(k)$ is the Kalman gain matrix

$$\mathbf{K}_o(k) = \bar{\mathbf{P}}_o(k)\,\mathbf{H}_o^{\mathrm{T}}\,(\,\mathbf{H}_o\,\bar{\mathbf{P}}_o(k)\,\mathbf{H}_o^{\mathrm{T}} + \mathbf{R}(k)\,)^{-1} \tag{3.19}$$

and $\bar{\mathbf{X}}_o(k)$ and $\bar{\mathbf{P}}_o(k)$ are the *a priori* information (time updated estimates to be described below).

The updated (*a posteriori*) error covariance matrix for $\hat{\mathbf{X}}_o(k)$ is

$$\hat{\mathbf{P}}_o(k) = \bar{\mathbf{P}}_o(k) - \mathbf{K}_o(k)\,(\,\mathbf{H}_o\,\bar{\mathbf{P}}_o(k)\,\mathbf{H}_o^{\mathrm{T}} + \mathbf{R}(k)\,)\,\mathbf{K}_o(k)^{\mathrm{T}} \tag{3.20}$$

$$= (\,\mathbf{I} - \mathbf{K}_o(k)\mathbf{H}_o\,)\,\bar{\mathbf{P}}_o(k) \tag{3.21}$$

The time update for the Kalman filter predicts the state vector and its error covariance matrix for the next time step. Since process noise is zero mean, the predicted state vector can be written as

$$\bar{\mathbf{X}}_o(k+1) = \Phi_o\,\hat{\mathbf{X}}_o(k) \tag{3.22}$$

and its error covariance matrix is

$$\bar{\mathbf{P}}_o(k+1) \;=\; \Phi_o\,\hat{\mathbf{P}}_o(k)\,\Phi_o^{\mathrm{T}} + \mathbf{Q}_o \tag{3.23}$$

The above results are used as the *a priori* information for the Kalman filter measurement update in the next step.

An innovation test is used to monitor the integrity of our ephemeris error estimate. The innovation test, built as an integral part of the Kalman filter, tests the following innovation process

$$\mathbf{v} \;=\; \mathbf{Z}_o(k) - \mathbf{H}_o(k)\,\bar{\mathbf{X}}_o(k) \tag{3.24}$$

The covariance matrix for the innovation process $\mathbf{v}$ is equal to $(\mathbf{R}(k)+\mathbf{H}_o\,\bar{\mathbf{P}}_o(k)\,\mathbf{H}_o^{\mathrm{T}})$. The innovation test will not try to identify the outlier(s). Instead, the covariance matrix of the filter estimate, $\hat{\mathbf{P}}_o$, will be adjusted if the following condition occurs

$$\parallel v_i \parallel \;>\; \alpha\,\sqrt{(\mathbf{R}(k) + \mathbf{H}_o\,\bar{\mathbf{P}}_o(k)\,\mathbf{H}_o^{\mathrm{T}})_{ii}} \tag{3.25}$$

where the subscript "ii" is used to denote the i^{th} diagonal element. α is a constant factor chosen to be 3.5 [Boguslavskij].

The lower part of Figure 3.3 describes the ephemeris algorithms we implemented in our testbed master station (TMS) software using a Kalman filter and an innovation test.

3.4 Ephemeris Error Estimation Results

Figure 3.4 shows the results using the approach described in Sections 3.2-3.3. An estimate of satellite clock error (labeled as "dB"), which is largely due to SA, is also shown but will not be discussed until Chapter 4. The estimates of ephemeris error in x, y, z components vary more slowly than do the clock errors. This is also verified by Figure 3.4, which shows the rate correction estimates for ephemeris and clock. It is clear from this figure that after the filter has converged (in less than 5 minutes), the ephemeris error components vary ten or more times more slower than do the satellite clock error. Figures 3.4 and 3.4 demonstrate why the clock error has to be broadcast much more frequently than the ephemeris error and why it is important to separate these components to satisfy the WAAS bandwidth limitation.

Figures 3.6 and 3.7 demonstrate how this implementation can accommodate the difficult conditions presented by rising or setting satellites. Low elevation satellites typically have greater uncertainty associated with their measurements. This is due in part to the increased multipath, greater uncertainty in the ionosphere and troposphere delay models and a lower signal to noise ratio. The effect of multipath is worst for rising satellites because the carrier smoothing process takes time to converge. For a WAAS network, it is also the low elevation satellites that experience the most dramatic change in the number of WRSs viewing it. When this change occurs, the snapshot minimum-variance estimate is discontinuous. A real time operational WAAS WMS should be able to coast through these situations, thus guaranteeing a good navigation fix for the user within the coverage area [Tsai,a].

The techniques we developed are able to separate the errors properly, in spite of the relatively poor observation geometry. The minimum-variance approach provides the snapshot estimates which are then smoothed by a Kalman filter. This filtering

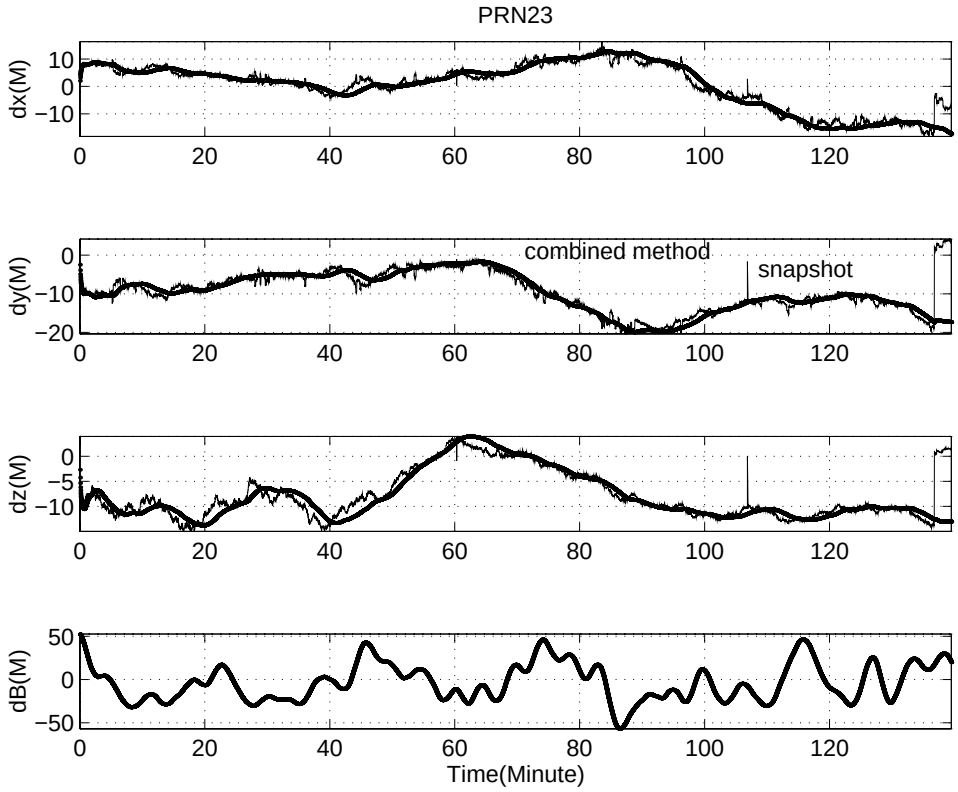

Figure 3.4: Ephemeris and Clock Error Estimates for PRN 23

Jagged lines are snapshot estimates; heavy/smooth lines are estimates using combined minimum-variance and Kalman filter approach.

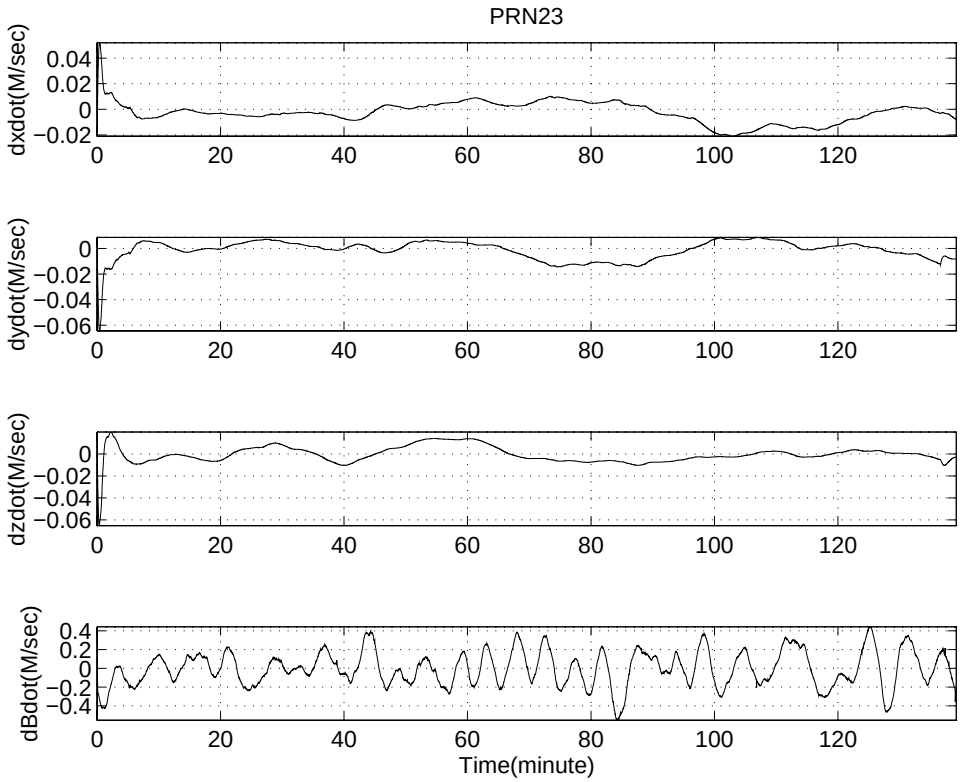

Figure 3.5: Ephemeris and Clock Rate Error Estimates for PRN 23

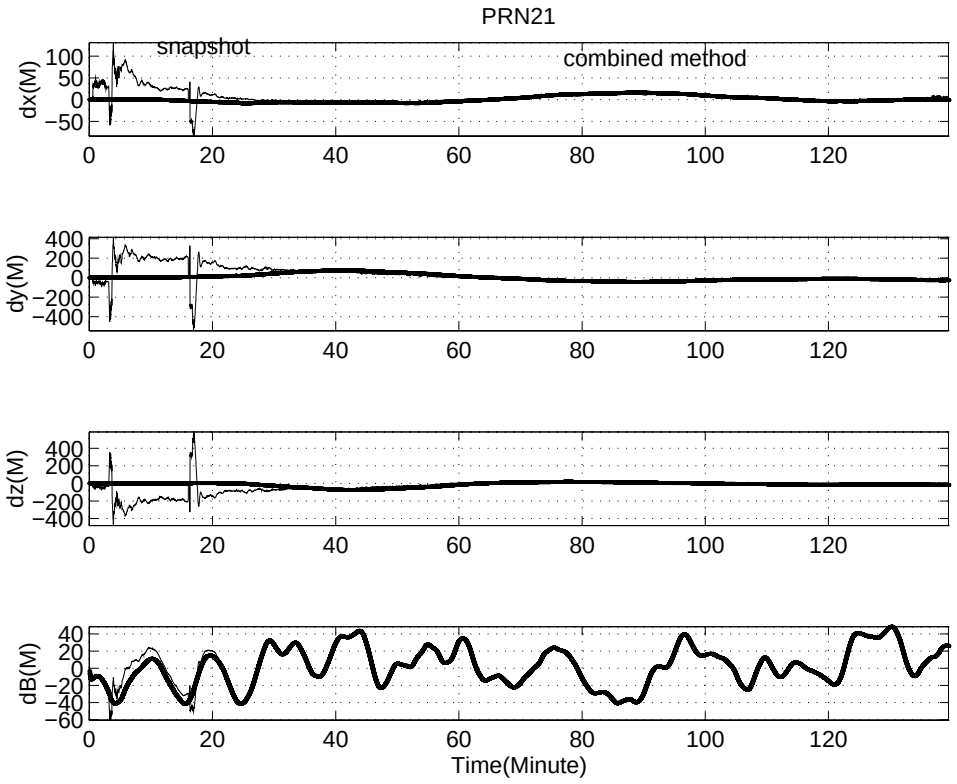

Figure 3.6: Ephemeris and Clock Error Estimates for PRN 21: A Rising Satellite

Jagged lines are snapshot estimates; heavy/smooth lines are estimates using combined minimum-variance and Kalman filter approach.

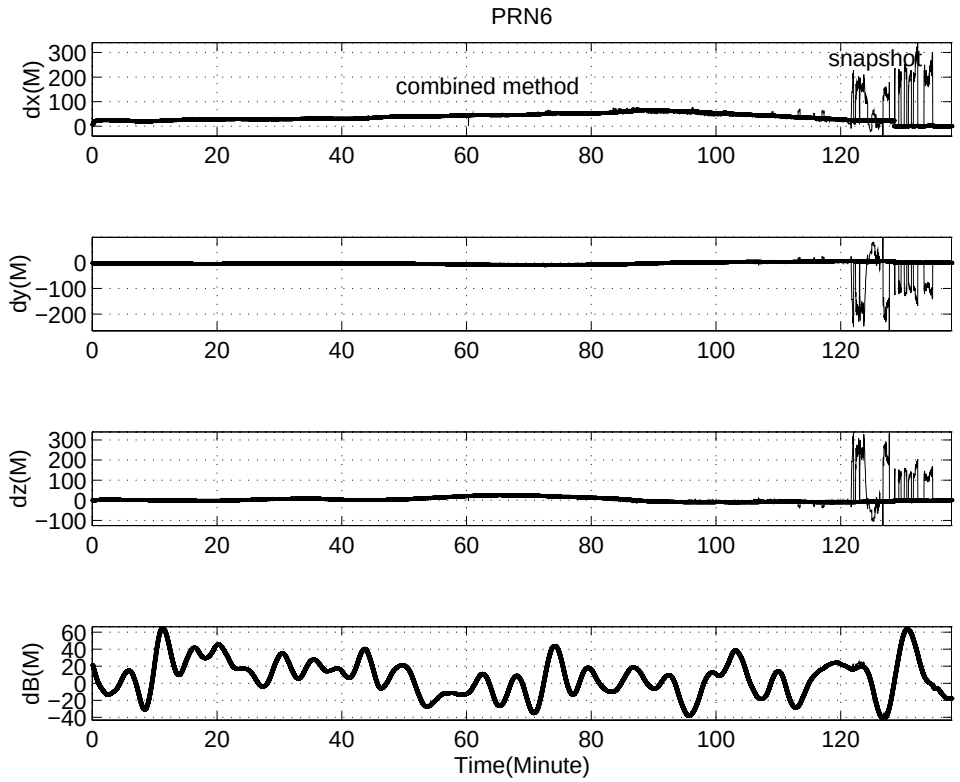

Figure 3.7: Ephemeris and Clock Error Estimates for PRN 6: A Setting Satellite

Jagged lines are snapshot estimates; heavy/smooth lines are estimates using combined minimum-variance and Kalman filter approach.

approach reduces the noise level and provides a time update even when there is a temporary data loss. Our approach also generates fairly good estimates for satellites which are either rising or setting. Our ephemeris corrections vary sufficiently slowly such that they meet the MOPS criteria. In addition, they are less sensitive to noise and geometry.

To prevent outlying measurements from corrupting our estimates, an outlier detection and isolation algorithm was implemented. Next we will describe how our algorithms perform when the system contains failure(s).

3.5 Satellite Ephemeris Data Degradations

The GPS Operational Control Segment (OCS) may upload incorrect ephemeris parameters. Although the OCS has implemented a real time process to guard against these kind of errors [Crum] [Lala], it is necessary for WAAS to monitor the validity of the broadcast ephemeris.

In this section, real data which contains maneuvering satellites is used for study. These maneuvering satellites were declared as "unhealthy" by the OCS several hours before the satellites were re-positioned. Even so, this case is examined as an ephemeris failure to see if our algorithms can detect and isolate this kind of failure before it corrupts the estimation process [Tsai,c]. Furthermore, this study also examines if our algorithms can rapidly issue a "don't use" message for the degraded satellite.

Ephemeris failures are the errors in the broadcast ephemeris that cannot be managed with a correction every 60 seconds or the error magnitude is too big to fit into the message. Ephemeris failures would affect both the master clock filter and the CVTT filter.

For the master clock filter, where the measurements are already corrupted by SA, ephemeris failures will cause an extra error in the estimate. The effect will be small if the error caused by this failure in the range direction is small. However, if the error caused by the failure is large, the estimate for the master clock filter will no longer be valid.

Without proper and timely exclusion, the ephemeris failures will invalidate the synchronization of the pseudorange residuals. Recall from Chapter 2 that we assumed that the range error caused by the ephemeris error is negligible after single differencing because the line of sight difference is small. If this assumption is not true, then the synchronized pseudorange residuals are no longer decoupled. Further processing of the ephemeris and clock error estimation could be dangerous because the resulting corrections can provide hazardous misleading information to WAAS users.

Figure 3.8 shows the synchronized pseudorange residuals of all TRSs for PRN 7. This data was collected on July 29 of 1997. PRN 7 was broadcast as "unhealthy" by the OCS between GPS time 297060 and 319790 (seconds). It can be seen from Figure 3.8 that the OCS did broadcast a new set of ephemeris parameters (to flag the satellite as "unhealthy") several hours before it re-positioned the satellite so that GPS users will not use that satellite for navigation.

For a healthy satellite, the synchronized pseudorange residuals from all reference stations agree to within a few decimeters. The dispersion between their synchronized pseudorange residuals is small because the ephemeris errors are small and the line of sight vectors from satellite to reference stations are very close. However, when the satellite is being re-positioned, the synchronized pseudorange residuals start to grow in magnitude and the dispersion increases as can be observed from Figure 3.8.

We divide Figure 3.8 into four regions. Region 1 is when the satellite is declared

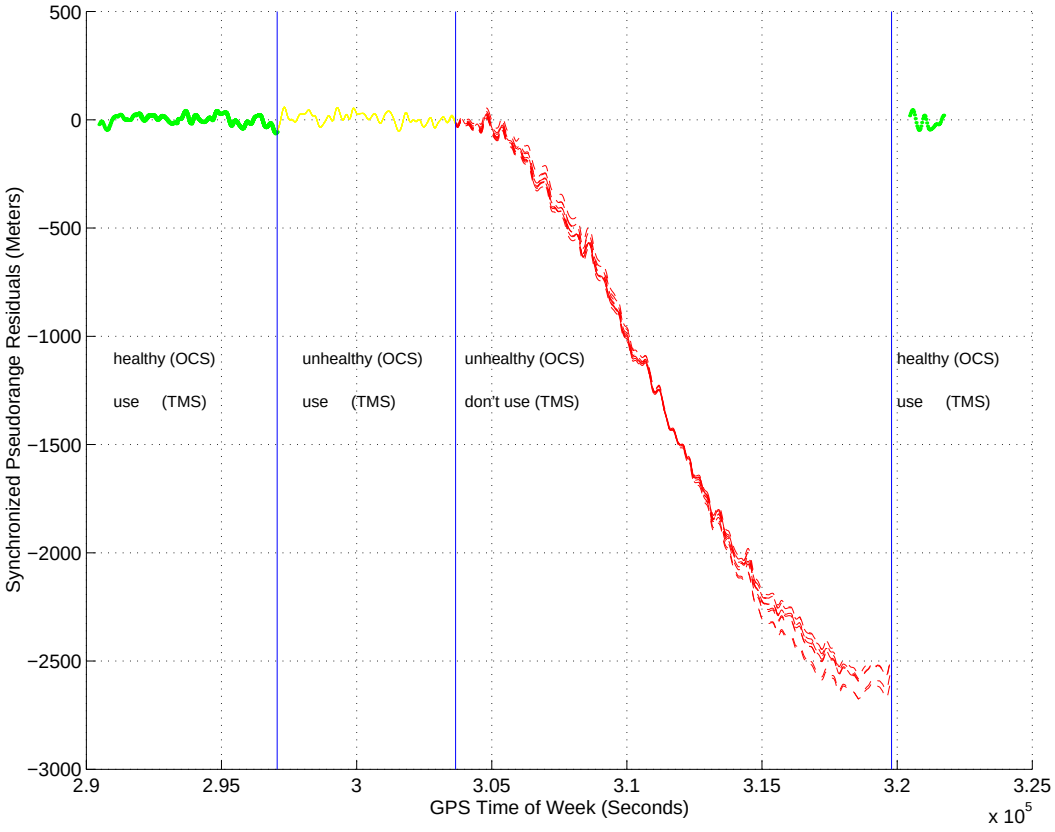

Figure 3.8: Synchronized Pseudorange Residuals for A Maneuvering Satellite PRN 7

This plot is divided into four regions, starting from the left. Region 1 is when PRN 7 is healthy and can be used. Region 2 is when PRN 7 is "unhealthy" but can be used. Region 3 is when PRN 7 is "unhealthy" and "don't use". Region 4 is when PRN 7 is healthy and can be used again.

"healthy" by OCS broadcast and is declared usable by our TMS. Region 2 is when the satellite is declared "unhealthy" by OCS broadcast and is still declared usable by our TMS. Region 3 is when the satellite is declared "unhealthy" by OCS broadcast and the TMS declares "don't use". Region 4 is when the satellite is declared "healthy" again by OCS broadcast and is also declared usable by our TMS.

In Region 2 of Figure 3.8, though the satellite is "unhealthy", its synchronized pseudorange residuals have not started to drift away. Computed corrections have not caused any alarm on the chi-square test. No outlier isolation has been attempted. Corrections for PRN 7 are broadcast as well the other satellites, because no user errors will result.

In Region 3 of Figure 3.8, the satellite is "unhealthy" and the synchronized pseudorange residuals have started to disperse, because the ephemeris errors are getting larger. Computed ephemeris error estimates start to grow in both position and velocity. The chi-square test in our ephemeris algorithms starts to issue alarms but no outlier(s) can be identified because this ephemeris failure is common to all TRS. However, in the CVTT filter, our algorithm not only detects there could be outlying measurement(s) but also makes the correct isolation. Single differenced measurement $(\Delta\tilde{\rho}^j_m - \Delta\tilde{\rho}^j_M)$ for PRN 7 diverges from measurements of the other satellites. Therefore, PRN 7 is not used in CVTT synchronization and the pseudorange residuals are well synchronized and decoupled. Generated ephemeris error corrections for PRN 7 continue to grow in magnitude. Eventually the corrections cannot be contained in the ± 128 range of the slow correction. and a "don't use" flag for PRN 7 is broadcast.

In Region 4, the satellite has been moved to the new orbit and a new set of ephemeris parameters is generated and broadcast. The satellite is "healthy" and

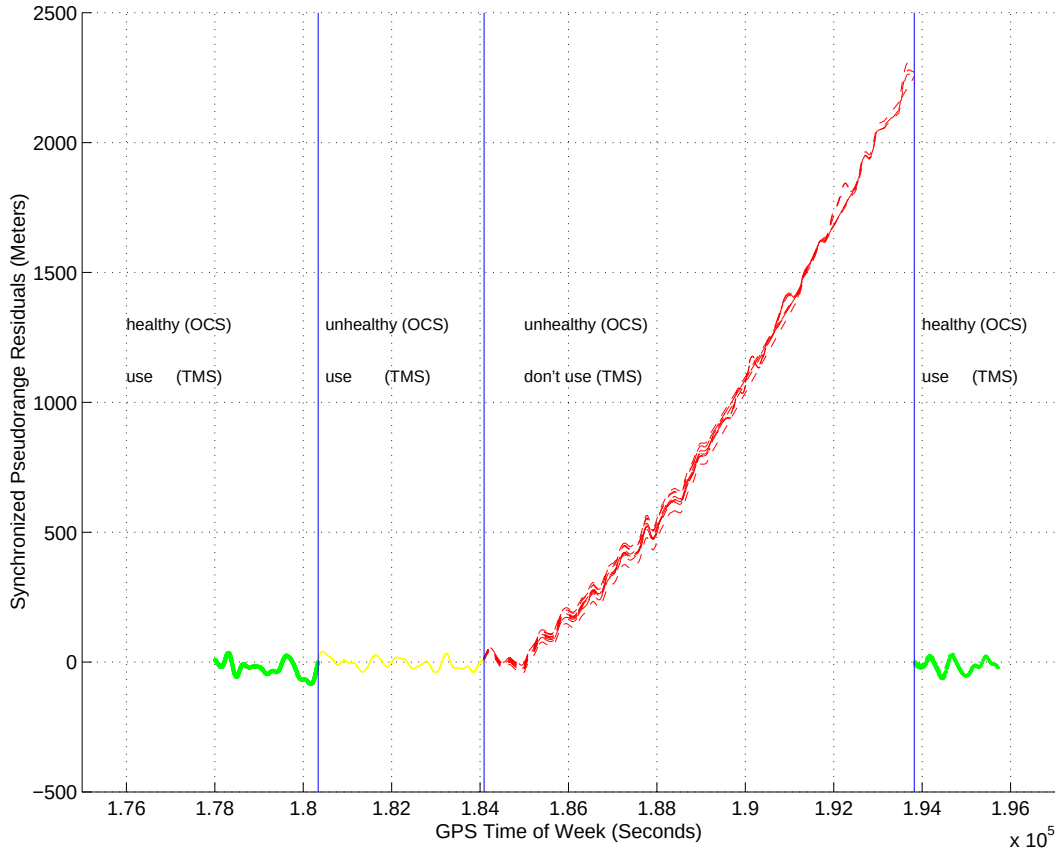

Figure 3.9: Synchronized Pseudorange Residuals for A Maneuvering Satellite PRN 14

This plot is divided into four regions, starting from the left. Region 1 is when PRN 14 is healthy and can be used. Region 2 is when PRN 14 is "unhealthy" but can be used. Region 3 is when PRN 14 is "unhealthy" and "don't use". Region 4 is when PRN 14 is healthy and can be used again.

usable by all GPS users again.

Our ephemeris algorithms continue to estimate ephemeris errors even though a "don't use" flag is raised. Therefore, it is important for our algorithm to detect when the satellite is usable. When the satellite is healthy again, its broadcast ephemeris parameters are valid and usable. The pseudorange residuals from all TRSs will be valid and can be used to generate corrections. Our snapshot MV estimates issue no alarm because the chi-square test passes and the Kalman filter is reset so we can use the satellite immediately. The decision on "use" and "don't use" of our prototype WAAS does not rely on the GPS broadcast of "healthy" and "unhealthy" at all.

Similarly, Figure 3.9 shows the synchronized pseudorange residuals of all TRSs for PRN 14 on August 11, 1997. Region 1 shows when PRN 14 is healthy and can be used. Region 2 shows when PRN 14 is "unhealthy" but can be used. Region 3 shows when PRN 14 is "unhealthy" and "don't use". Region 4 shows when PRN 14 is healthy and can be used again.

In addition to these two cases, we have also experienced several other satellite maneuvers while running our NSTB master station in real time. Once again our algorithms can still use the "unhealthy" (OCS broadcast) satellite until the errors exceed the slow correction range and a "don't use" (our algorithm) message will be reliably produced in time. The decision on "use" and "don't use" does not rely on the GPS broadcast of "healthy" or "unhealthy."

3.6 Summary

There are many candidate methods which can be used to estimate satellite ephemeris errors. We have surveyed these approaches and compared their advantages and disadvantages (Table 3.1). The preferred ephemeris estimator is a snapshot minimum-variance method combined with a Kalman filter which employs a kinematic model. Estimation results from the ephemeris algorithms are presented.

Protection against outlying measurements has been integrated into the ephemeris algorithms. A chi-square test is used for outlier detection and a Studentized t test is used for outlier isolation. An innovation test is built in the Kalman filter. Ephemeris failures caused by satellite maneuvering are studied and tested against our algorithms. The results demonstrated the robustness of our algorithms. Furthermore, the decision on "use" and "don't use" for the observed satellites does not rely on the GPS broadcast of "healthy" and "unhealthy."

Chapter 4

Satellite Clock Estimation Algorithms

GPS uses atomic clocks on board the satellites to provide precise time references. However, this timing accuracy is degraded purposefully by the U.S. Government to deny the full accuracy of the GPS system to un-authorized users. This practice of degradation is known as Selective Availability (SA). Only authorized users are capable of removing this error to attain the precise positioning service (PPS) accuracy. WAAS has to generate an estimate of clock error to remove SA.

The GPS satellite clock error include two parts, SA and the true atomic clock error. The time constant of SA is about 120 seconds [Matchett] [Studenny] while the error of the atomic clock changes very slowly (because of highly stable atomic clock) [McCaskill]. Appendix D discusses how to separately estimate this slow component. The algorithms described in this chapter focus on estimating the fast component.

This chapter discusses the algorithms we developed and tested to estimate the satellite clock errors. Once again, a snapshot algorithm is discussed first followed by

a Kalman filter implementation which generates the smoothed estimate of the clock error and clock error rate. A second order Gauss Markov process model is used to model SA. This model has been adopted by the RTCA for receiver testing purposes [Studenny]. Outlier detection and isolation will be discussed in Section 4.2. This chapter concludes with results from satellite clock failure simulation.

4.1 Clock Error Measurements

In the overall processing chain, clock error estimation follows ephemeris error estimation immediately (Figure 4.1). Clock error measurements for all satellites are derived from combining the synchronized pseudorange residuals with the ephemeris error estimate, $\Delta\hat{\mathbf{R}}^k$. This real time process will be described below.

The clock error measurement for the k^{th} satellite from the m^{th} WRS can be expressed as follows:

$$\begin{aligned} z_{c,m}^k &= \Delta\hat{\mathbf{R}}^k \cdot \mathbf{1}_m^k - \Delta\tilde{\rho}_m^k \\ &= \Delta B^k + n_m^k \end{aligned} \tag{4.1}$$

and its measurement variance can be computed as follows:

$$\sigma_{c,m}^{k\ 2} = \mathbf{1}_m^{k\ \mathrm{T}} \cdot \hat{\mathbf{P}}_3 \cdot \mathbf{1}_m^k + \sigma_{\Delta\tilde{\rho}_m^k}^2 \tag{4.2}$$

where $\hat{\mathbf{P}}_3$ is the upper 3 x 3 diagonal block matrix from the ephemeris algorithm (Equation (3.18)). The subscript "c" is used to denote clock. This variance combines the covariance matrix of the ephemeris error estimate and the variance of the original measurement, i.e., the synchronized pseudorange residual.

In matrix form, Equation (4.1) can be rewritten as

$$\mathbf{z}_c = \mathbf{H}_c \, \Delta B^k + \mathbf{n}_c \tag{4.3}$$

where $\mathbf{H}_c$ is a column vector with all 1's and $\mathbf{n}_c$ is the measurement noise with covariance matrix $\mathbf{W}_c$ whose diagonal elements are given by Equation (4.2). Equation (4.1) will be the basic clock error measurements for our snapshot clock algorithm.

4.2 Snapshot Algorithm

The linear system described by Equation (4.1) has only one unknown, ΔB^k. We use a weighted least-squares (WLS) method to derive the estimate for satellite clock error.

Unlike the ephemeris algorithm which uses *a priori* information to alleviate the problem of bad observation geometry, Equation (4.1) is always well conditioned and over-determined. The WLS estimate is expressed as follows:

$$\Delta \hat{B}^k_{snap} = (\mathbf{H}_c^{\mathrm{T}} \mathbf{W}_c^{-1} \mathbf{H}_c)^{-1} \mathbf{H}_c^{\mathrm{T}} \mathbf{W}_c^{-1} \mathbf{z}_c \tag{4.4}$$

$$\hat{P}^k_{c,snap} = (\mathbf{H}_c^{\mathrm{T}} \mathbf{W}_c^{-1} \mathbf{H}_c)^{-1} \tag{4.5}$$

where $\mathbf{W}_c$ is a diagonal matrix whose elements are computed in Equation(4.2). $\hat{P}^k_{c,snap}$ is the variance of the weighted least-squares estimate.

This snapshot approach only generates the clock error estimate while we need to have the error rate estimate as well to coast through periods of data dropouts. We will discuss the sequential algorithm in the next section.

To guarantee integrity in the corrections, estimates computed by Equation (4.4)

have to be examined by a chi-square test by computing

$$\chi^2 = \sum_{i=1}^{i=M} \frac{(z_{c,i} - \Delta\hat{B}^k_{snap})}{\sigma^2_{c,i}}$$

If the computed χ^2 exceeds the threshold, there could be outlier(s) in the measurements. If an alarm is raised, a Studentized t test is used to isolate the outlying measurement(s).

A Studentized t test first computes the chi-square and the "t" distribution by excluding one measurement at a time. The chi-square and the "t" which exclude the i^{th} measurement are

$$\chi^2_{(i)} = \sum_{j=1, j\neq i}^{j=M} \frac{(z_{c,j} - \Delta\hat{B}^k_{snap,(i)})^2}{\sigma^2_{c,j}}$$

$$t_{(i)} = \frac{(z_{c,i} - \Delta\hat{B}^k_{snap,(i)})}{\sigma_{c,i}} / \sqrt{\chi^2_{(i)}/(M-N-1)}$$

where $\Delta\hat{B}^k_{snap,(i)}$ is the new estimate with the i^{th} measurement excluded. Here we use the subscript "(i)" to denote when the i^{th} measurement is excluded from the estimation. An outlier is identified if the following two conditions

$$\begin{cases} \chi^2_{(i)} < \chi^2_{\text{THRESHOLD}}(M-N-1) \\ t_{(i)} > t_{\text{THRESHOLD}}(M-N-1) \end{cases}$$

are both met. If the i^{th} measurement is an outlier, $\chi^2_{(i)}$ should be small (less than the detection threshold) since $z_{c,i}$ has been excluded. However, $t_{(i)}$ will be large since $\Delta\hat{B}^k_{snap,(i)}$ and $\chi^2_{(i)}$ are computed without using the outlier $z_{c,i}$. $\hat{B}^k_{snap}$ and $\hat{P}^k_{c,snap}$ will be then replaced by $\hat{B}^k_{snap,(i)}$ and $\hat{P}^k_{c,snap,(i)}$. A detailed description of the computation

of $\hat{B}^k_{snap,(i)}$ and $\hat{P}^k_{c,snap,(i)}$ is in Appendix C. The number of degrees of freedom for the chi-square distribution and t distribution is $M - N - 1$ (M has to be greater than $N - 1$).

If no outlier is identified, then the covariance for the clock estimate will be increased. In Section 4.5, we study the satellite clock failures and show that these algorithms can reliably detect and exclude ramp and step type failures.

4.3 Sequential Algorithm

Outputs from the snapshot clock estimator, the estimate and its variance (Equations (4.4) and (4.5)), are treated as measurements by the sequential algorithm, which is implemented as a Kalman filter.

We adopt a second order Gauss Markov process model [Matchett] [Studenny] to describe the clock dynamics. It can be expressed by an ordinary differential equation as follows:

$$\ddot{x} + 2\,\beta\,\omega_0\,\dot{x} + \omega_0^2\,x \;\; = \;\; c\,w \tag{4.6}$$

where ω_0 is the natural frequency and β is the damping ratio which is less than 1 (under-damped system). w is additive white Gaussian noise with unity power spectral density. RTCA has proposed the following parameters for the model [van Graas]

$$\begin{aligned} \beta &= 1/\sqrt{2} \\ \omega_0 &= 0.012 \text{ rad/s} \\ c^2 &= 0.002585\ m^2 \end{aligned}$$

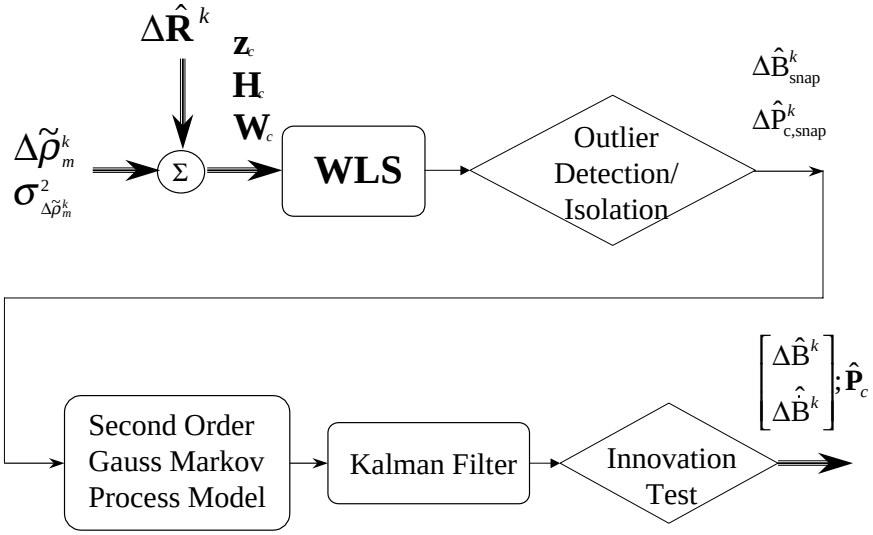

Figure 4.1: Stanford TMS Clock Algorithms

The upper part shows the snapshot algorithm and the lower part is the sequential algorithm.

This model results in a random process with a standard deviation of 23 meters in range error and 0.28 m/s in range error rate. The time constant for the system is approximately 120 seconds.

Equation (4.6) can be expressed as a linear, time-invariant, discrete-time system as follows:

$$\mathbf{X}_c(k+1) = \Phi_c(k)\mathbf{X}_c(k) + \mathbf{G}_c(k)\mathbf{w}_c(k) \tag{4.7}$$

with the measurement equation:

$$\Delta\hat{B}^k_{snap} = \mathbf{H}_c(k)\mathbf{X}_c(k) + v_c(k) \tag{4.8}$$

where

$$\begin{aligned} \mathbf{X}_c &= \left[\Delta B^k \;\; \Delta\dot{B}^k\right]^{\mathrm{T}} \\ \mathbf{H}_c &= [1 \;\; 0] \end{aligned}$$

Measurement noise $v_c(k)$ has the variance $\hat{P}^k_{c,snap}$ from snapshot clock estimator. If the update interval is once per second, then the matrices in Equation (4.7) become:

$$\begin{aligned} \Phi_c &= \begin{bmatrix} 0.9999284 & 0.9915387 \\ -0.0001428 & 0.9831014 \end{bmatrix} \\ \mathbf{G}_c &= \begin{bmatrix} 0.0146771 & 0.0252060 \\ 0 & 0.0504133 \end{bmatrix} \end{aligned}$$

We have implemented a Kalman filter to estimate the state vector $\mathbf{X}_c$, which includes clock error and clock error rate. The Kalman estimate for the state vector

$\mathbf{X}_c$ at time t_k is

$$\hat{\mathbf{X}}_c(k) = \bar{\mathbf{X}}_c(k) + \mathbf{K}_c(k)(\,\Delta\hat{B}^k_{snap} - \mathbf{H}_c\,\bar{\mathbf{X}}_c(k)\,) \tag{4.9}$$

where $\bar{\mathbf{X}}_c(k)$ and $\bar{\mathbf{P}}_c(k)$ are the *a priori* information (time updated estimates to be described below). $\mathbf{K}_c(k)$ is the Kalman gain matrix

$$\mathbf{K}_c(k) = \bar{\mathbf{P}}_c(k)\,\mathbf{H}_c^{\mathrm{T}}\,(\,\mathbf{H}_c\,\bar{\mathbf{P}}_c(k)\,\mathbf{H}_c^{\mathrm{T}} + R_c(k)\,)^{-1} \tag{4.10}$$

and the updated (*a posteriori*) error covariance matrix for $\hat{\mathbf{X}}_c(k)$ is [Brown] [Kailath,b]

$$\hat{\mathbf{P}}_c(k) = \bar{\mathbf{P}}_c(k) - \mathbf{K}_c(k)\,(\,\mathbf{H}_c\,\bar{\mathbf{P}}_c(k)\,\mathbf{H}_c^{\mathrm{T}} + R_c(k)\,)\,\mathbf{K}_c(k)^{\mathrm{T}} \tag{4.11}$$

$$= (\,\mathbf{I} - \mathbf{K}_c(k)\mathbf{H}_c\,)\,\bar{\mathbf{P}}_c(k) \tag{4.12}$$

The time update for the Kalman filter predicts the state vector and its error covariance matrix for the next time step. The superscript bar is used to denote the predicted estimate and covariance matrix. Since the process noise is zero mean, this predicted state vector can be written as

$$\bar{\mathbf{X}}_c(k+1) = \Phi_c\;\hat{\mathbf{X}}_c(k) \tag{4.13}$$

and its error covariance matrix is

$$\bar{\mathbf{P}}_c(k+1) = \Phi_c\,\hat{\mathbf{P}}_c(k)\,\Phi_c^{\mathrm{T}} + \mathbf{Q}_c \tag{4.14}$$

The above results are used as the *a priori* information for the Kalman filter measurement update in the next time step t_{k+1}.

Figure 3.4 of Chapter 3 shows the ephemeris and clock error estimates for satellite PRN 23 during a period of about 2 hours. The estimates of clock error vary faster than do the ephemeris errors. This is also verified by Figure 3.4, which shows the rate correction estimates for ephemeris and clock. After the filter has converged (in less than 5 minutes), the ephemeris error components vary ten or more times more slowly than do the satellite clock error. Figures 3.4 and 3.4 show that the clock error has to be broadcast much more frequently than the ephemeris error. It is important to separate these components to satisfy the slow and fast message format. After all, WAAS does not have the bandwidth to broadcast the ephemeris corrections as often as the clock corrections. In addition, Figures 3.6 and 3.7 demonstrate that our algorithms can accommodate the difficult conditions presented by the rising or setting satellites.

Before the newly generated clock estimates and their covariance matrices are used as corrections, an innovation test is executed to guarantee that the difference between the prediction and measurement is bounded by the covariance. Once again, the innovation test is built as an integral part of the Kalman filter. The innovation process

$$v(k) \;=\; \hat{B}^{k}_{snap} - \mathbf{H}_c(k)\,\bar{\mathbf{X}}_c(k) \tag{4.15}$$

The variance for the innovation process $v(k)$ is equal to $R_c(k)+\mathbf{H}_c\,\bar{\mathbf{P}}_c(k)\,\mathbf{H}_c^{\mathrm{T}}$, a scalar. $R_c(k)$ is the variance of the measurement and $\bar{\mathbf{P}}_c(k)$ is the time-updated covariance matrix from the Kalman filter. The covariance matrix of the filter estimate, $\hat{\mathbf{P}}_c$, will be adjusted if the following condition occurs

$$\parallel v(k) \parallel \;>\; \alpha\sqrt{(R_c(k) + \mathbf{H}_c\,\bar{\mathbf{P}}_c(k)\,\mathbf{H}_c^{\mathrm{T}})} \tag{4.16}$$

α is a constant factor chosen to be 3.5 [Boguslavskij].

Figure 4.1 details our implementation of clock algorithms. The upper part in the figure is the snapshot method while the lower part is the Kalman filter implementation. These algorithms involve a chi-square test for fault detection, a studentized t test for fault isolation and an innovation test.

4.4 UDRE Estimation and Validation

The GPS satellites broadcast a user range accuracy (URA) parameter broadcast in its navigation data broadcast to indicate expected range accuracy [SPS]. Similarly, WAAS uses a user differential range error (UDRE) to indicate the uncertainty in the corrected pseudoranges. UDRE tries to bound the error due to the ephemeris and clock corrections. The WAAS messages send a discrete UDRE indicator (UDREI), that occupies 4 bits for each satellite, to account for user differential range error.

The 4-bit UDREIs are used for the evaluation of the $\sigma^2_{UDRE}{}'s$, indicating the accuracy of combined fast and slow error corrections, but not including the accuracy of the ionospheric delay corrections [Chao,d] [MOPS].

The WAAS users employ a weighted least-squares (WLS) method to solve for their position estimate and estimate covariance, and the WLS estimator uses the UDREI that comes from the WAAS broadcast and the measurement variance from the receiver. Table 4.4 shows the transform between UDREI, UDRE and σ^2_{UDRE} .

4.4.1 UDRE Estimation

UDRE is a single number but it must be valid for any user inside any part of the reference network. Therefore the line of sight vector from the reference station to the

UDREI	**UDRE** (Meters)	σ^2_{UDRE} (Meters^2)
0	0.75	0.0520
1	1.00	0.0924
2	1.25	0.1444
3	1.75	0.2830
4	2.25	0.4678
5	3.00	0.8315
6	3.75	1.2992
7	4.50	1.8709
8	5.25	2.5465
9	6.00	3.3260
10	7.50	5.1968
11	15.0	20.7870
12	50.0	230.9661
13	150	2078.695
14	Not Monitored	Not Monitored
15	Do Not Use	Do Not Use

Table 4.1: UDRE and UDREI Transform

satellite must be used. We use a weighted least-squares to generate the estimate of UDRE. This algorithm uses the following inputs:

1. $\mathbf{R}$ is the measurement covariance matrix of the synchronized pseudorange residuals.

2. $\hat{\mathbf{P}}$ is the covariance matrix which combines $\hat{\mathbf{P}}_o$ (from ephemeris estimate) and $\hat{\mathbf{P}}_c$ (from clock estimate).

3. $\mathbf{H}$ is the design matrix composed of the unit length line of sight vectors and satellite clock terms. The line of sight vectors cover all users inside the reference network.

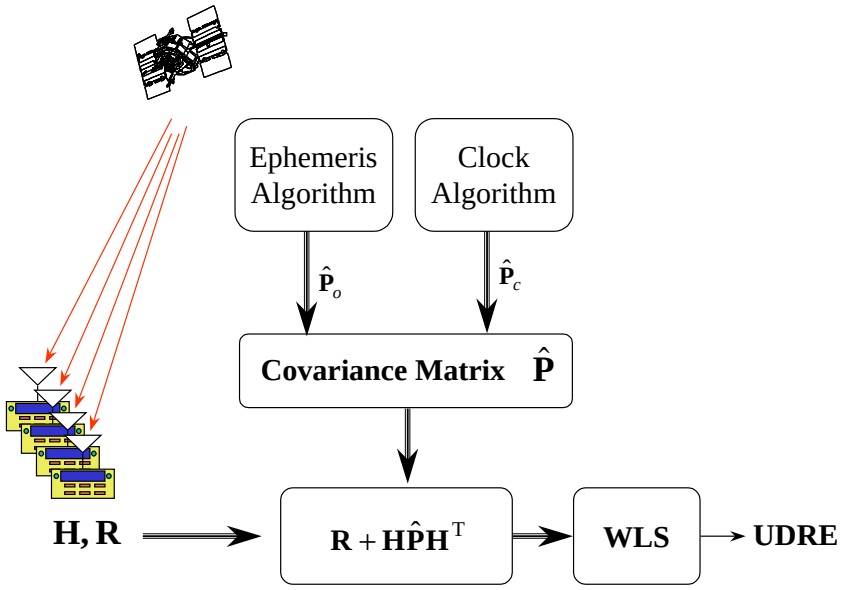

Figure 4.2: UDRE Estimation

The covariance matrix for combined ephemeris (slow) and clock (fast) error estimates are computed as follows:

$$\mathbf{P}_{\mathrm{UDRE}} = \mathbf{R} + \mathbf{H}\hat{\mathbf{P}}\mathbf{H}^{\mathrm{T}} \tag{4.17}$$

The estimated σ^2_{UDRE} is computed as follows

$$\sigma^2_{\mathrm{UDRE}} = \left(\sum_{i=1}^{i=M} \frac{1}{\mathbf{P}_{\mathrm{UDRE},ii}} \right)^{-1} \tag{4.18}$$

where $\mathbf{P}_{\mathrm{UDRE},ii}$ is the i^{th} diagonal element of the covariance matrix $\mathbf{P}_{\mathrm{UDRE}}$. Figure 4.2 shows the block diagram that describes how we compute the UDRE estimate.

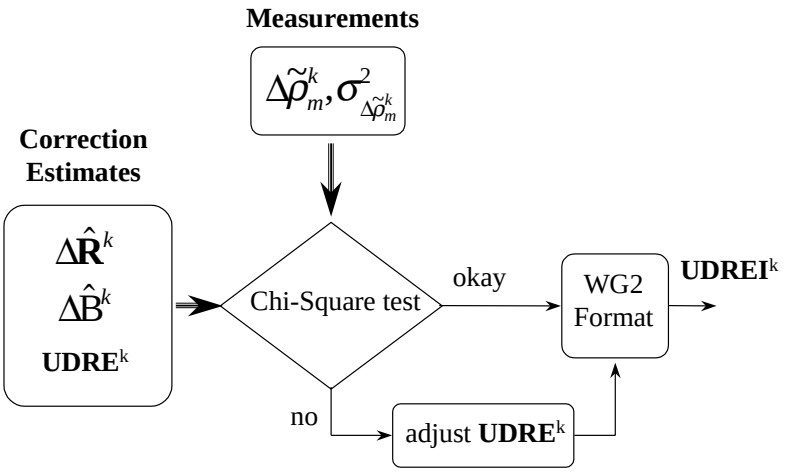

Figure 4.3: UDRE Validation

4.4.2 UDRE Validation

To ensure that UDRE is a valid estimate, we need to examine the residuals of the fit. First, a chi-square test to test the goodness of fit is conducted as follows

$$\chi^2 = \sum_{i=1}^{i=M} \frac{\Delta\tilde{\rho}_i^k - \Delta\hat{\mathbf{R}}^k \cdot \mathbf{1}_i^k + \Delta\hat{B}^j}{\sigma^2_{\Delta\tilde{\rho}_i^k}}$$

As shown in Figure 4.3, the correction estimates ($\Delta\hat{\mathbf{R}}^k$, $\Delta\hat{B}^k$ and UDRE^k) from our ephemeris and clock estimators and synchronized pseudorange residuals for the k^{th} satellite are used in the chi-square test. If the chi-square test fails, then the UDRE estimate has to adjusted or "bumped". The UDRE estimate is converted to UDREI for broadcast [MOPS].

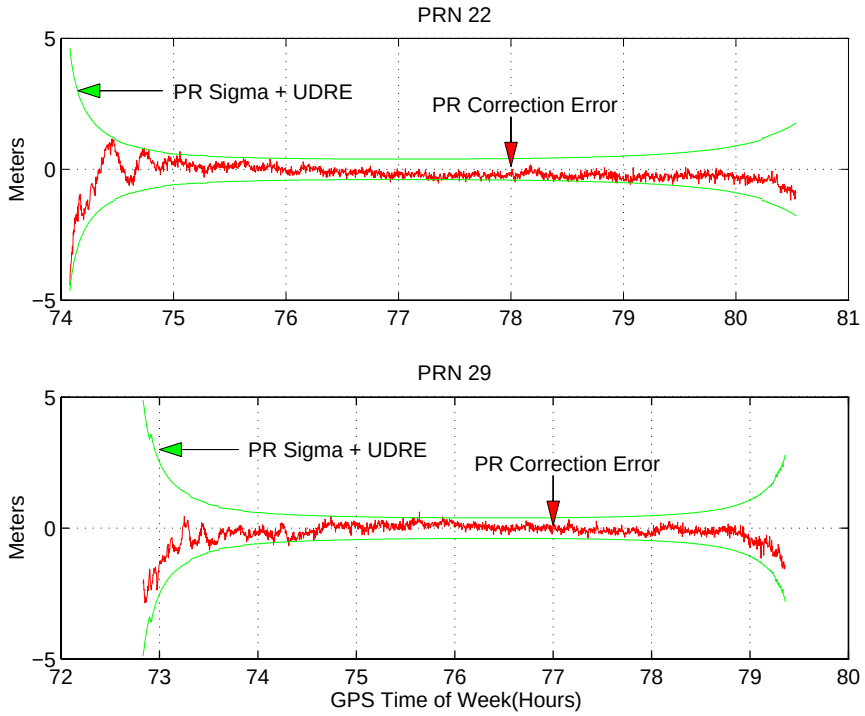

Figure 4.4: Pseudorange Correction Errors versus UDRE Estimates

Figure 4.4 plots the estimated UDRE and the pseudorange correction error for the reference station at Stanford (SU). The pseudorange correction error for satellite k is computed as follows:

$$e^k = \Delta\tilde{\rho}^k_{SU} - \Delta\hat{\mathbf{R}}^k \cdot \mathbf{1}^k_{SU} + \Delta\hat{B}^j$$

where $\Delta\tilde{\rho}^k_{SU}$ is the synchronized pseudorange residual for the k^{th} satellite observed by the Stanford reference station. Figure 4.4 shows the results of our UDRE estimator for satellites PRN 22 and PRN 29. As shown, the errors e^k are always within the combined UDRE and pseudorange sigma values.

4.4.3 Reasonability Check

A reasonability check is the final step before generated corrections are packed into WAAS messages. Reasonability checking uses the following specifications as guidelines:

1. GPS SPS Signal Specification on range domain accuracy [SPS]
    - 150 meters not to exceed (NTE) range error (eclipsed by WAAS MOPS, see SA offset below).
    - 2 meters/second NTE range error rate.
    - 19 millimeters/second^2 NTE range acceleration error.
2. WAAS MOPS Signal Specification [MOPS]
    - $-256.0 <$ SA offset < 255.875 (meters).
    - Ephemeris Error $< \pm 127.875$ (meters).
    - Ephemeris Error Rate $< \pm 0.0625$ (meters/sec).

If the generated corrections fail any of these tests, a "don't use" message will be broadcast for that satellite.

4.5 Satellite Clock Failure Simulation

The causes of satellite clock failures can be complicated. They could involve errors in the broadcast clock parameters (Subframe 1) or a real failure of the onboard atomic clock. The clock failure study presented here does not intend to include all possible failures. We choose cases which we think are the most common failure modes. The

effects, we consider, can be categorized into two simple types, namely step and ramp type failures. These two modes are the most common clock failures, and they will be used for our clock failure simulations. This section considers these two possible clock failures and examines how the clock algorithms described earlier handle them.

Satellite clock failures will not affect the results of CVTT and ephemeris error estimation. In both cases, we use a single differencing operation on the measurements from two reference stations (Section 2.3.2 and Section 3.1), and the satellite clock error term is canceled. However, it will affect the master clock estimate if it is observed by the master station.

The simulated clock errors, step-type or ramp-type, are added to the raw GPS measurements: pseudoranges, carrier phases and Doppler measurements (ramp-type error only). The ramp type error is discussed first.

A ramp-type clock error can be expressed as follows:

$$\Delta B^k(t) = \begin{cases} 0 & t < t_0 \\ \alpha\,(t - t_0) & t \geq t_0 \end{cases}$$

where α is the introduced slope error and t_0 is the time when this failure happens. $\Delta B^k(t)$ is added to the raw pseudoranges and carrier phases while α is added to the Doppler measurements.

Figure 4.5 shows the synchronized pseudorange residuals for PRN 30 of all the reference stations. Slope errors of 0.25 and 0.50 meters/second are introduced at GPS time 236600 seconds in two different simulations. Also shown is the WAAS bandwidth limit of 255.875 meters for the clock corrections (Reasonability check in Section 4.4.3). Darker lines indicate when PRN 30 is broadcast as "don't use" that occurs when the estimated clock correction exceeds 255.875 meters.

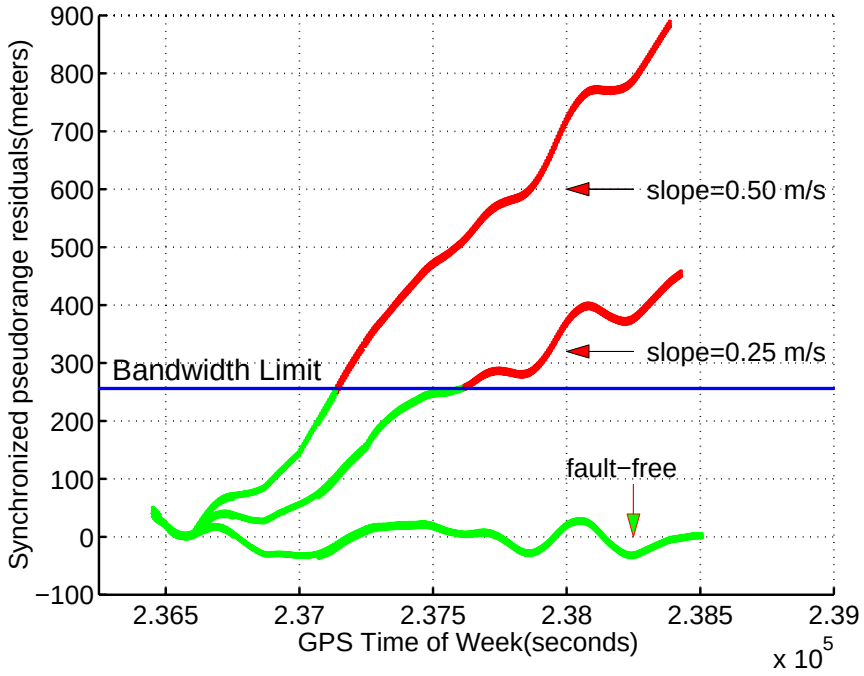

Figure 4.5: Ramp-Type Clock Failure Simulation

Here we plot the synchronized pseudorange residuals of all the TRSs for PRN 30. Ramp-type errors of size 0.25 and 0.5 meters per second are introduced to PRN 30 at time of week 236600 seconds. Bandwidth limit of 255.875 meters for the clock corrections is shown by the horizontal line. Darker lines are used when PRN 30 is broadcast as "don't use".

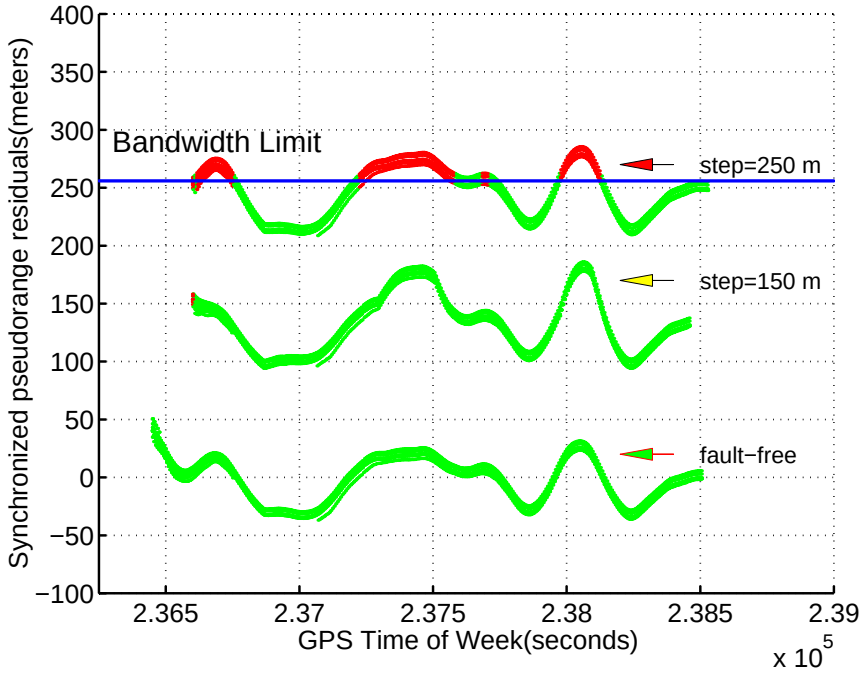

Figure 4.6: Step-Type Clock Failure Simulation

Synchronized Pseudorange Residuals for all the TRSs for PRN 30. Step-type errors of size 150 and 250 meters are introduced to PRN 30 at time 236600 seconds. Bandwidth limit of 255.875 meters for the clock corrections is shown by the horizontal line. Darker lines are used when PRN 30 is broadcast as "don't use".

As described earlier, this type of failures only effects the master clock filter. Our clock algorithm still generates estimates that fit with the measurements. The clock corrections for this satellite pass both chi-square and t tests, because this extra error is common to all reference stations. This failure can be identified in the master clock filter if its magnitude is large enough (because of SA's effect on the master clock filter). However, this failure is identified when its clock correction exceeds 255.875 meters (fails the reasonability check). Although we only show two cases of ramp type errors, this kind of failure can always be identified because the correction estimate will once again exceed 255.875 meters as the error introduced by the failure grows with time.

Similarly, a step-type clock error can be expressed as follows:

$$\Delta B^k(t) = \begin{cases} 0 & t < t_0 \\ A & t \geq t_0 \end{cases}$$

where A is the size of introduced step error and t_0 is the time when this failure is introduced. $\Delta B^k(t)$ is added to the pseudoranges and carrier phases.

Fig. 4.6 shows the synchronized pseudorange residuals for PRN 30 for all reference stations. Step errors of 125 and 250 meters are introduced at GPS time 236600 seconds in two different simulation tests. Also shown in the figure is the WAAS bandwidth limit (255.875 meters). Darker lines indicate when PRN 30 is broadcast as "don't use". When the step error first occurs, the clock error rate would be excessive. There would be an initial "don't use" and then be declared usable.

Once again, the introduced errors can be identified once the generated corrections fail the reasonability check. For a step error of 150 meters, the errors still can be corrected therefore the satellite is usable. There is no isolation since it is neither

necessary nor meaningful when the errors are correctable by our TMS.

For a step error of 250 meters, sometimes the errors cannot be corrected (fails the reasonability test) therefore it will be indicated as "don't use". It is important to note that the switching back and forth phenomenon between "use" and "don't use" in this figure. Our clock algorithm can promptly determine when the satellite is re-usable. This will guarantee that availability will not be unnecessarily sacrificed.

4.6 Summary

In this chapter, a snapshot weighted least-squares estimate is derived and its estimate is used as the input to a Kalman filter that provides a smoothed estimate for the clock error and the clock error rate. UDRE estimates are also derived and validated to provide a reliable weighting factor (UDREI) for user's navigation computation.

A reasonability check is implemented to check if the generated corrections are consistent with the GPS and WAAS signal specifications. Using simulated failures, we have demonstrated that the designed algorithms are capable of identifying when the troubled satellite should not be used (a "don't use" flag). When clock error or clock error rate cannot be corrected by the WAAS broadcast, a "don't use" flag will be broadcast promptly.

Chapter 5

Navigation Performance

To evaluate the real time WAAS concept and to test the algorithms being developed, Stanford's WADGPS Laboratory has participated in the FAA's National Satellite Test Bed (NSTB) as described in Chapter 2. As part of the on-going research co-operation with the FAA, Stanford has designed, built and flight tested a real-time WAAS prototype [Walter,a].

This chapter will describe WAAS performance for both static and dynamic platforms. Static users are chosen from one or many of the wide-area reference stations. When a station has been chosen as a static user, its data will not be used to generate the WAAS corrections. For dynamic evaluation, the results contain flight trial data collected in 1995 using Professor Powell's single-engine Piper Dakota.

Failures which include both real data with maneuvering satellites and simulations are tested to examine the performance of the WAAS prototype under failure states. This provides a way to evaluate the system in the presence of failures.

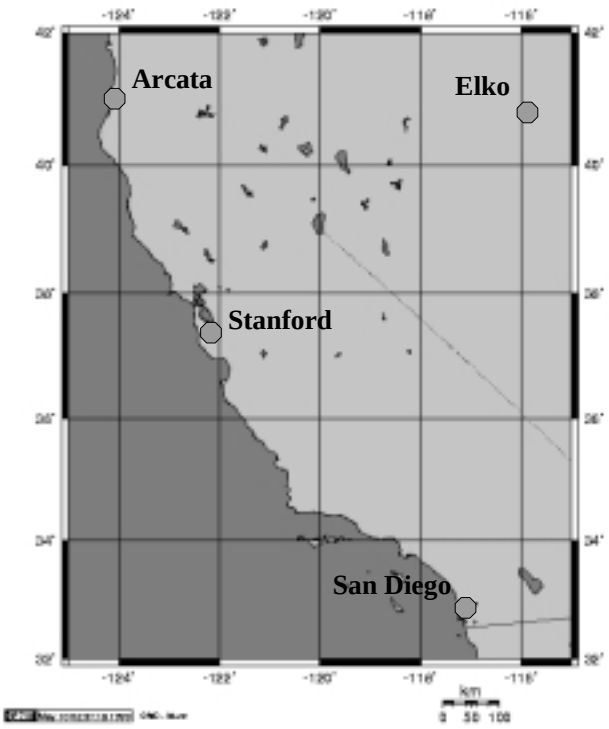

Figure 5.1: Stanford WAAS Test bed

5.1 Stanford WAAS Test bed

The results presented in this section were collected in real time using an early portion of the NSTB with the reference stations located in Arcata, California, Elko, Nevada and San Diego, California (Figure 5.1). These reference stations sent their GPS observations over the phone lines to the Testbed Master Station (TMS) on the Stanford campus. The vector differential corrections were derived from these observables. These corrections were then put into the RTCA data format and broadcast using a UHF transmitter. The results of static and dynamic tests are presented below.

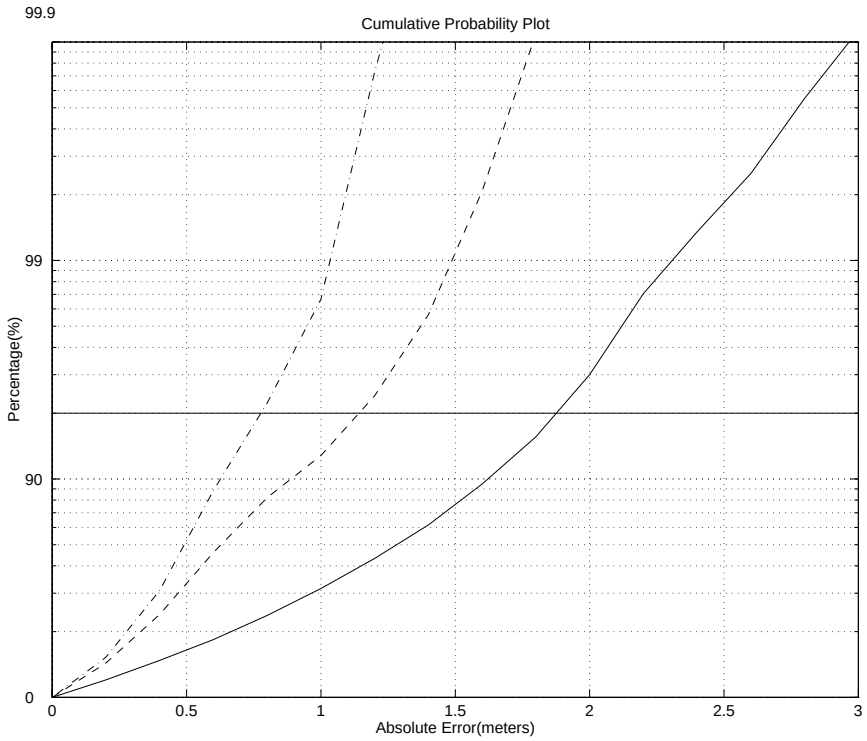

Figure 5.2: Cumulative Probability Plot of Absolute Errors

The results are plotted in the east-west (dashdot), south-north (dashed) and vertical (solid) directions. The solid horizontal line indicates the cumulative probability at 95%.

5.1.1 Static results

The statistics of the static test results are shown in Figure 5.2. This figure shows the distributions of the absolute errors in the east-west (dashdot line), south-north (dashed line) and vertical (solid line) directions. The inter-frequency biases (IFBs), which exist in both the reference station receivers and the GPS satellites, are calibrated [Chao,b]). IFB calibration is important for the ionospheric delay estimation and also affects the estimation of the ephemeris and clock error estimates. IFB calibration improves both the mean and the standard deviation of the navigation accuracy

[Chao,d].

This data was collected for about 32 hours and includes both daytime and nighttime at a 1 Hz epoch rate. Our accuracy is better than 1.5 meters in the horizontal directions 95% of the time. Positioning performance is better in the horizontal directions, but the 95% value for the absolute vertical error is also better than 2 meters.

These positioning results were based on our prototype WAAS algorithms. It will be helpful to compare these results with results from different algorithms, such as the dynamic orbit determination. In addition, we will also compare our results to algorithms that do not correct the ephemeris broadcast by GPS. In addition, we will assess the performance of a dual frequency receiver using our ground algorithms. These latter results will allow us to compare the relative importance of ionospheric estimation and ephemeris/clock estimation [Tsai,b].

Figure 5.3 shows the results from a 4-hour data set which we use to compare several situations. Once again, inter-frequency biases for the reference station receivers and the satellites have been calibrated for all cases. These four cases are:

1. **Broadcast** This result uses broadcast ephemeris only. In this case, the fast corrections are composed of weighted synchronized pseudorange residuals from our WRSs, while satellite ephemeris errors are set to be zero. This result is shown as a dashed line.

2. **WAAS Prototype** This result uses corrections generated by our prototype WMS. The corrections generated by our WMS were used to compensate satellite ephemeris errors, satellite clock errors and the ionospheric delays. The 250 bps data rate constraint is applied. The latency caused by data transmission from the reference stations to the WMS and by WMS data processing also exists. This result is shown as a solid line.

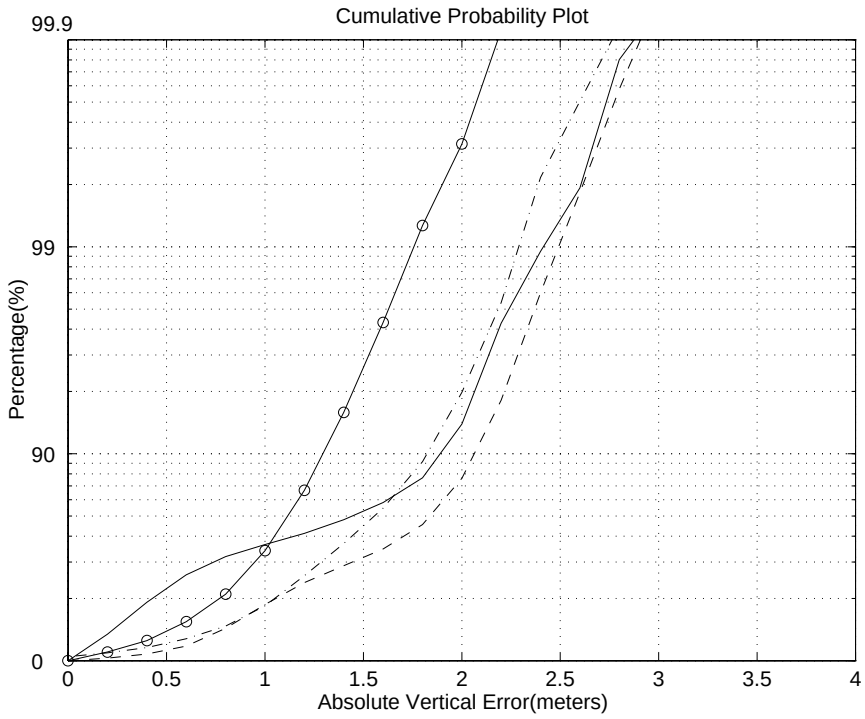

Figure 5.3: Cumulative Probability Plot of Absolute Vertical Errors

Results shown here include our prototype WAAS operation (solid), using broadcast ephemeris (dashed), using dual frequency receiver (solid line with "o") and results applying post-processed precise ephemeris (dashdot).

3. **Post-Processed Precise Ephemeris** This result uses post-processed precise ephemeris [IGS] from the International GPS Service For Geodynamics (IGS) for slow corrections (satellite ephemeris errors), and satellite clock corrections are derived from the synchronized pseudorange residuals using the post-processed precise ephemeris. The 250 bps data rate constraint is applied to the clock corrections but not to the ephemeris corrections. This result is shown as a dashdot line.

4. **Dual Frequency User** This result uses corrections generated by our WAAS prototype satellite ephemeris and clock estimator, but the user receiver employs measurements on both frequencies to estimate the ionospheric delay (Chapter 2). Corrections for the ionospheric delays from our prototype WAAS are not used. This indicates the accuracy a dual frequency WAAS user can achieve. The 250 bps data rate constraint is applied as well as the latency caused by data transmission from the reference stations to the WMS and by WMS data processing. The result is shown as a solid line with "o".

Our **WAAS Prototype** results show an improvement over using the **Broadcast** ephemeris, and is quite close to the results from using the **Post-Processed Precise Ephemeris**. This indicates our ephemeris and clock algorithms achieve nearly the same performance as the one which uses a more complicated dynamic model. However, given the limited amount of data points, the first three cases have indistinguishable results. In addition, the user is located almost at the center of our network which should have better results than users at the boundary.

The best result is achieved for a dual frequency user when the ionospheric delays can be calibrated using measurements on both frequencies. Ionospheric corrections from the WAAS broadcast are not used in this case. However, dual frequency receivers

are significantly more expensive and the second frequency is not approved for use by civil avionics.

5.1.2 Dynamic Tests

The flight trials were conducted at Palo Alto airport in 1995. As a truth source, we surveyed both ends of the runway of the airport using carrier phase differential GPS and assumed that the runway is flat. This model should be accurate to better than one meter.

The RTCA messages were broadcast to Professor Powell's Piper Dakota using a UHF data link. The airborne user had a 10 channel single frequency receiver to receive the GPS signals and a UHF radio modem to receive our WAAS messages. Eventually, the WAAS messages will be broadcast from geostationary satellites [Fuller]. The data presented here were collected "before" the inter-frequency biases were calibrated.

Figure 5.4 shows 20 *touch-and-go*'s conducted in a 90 minute period at the Palo Alto airport. These points include the flight technical error (FTE) in addition to the navigation system error (NSE). The flight technical error is the accuracy with which the aircraft is controlled relative to the indicated aircraft position The navigation system error is the difference between the indicated aircraft position and the true aircraft position. It is negligible when the aircraft is on the ground. Zero altitude is the surface of the runway. The vertical NSE when the airplane was on the runway (roughly from 50 meters to 450 meters in the along-track direction), are always within the ± 4.1 meters 95% (2drms) navigation sensor error limits (shown as dashed line) required for Category I precision approach and landing [FRP1992]. In addition, the vertical errors are very consistent for all approaches and have approximately the same offset [Tsai,b].

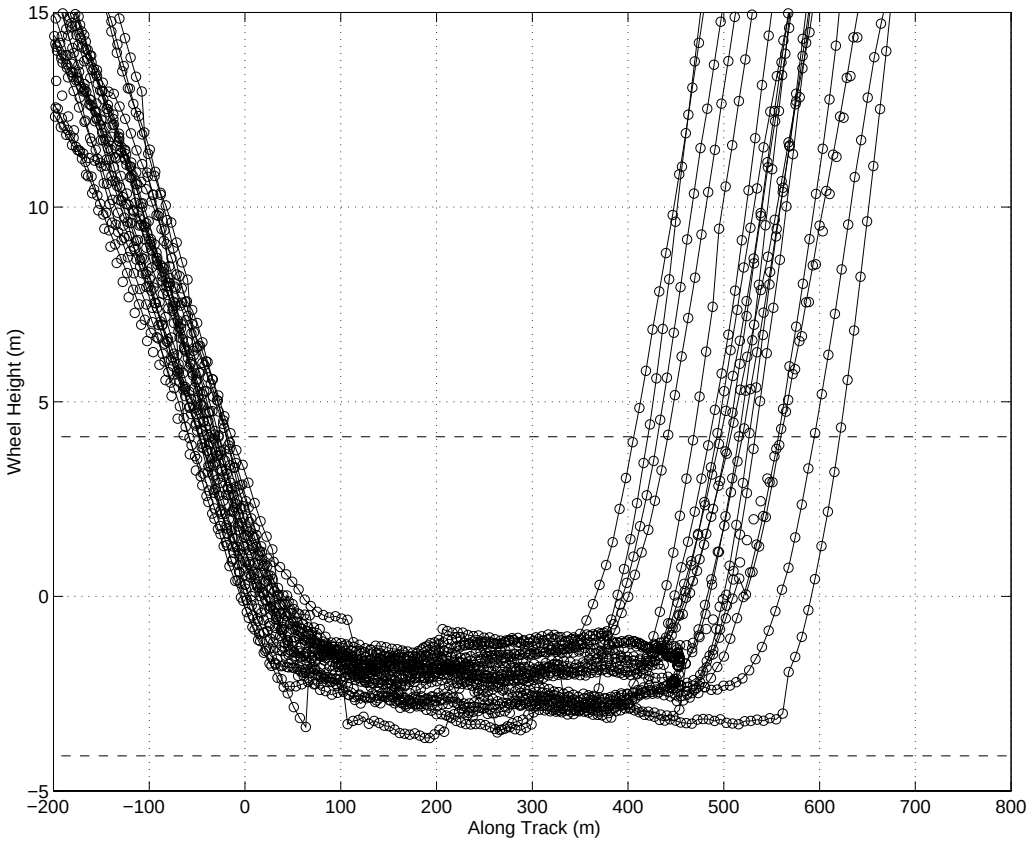

Figure 5.4: Results from Flight Trials at Palo Alto Airport

Dashed lines show the ±4.1 meters 95% navigation sensor error (NSE) required for the Category I precision approach and landing. 20 *touch-and-go*'s are conducted in a 90 minute period at the Palo Alto airport.

It is important to note that this flight trial was conducted before the IFB calibration. IFB calibration is important for the ionospheric delay estimation and also affects the derivation of synchronized pseudorange residuals and estimating ephemeris and clock corrections. IFB calibration can improve both the mean and the standard deviation of the navigation accuracy [Chao,b].

Interestingly, results from our static passive user show a mean vertical error of about -1.5 meters before IFB calibration. After we post-processed the data with the biases calibrated, the mean is about 0 meters. We believe the vertical errors on this flight trial are dominated by the inter-frequency biases and the errors should be centered around the zero altitude "after" IFB calibration.

There are a few jumps in Figure 5.4. We speculate that they are due to GPS signal multipath when the airplane was on the ground, and from message loss since the UHF data link performs poorly when the airplane is on the ground.

5.2 Integrity, Accuracy And Availability Under Fault-Free Conditions

The results presented in this section are the nominal system performance, i.e., no system component failures or degradations. The data (94917 epochs, about 26 hours) was collected on July 29, 1997 using the CONUS NSTB network as described in Chapter 2. The passive user is the receiver at the FAA Technical Center. The results will be presented in terms of *accuracy*, *integrity* and *availability*.

Accuracy The navigation system error (NSE) measures the degree of conformance between the estimated or measured position and/or velocity of a platform at a given

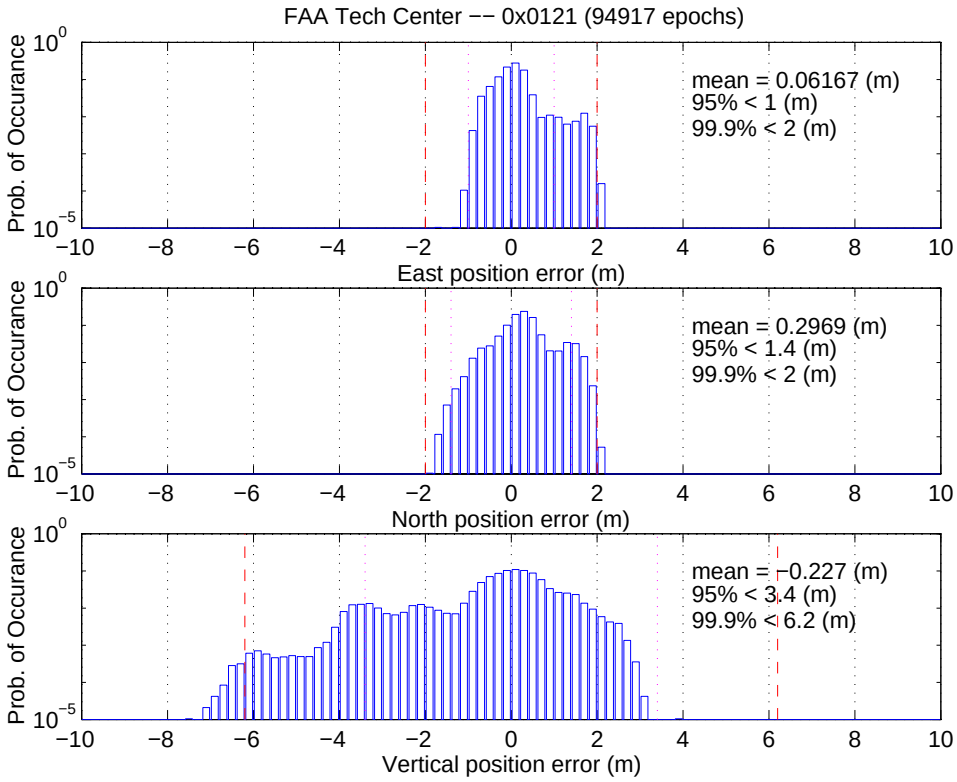

Figure 5.5: Accuracy Plot in the East, North and Vertical Directions.

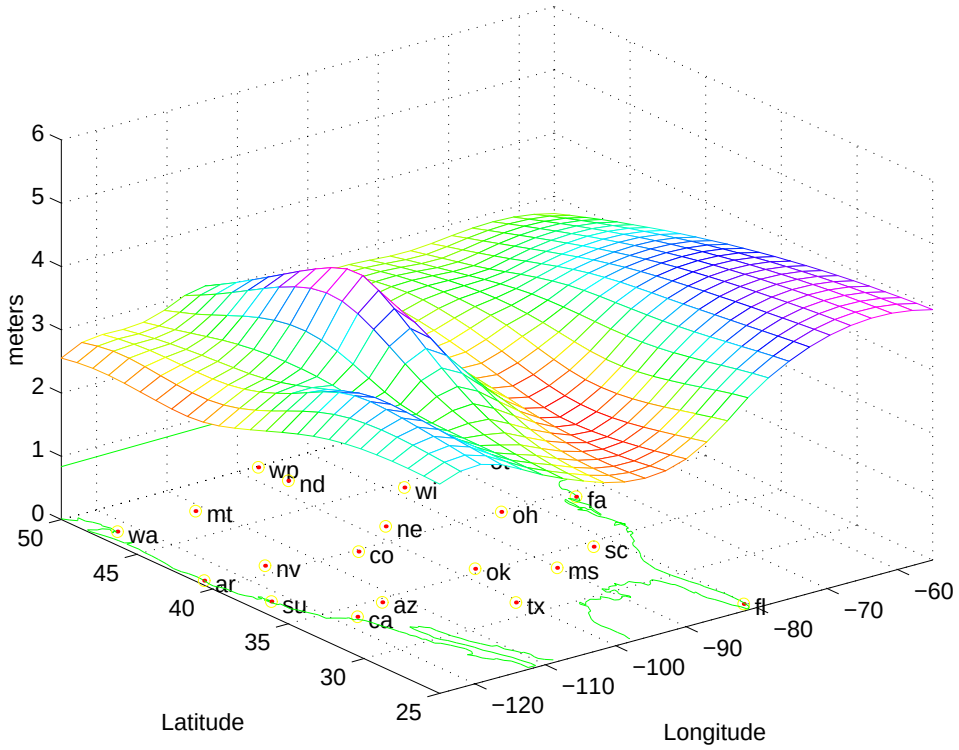

Figure 5.6: 3D Plot of the 95% Vertical Accuracy for the Entire NSTB Network

time and its true position and/or velocity. A histogram of this difference is shown in Figure 5.5. The horizontal errors are better than 1.5 meters 95% of the time. The vertical accuracy is 3.4 meters (95%) which is better than the 4.1 meter Category I precision approach requirement for the NSE [FRP1992].

Figure 5.6 is a three dimensional plot of the 95% vertical accuracy for the entire NSTB network which includes both active reference stations and passive users. Overall, the vertical performance of the NSTB achieved the required accuracy for WAAS.

Integrity is the ability of a navigation system to provide timely warnings to users when the system should not be used for navigation purpose. Estimated sigma values

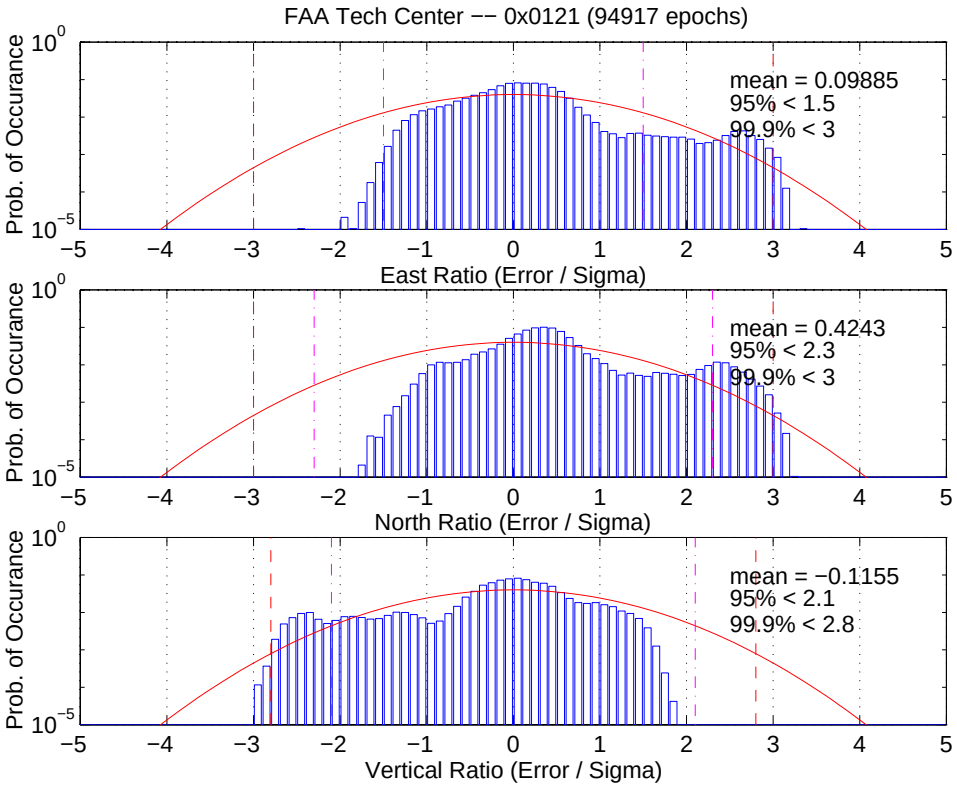

Figure 5.7: Integrity Plot.

(computed from the covariance matrix of WLS estimates in Chapter 2) should be able to cover the real position errors. Integrity is evaluated as the ratio of position error to the estimated sigma. Figure 5.7 shows the histogram of the actual-to-predicted error ratio. Integrity is maintained as long as the tails of the histogram are bounded by the unit Gaussian curve (shown as the solid curve). In all three dimensions, the integrity is preserved.

Availability is the probability that the navigation and fault detection functions are operational and that the signal accuracy, integrity, and continuity of function requirements are met. Availability is measured using the the one sigma error bound for the position estimate. For a navigation sensor error bound of 19.2 meters at a

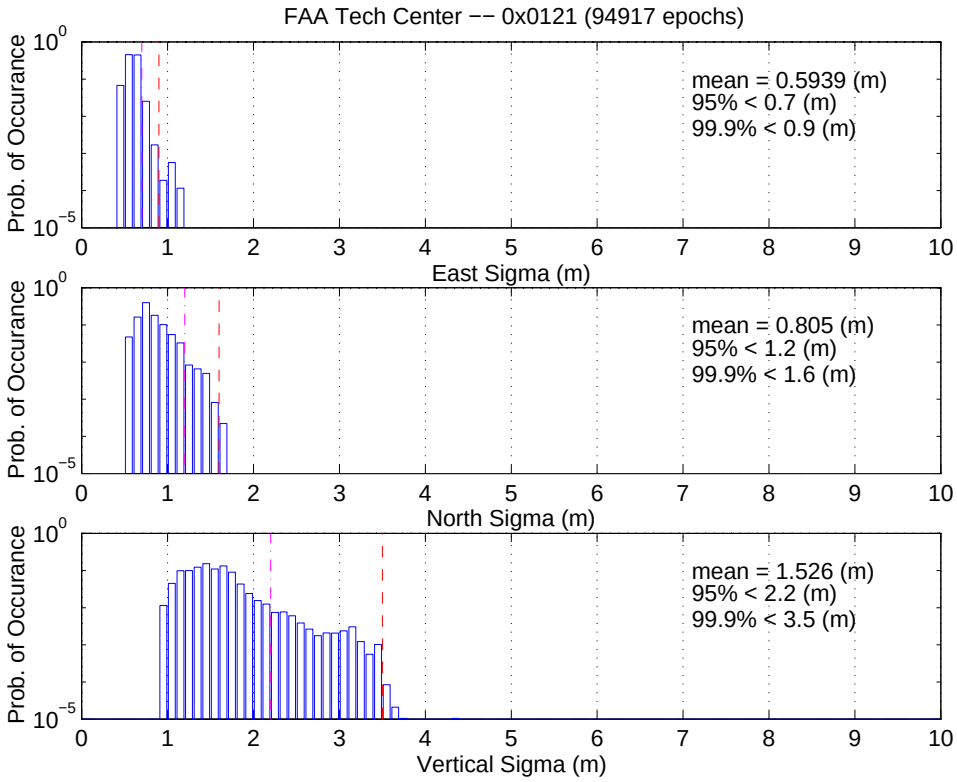

Figure 5.8: Availability Plot

probability level better than 10^{-7} the maximum allowable bound is 3.6 meters. If sigma is larger than this value then the system will be declared "unavailable" at that instant. Figure 5.8 shows the WAAS predicted one sigma error bound. The WAAS system is available more than 99.9% for the duration of the data set.

Figure 5.9 shows the "accuracy" comparison between a dual frequency user and a single frequency user. Results for the single frequency user are shown by the lighter lines and its statistics are on the right hand side of the plots while those for the dual frequency user are shown by the darker lines and its statistics are on the left hand side of the plots.

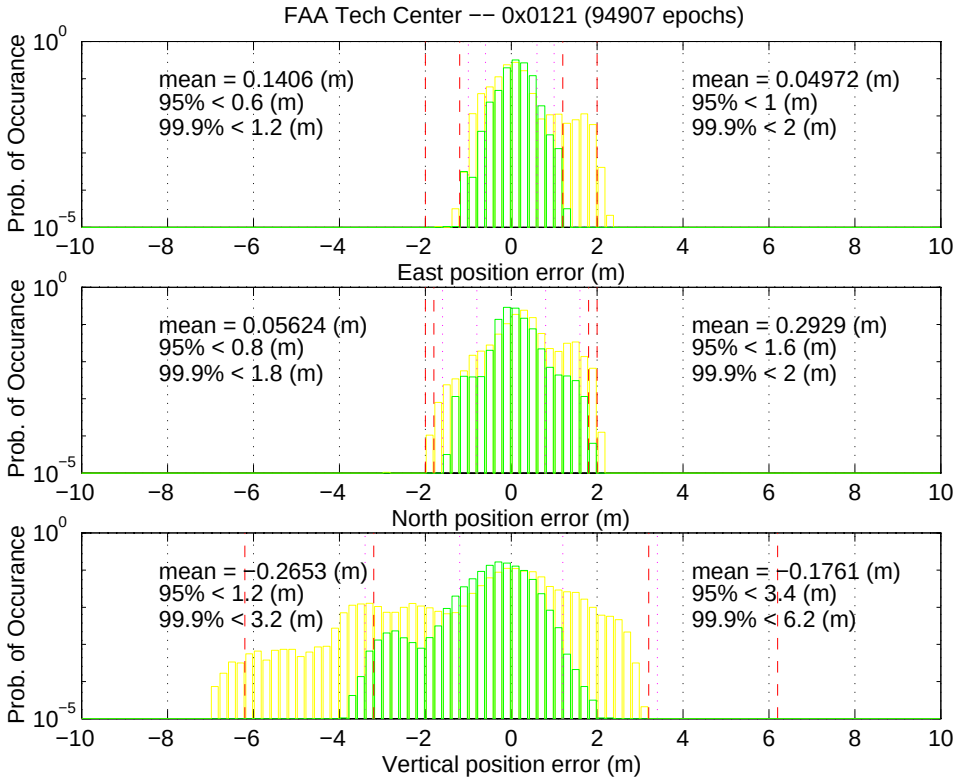

Figure 5.9: Accuracy Comparisons Between Single and Dual Frequency Users

Numbers shown on the right are the results (lighter lines) for the single frequency user. Numbers shown on the left are the results (darker lines) for the dual frequency user.

	East (m)	North (m)	Vertical (m)
Single-Frequency	1.0	1.6	3.4
Dual-Frequency	0.6	0.8	1.2

Table 5.1: 95% Accuracy Comparisons between Single- and Dual- Frequency Users

With dual frequency ionospheric measurements in the user equipment, the histograms in Figure 5.9 show smaller errors in all three dimensions. The 95% vertical accuracy improves from about 3.4 meters to 1.2 meters. Table 5.1 summarizes the results of Figure 5.9 and compares the accuracy for the single- and dual- frequency users. This result indicates the problem in estimating the ionospheric corrections using a vertical grid model which makes no use of the physical ionosphere model [Hansen,b] [WG2].

5.3 Faulted Performance

Integrity monitoring is one of the most important tasks of the WAAS. The WAAS signal broadcast not only has to improve the positioning accuracy but to provide integrity information within a specified time-to-alarm. To be used as a primary-means navigation sensor, the WAAS is required to provide safety critical warning signals when the system should not be used. This capability relies on the master station's ability to detect and isolate failures which could effect the differential correction generation.

Malfunctions in the WAAS system can come from both the WAAS ground segment and the GPS space segment. Possible causes of failures can be rather complicated. Here we investigated several failure modes which we think are important and would be catastrophic if not properly handled. Failures of the user's receiver are not included in this study.

5.3.1 Reference Clock Degradations

Reference station clock degradations or failures have a direct impact on the system. For example, if the rubidium clock fails, the receiver might have to use its internal crystal clock. Data from this station will be excluded during the CVTT filter process because a crystal clock is noticeably less stable over time than a rubidium clock.

Reference clock failures can occur at either the master station or the reference station. Slow ramp-type error may be the most difficult to detect and identify. Accordingly, failure modes investigated here include both ramp-type and step-type failures.

Each WAAS reference station will have multiple dual frequency receivers for redundancy. Reference receiver failures other than clock are not considered here. Only reference clock failures are simulated and studied. Other types of failures within an individual receiver, such as multipath and cycle slips, will not be addressed here.

5.3.2 GPS Space Segment Degradations

The Operational Control Segment (OCS) does an excellent job of estimating satellite orbit and clock and in maintaining the integrity of the GPS navigation message broadcast [Bower] [Crum] [McCaskill]. Even so, failures on the space segment can still occur. The required time for the OCS to upload a new ephemeris or clock message to flag a troubled satellite as "unhealthy" could take tens of minutes. This precludes

the use of unaugmented GPS for non-precision and precision approach phases of flight. WAAS adds an additional layer of protection to provide more timely warnings to the airborne users.

Space segment failures could result either from real satellite ephemeris anomalies or errors in the OCS uploaded satellite ephemeris/clock parameters (Subframe 1, 2 and 3). In either case, broadcast parameters fail to provide correct data for the users to compute satellite position and satellite clock bias.

When the broadcast ephemeris parameters contained in the subframes 2 and 3 fail to provide accurate satellite position computation, we call this an ephemeris failure. Similarly, broadcast clock errors could result from inaccuracies in the broadcast parameters or physical failures of the atomic clock on board. The effects are categorized into two types, namely the ramp-type and step-type failures. Slow ramp errors could go undetected by the OCS for a long enough period that they would pose integrity threats to the users.

The failure modes described above have been studied in the previous chapters. Their influence on the end-to-end required navigation performance (RNP) will be presented next.

5.3.3 Faulted Performance Results

To verify the individual fault detection and isolation algorithms and to demonstrate the end-to-end integrity of our master station algorithms, I added simulated failures to real NSTB data. Also included in this data was an actual satellite maneuver. This data was then reprocessed by our master station algorithms as though they had been received in real time.

Results presented here again employ real data collected on July 29, 1997. According to the OCS ephemeris broadcast, space vehicle PRN 7 was set "unhealthy" from GPS time of week 297060 to 319790 seconds. Its data, however, is included in our WMS data processing.

The following "artificial" failures were added to the WAAS ground segment and GPS space segment:

1. From 241200 to 248400 seconds, a ramp-type clock degradation with an error rate = 0.50 m/s was added to each TRS measurement from PRN 17.

2. From 248400 to 255600 seconds, a ramp-type clock degradation with an error rate = 0.50 m/s was added to each TRS measurement from PRN 21.

3. From 277200 to 284400 seconds, a step-type clock degradation of size 250 meters was added to each TRS measurement from PRN 3.

4. From 302400 seconds till the end of data, a step-type error degradation of size 150 meters was added to all satellite measurements from the Miami station.

5. From 324000 seconds till the end of data, a ramp-type error degradation of slope 0.50 m/s was added to the all satellite measurements from Stanford station (master clock).

Figure 5.10 shows the time when each failure is present. As shown, many failures exist in this evaluation and at some times there are multiple failures [Tsai,c].

Figure 5.11 compares the vertical results for the fault-free and faulted performance of the passive user at the FAA Technical Center. The faulted performance results include fault detection and removal of both simulated failures and satellite maneuvering using our algorithms as described in the previous chapters. Results for the fault-free

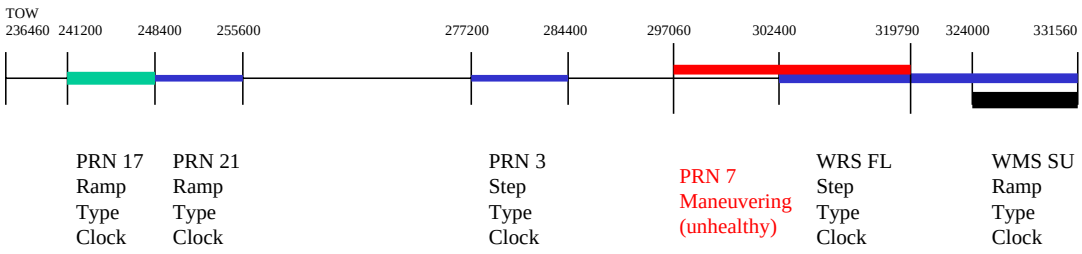

Figure 5.10: Time and Periods When Failures Are Introduced

There are 5 artificial degradations, or failures, introduced to the real data. This data also contains a maneuvering satellite on PRN 7.

mode are shown by the darker lines and the corresponding statistics are displayed on the right hand side of the plots while those for the faulted mode are shown by the lighter lines and their statistics are displayed on the left hand side of the plots.

The accuracy performance is shown in the bottom plot. The faulted results does contain one point that has positioning accuracy worse than -10 meters. However, the 95% or 99.9% performance for the two results are nearly the same.

The integrity performance is shown in the top plot of Figure 5.11. Once again, the 95% or 99.9% vertical performance for these two results are nearly the same. Note that integrity is preserved even though there was an outlier in the accuracy. In other words, these algorithms were able to predict the outlying position estimate.

The middle plot of Figure 5.11 is the availability performance. The faulted results have a few more outliers than do the fault-free results. These outliers arise in the early stage of failure introduction when the outlying measurements are detected but not yet isolated. During that period of time, the estimated UDRE's are increased and availability is reduced to preserve integrity. Once again, the 95% or 99.9% performance for these two results are nearly the same. We have to sacrifice some availability for integrity. Notice, however, despite the unusually large number of failures, the availability penalty is slight.

The 99.9% vertical performance comparisons between fault-free and faulted results are summarized in Table 5.2. These two scenarios result in nearly the same accuracy, availability and integrity. The outlying measurements were isolated and did not cause any integrity failures. Fault detection and isolation algorithms did not cause a significant loss of availability.

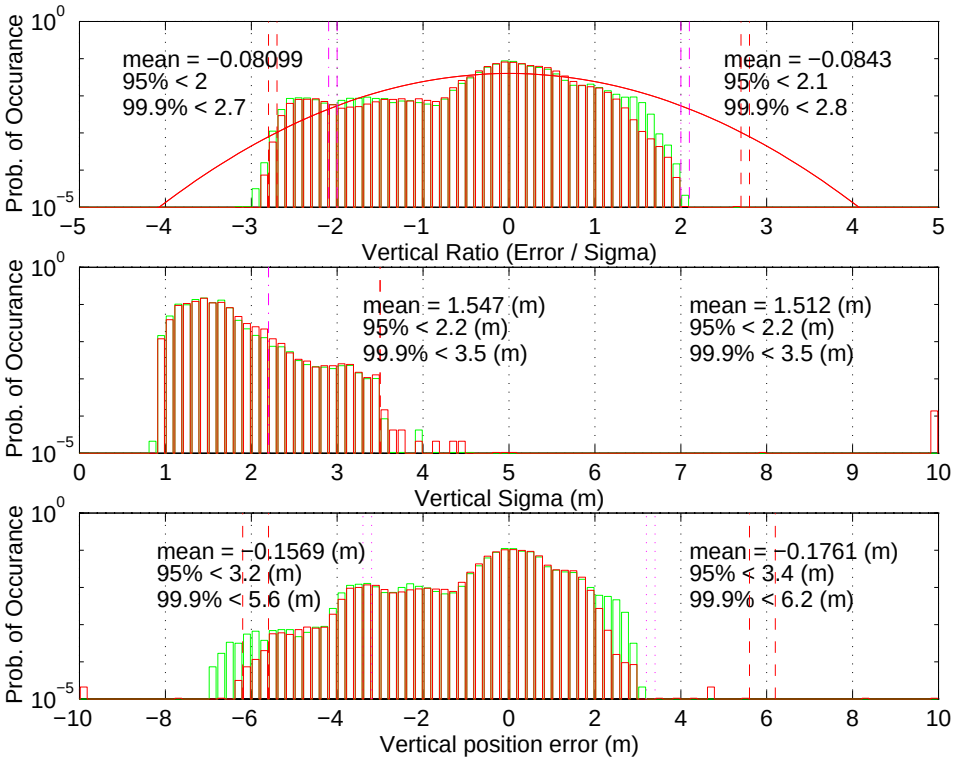

Figure 5.11: Vertical Performance Comparisons: Fault-free versus Fault-state

The passive user is located at the FAA Technical Center. There are approximately 94,000 data points used. Shown here are the "vertical" performance comparisons in integrity (top), availability (middle) and accuracy (bottom). Numbers shown on the right are the results (lighter lines) for fault-free state. Numbers shown on the left are the results (darker lines) for faulted state.

Station Name	Accuracy (m)	Availability (Sigma (m))	Integrity (Accuracy/Sigma)
Arcata	6.20 vs 6.20	5.40 vs 5.60	2.00 vs 2.10
Stanford	6.40 vs 6.00	6.00 vs 6.00	2.20 vs 2.70
FAA Tech. Center	6.20 vs 5.60	3.50 vs 3.50	2.80 vs 2.70

Table 5.2: 99.9% Vertical Performance Comparisons: Fault-free versus Fault-state

Fault-free versus fault-state results are shown. The stations at Arcata, Stanford, and the FAA Technical Center, are chosen as passive users. There are approximately 94,000 data points used.

5.4 Summary

In this chapter, we first presented accuracy for both static users and dynamic users derived from data collected from our earlier Stanford WAAS test bed. The achieved accuracy met the Category I precision requirements. We also compared the performance using corrections generated by our algorithms with corrections generated by the IGS precise ephemeris and with corrections using broadcast ephemeris only. Approximately the same level of accuracy was obtained in all three cases.

Using data from the FAA's NSTB, we have examined the system performance in terms of accuracy, integrity and availability. In addition, we have presented a comparison of performance results for single and dual frequency users.

Integrity monitoring algorithms were also tested against a real GPS failure (a

maneuvering satellite) as well as simulated failures. Simulated failures include satellite clock errors of ramp and step types, and reference station clock errors of ramp and step types. Importantly, our algorithms reliably determine "use" and "don't use" flag for all satellites independent of the OCS broadcast of "healthy" and "unhealthy" for our simulated failures and maneuvering satellites.

We have evaluated and compared the performance of our algorithms under fault-free and fault-state conditions. Our algorithms provide nearly the same level of accuracy, availability and integrity (Table 5.2) even in the presence of faults.

Chapter 6

Conclusions

WAAS progresses steadily towards a primary-means navigation service. The research work done at the Stanford WADGPS Laboratory has continuously demonstrated that the stringent requirements for precision approach can be met. With WAAS, more than one thousand airfields in the continental United States (CONUS) will have immediate access to a precision approach capability. Because of its wide coverage and cost-effectiveness, WAAS has attracted several other countries to participate. Two systems similar to WAAS are being developed and tested. One is the European Geostationary Navigation Overlay System (EGNOS) and the other is the Japanese MTSAT based Satellite Augmentation System (MSAS). Eventually, these satellite based augmentation systems (SBASs) will work together to provide seamless navigation service all over the world.

6.1 Ephemeris and Clock Error Estimation

A simple kinematic model for the ephemeris errors achieves user navigation performance nearly equivalent to that using a far more complicated dynamic model to

estimate the ephemeris errors. In addition, our approach decouples the pseudorange residuals from satellite to satellite. Therefore, only a small filter is required for each satellite. In addition, this greatly simplifies error tracing analysis.

6.2 Integrity Monitoring

Integrity monitoring is a vital WAAS task. Failures in the OCS broadcast ephemeris and clock parameters must be detected and isolated. The proposed approach is an integrated method which combines estimation and hypothesis testing. Without introducing too much computational complexity, ramp and step failures in the WAAS system were detected and isolated before they corrupted filter estimates. The approach has shown the capability to detect WAAS component failures, whether they occur in the ground segment or the space segment. Furthermore, the decision on "use" and "don't use" does not need to rely on the GPS broadcast of "healthy" and "unhealthy."

6.3 Summary of Accomplishments

The following is a summary of my contributions:

Ephemeris and Clock Error Estimation and Separation I designed an algorithm to separate and estimate the ephemeris and clock error components. The generated corrections are capable of providing the required accuracy for the users.

The algorithm also separates the ephemeris errors from the clock errors so they can be incorporated into the slow and fast messages respectively. The slowly varying ephemeris errors will not have to be broadcast as frequently as the fast clock errors.

This makes efficient use of the limited WAAS data broadcast bandwidth.

Demonstration of Category I Accuracy We have shown that Category I precision approach accuracy requirement can be met with our WAAS prototype. The conclusion is drawn from both static tests and dynamic flight trials.

UDRE Estimation and Verification I developed an algorithm to estimate UDRE and to verify the estimate which guarantees the confidence estimates providing integrity and weights for the weighted least-squares position estimates. This accomplishment is more important than generating the corrections themselves since all users will use these confidence estimates in their weighted least-squares navigation solution and to estimate the quality of the current WAAS service.

Investigate WAAS Performance Under Failure Modes Several layers of protection are necessary to guard against all possible system degradations, also known as failures. I have described and demonstrated how different kinds of failures can be detected and isolated with our master station algorithms.

In addition, I also implemented the following improvements to our master station data processing:

- A fast measurement downdating algorithm which reduces computational complexity while performing integrity monitoring. This algorithm is described in Appendix C.

- For the master clock filter, I implemented a Kalman filter to prevent discontinuities in the master clock estimate. This effort was important because each jump in the master clock introduces a discontinuity in the synchronized pseudorange

residuals. The effect is a discontinuity on the satellite clock error estimates and satellite(s) might be flagged as "don't use" temporarily if this discontinuity fails the reasonability check (Chapter 4).

- I devised a least-squares algorithm to reliably detect cycle slips. This algorithm is a more robust approach than our previous cycle slip detection method that used Doppler measurements.

- For the common view time transfer (CVTT) filter, I added several new features to switch the master clock in the event of a detected master clock failure. The switch is executed if the clock error estimate fails to pass chi-square test for more than 60 seconds or if the estimate for clock error rate exceeds 1.5 meters per second.

6.4 Recommendations for Future Work

Before WAAS is ready to provide seamless navigation guidance, much work still needs to be done. Here are some thoughts for this future research.

Interoperability of WAAS Two systems similar to WAAS are being developed and tested. One is the European Geostationary Navigation Overlay System (EGNOS) and the other is the Japanese MTSAT based Satellite Augmentation System (MSAS). Australia also has established its test bed.

All satellite based augmentation systems under development around the world should operate together to provide a seamless global navigation service. To achieve this goal, all augmentation systems need to be interoperable, thus eliminating technical, operational and procedural differences that an aircraft would otherwise encounter

while flying internationally between systems. Interoperability includes an array of procedures, standards, functional specifications and technical performance that must be addressed and satisfied so that one system works flawlessly with the others.

Redundant Navigation Systems A satellite based navigation system (SBAS) must remain available even during temporary GPS outages due to interference, jamming or even satellite failures. SBAS is susceptible to the threat from jamming and vulnerable to signal interference. Although the WAAS reference stations and master stations are resistant to jamming, it is still necessary for a redundant service in case the WAAS fails to provide guidance information. Therefore, integration with other external aids will be important as well as necessary. Existing DME systems, ILS facilities, or the Loran-C system, could be used. However, more research is necessary.

GPS modernization plan and additional second and third civil frequencies will definitely impact existing navigation systems. These also require further research.

6.5 Closing Remark

Global navigation satellite systems will be the primary-means aircraft navigation system. WAAS promises to provide seamless aircraft navigation guidance throughout the en-route, terminal, non-precision and precision approach phases of flight. Before WAAS becomes a sole-means navigation guidance system, its performance in terms of accuracy, integrity and availability, must be understood and enhanced. The research presented in this dissertation has made several key contributions toward this goal.

Appendix A

Chi-square Test

The chi-square test is a well established statistical approach to check the "goodness of fit" between the measurements and the estimate [Neter]. Given the M x 1 measurement vector $\mathbf{z}$ which are related to state vector $\mathbf{x}$ of dimension N x 1 by the following equation

$$\mathbf{z} = \mathbf{H} \cdot \mathbf{x} + \mathbf{v}; \tag{A.1}$$

where $\mathbf{v}$ is the measurement noise vector with the covariance matrix $\mathbf{R}$. Assume $\hat{\mathbf{x}}$ is the estimate for Equation (A.1) and its error covariance matrix is $\hat{\mathbf{P}}$. $\mathbf{z}$, $\mathbf{R}$, and $\hat{\mathbf{x}}$ will be used as the basic inputs for failure detection using the chi-square test. The chi-square is computed as follows:

$$\chi^2 = \sum_{i=1}^{i=M} \frac{(z_i - \mathbf{H}_i \hat{\mathbf{x}})^2}{\sigma_i^2} \tag{A.2}$$

where $\mathbf{H}_i$ is the i^{th} row for matrix $\mathbf{H}$ and σ_i^2 (R_{ii}) is the variance for the i^{th} measurement.

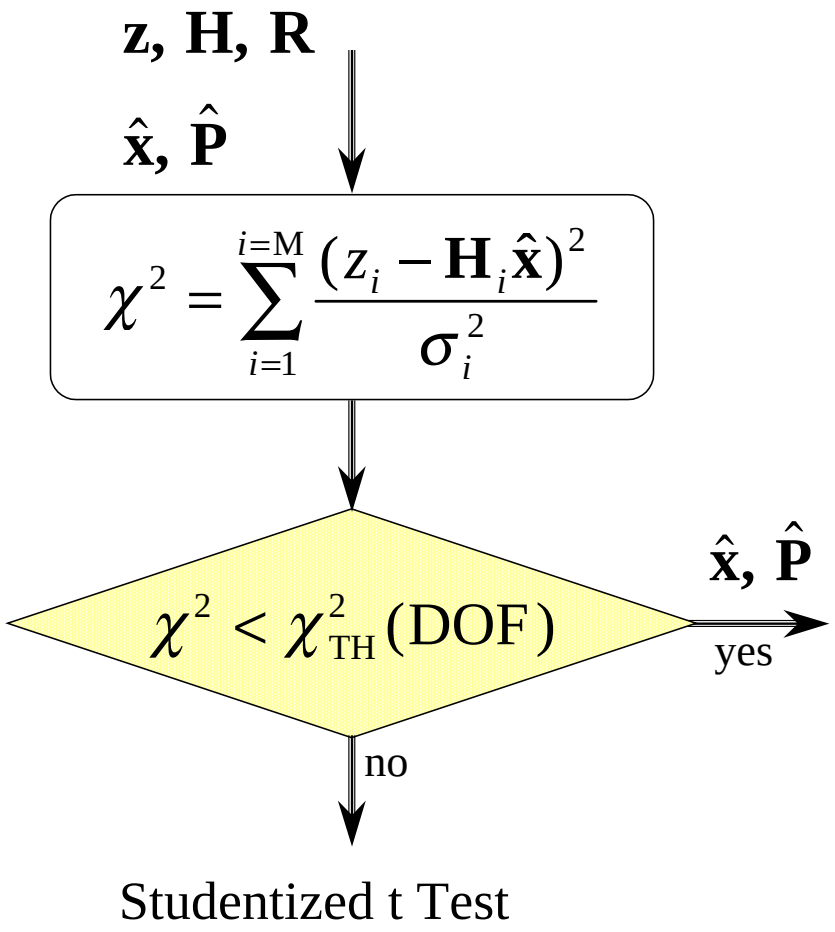

Figure A.1: Chi-square Test for Outlier Detection

DOF is the number of degrees of freedom which is equal to $M - N$. A Studentized t test will be executed if the chi-square test is failed.

χ^2 computes the sum of squares of the residuals weighted by the measurement variance σ_i^2 and follows a standard chi-square distribution with the number of degrees of freedom equal to $M - N$ [Neter]. By choosing a proper probability of false alarm (P_{FA}), the detection threshold can be set. A small value of χ^2 does not necessarily indicate a better fit. A value of χ^2 that is very small may indicate an error in the assignment of the uncertainties in the measured variables [Bevington]. This computed chi-square χ^2 is the weighted sum of squared errors (WSSE) [Walter,b].

If the measurements do not contain any outlier, χ^2 should always be smaller than the detection threshold. To examine if the estimate $\hat{\mathbf{x}}$ is valid, the following simple hypothesis is used:

$$\begin{cases} H_0: & \hat{\mathbf{x}} \text{ using all measurements is a good one.} \\ H_1: & \text{one or more measurements are corrupted.} \end{cases}$$

The decision on whether an outlying measurement is present is based on the following criterion:

$$\begin{cases} \text{Accept } H_0, \text{if } \chi^2 \leq \chi^2_{\text{THRESHOLD}}(\nu) \\ \text{Accept } H_1, \text{if } \chi^2 > \chi^2_{\text{THRESHOLD}}(\nu) \end{cases}$$

where ν is degrees of freedom of chi-square. If hypothesis H_1 is accepted, it means outlying measurement(s) might be present.

The block diagram of the chi-square test is shown in Figure A.1. An example of outlier detection using the chi-square test is shown in Figure A.2. If the chi-square test issues an alarm, the effort to identify the outlier(s) will be followed using a Studentized t test. Outlier isolation using a Studentized t test is described in Appendix B.

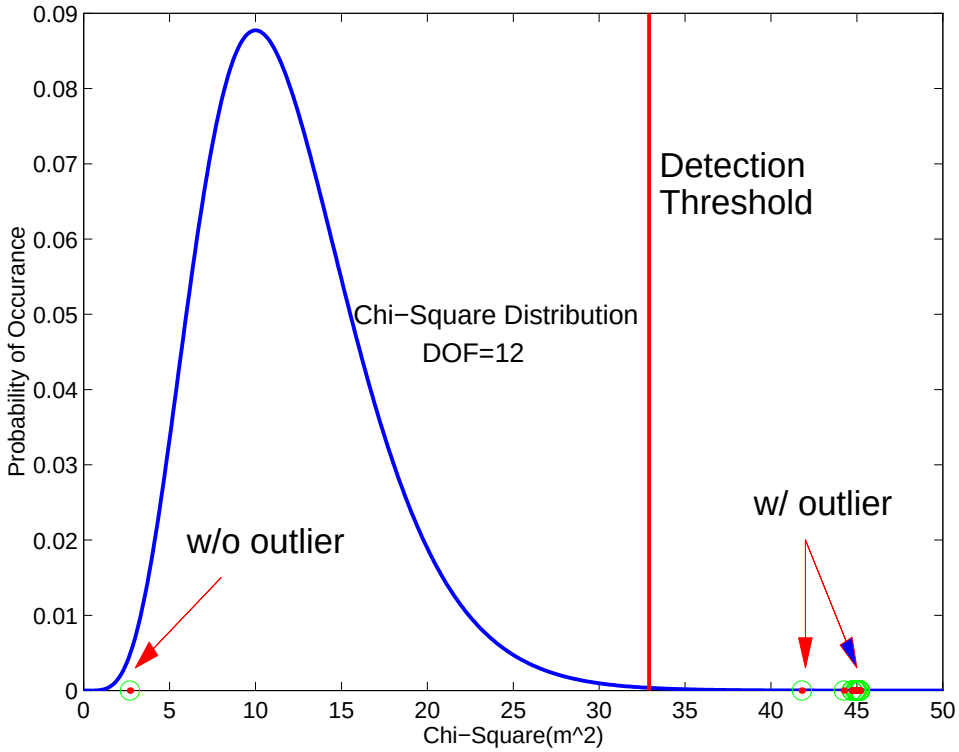

Figure A.2: An Example of Outlier Detection Using a Chi-square Test

The detection threshold is plotted as a vertical line for a chi-square distribution with the number of degrees of freedom equal to 12. The estimate which uses no outliers will have a small χ^2 while χ^2 for estimates derived using measurements that contain the outlier(s) might exceed the detection threshold.

Appendix B

Studentized t Test

Outlier isolation requires computing the new estimates of the unknown state vector $\mathbf{x}$ using only a subset of the measurements. When the number of measurements is large, the computational load increases dramatically. I derived a general formula for measurement downdate which computes the new estimate and its covariance matrix using $\hat{\mathbf{x}}$, $\hat{\mathbf{P}}$ and deleted measurement(s) and its noise covariance matrix. Measurement downdate obviates the need to compute the new estimate from scratch and greatly improves efficiency. The general formula for measurement downdating is detailed in Appendix C.

The procedure for outlier isolation is as follows:

1. Compute the new estimates $\hat{\mathbf{x}}_{(k)}$ and $\hat{\mathbf{P}}_{(k)}$ when removing the k^{th} measurement.

2. Compute the chi-square for each of these

$$\chi^2_{(k)} = \sum_{i=1, i\neq k}^{i=M} \frac{(z_i - \mathbf{H}_i \hat{\mathbf{x}}_{(k)})^2}{\sigma_j^2}$$

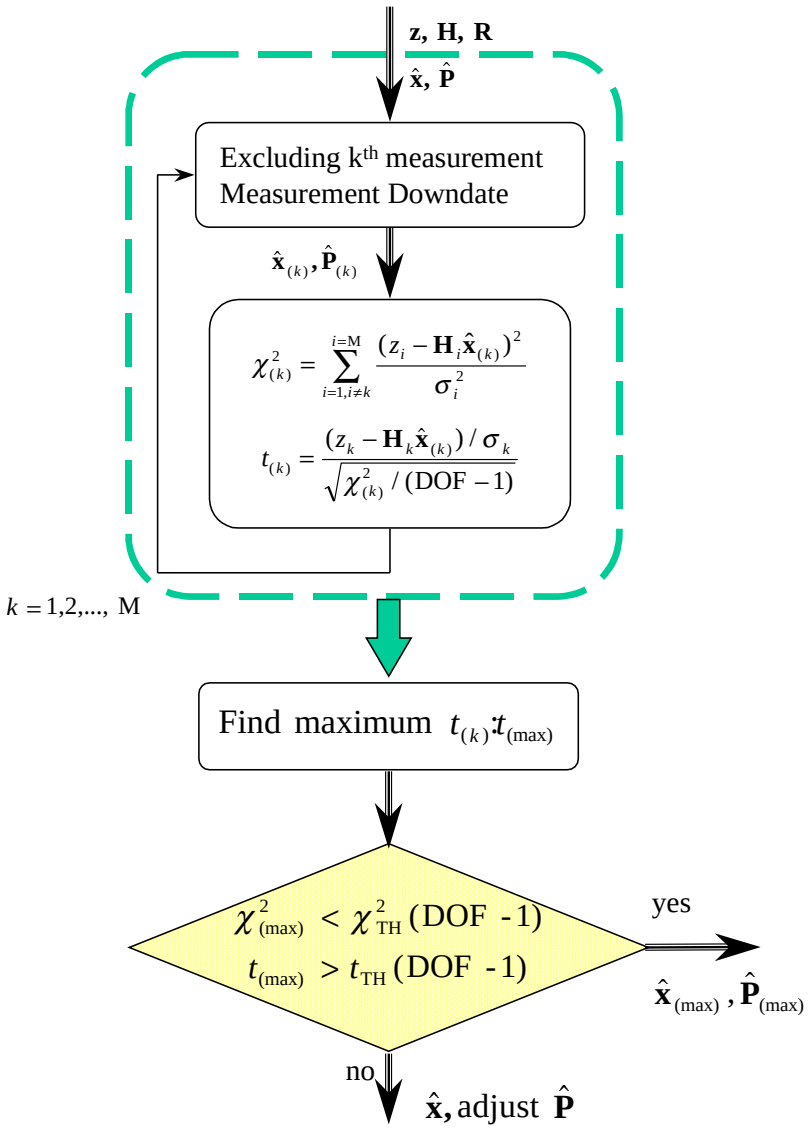

Figure B.1: Studentized t Test for Outlier Detection

DOF is equal to $M - N$. The number of degrees of freedom for both $\chi^2_{(k)}$ and $t_{(k)}$ is $M - N - 1$. Covariance matrix $\hat{\mathbf{P}}$ will be adjusted if no outlier(s) can be identified.

3. Compute the "t" distribution

$$t_{(k)} = \frac{(z_k - \mathbf{H}_k \cdot \hat{\mathbf{x}}_{(k)})}{\sigma_k} / \sqrt{\chi^2_{(k)}/(M-N-1)}$$

$M - N - 1$ is the number of degrees of freedom for $t_{(k)}$. $t_{(k)}$ will be large if the k^{th} measurement does not agree with the estimate based on all but the k^{th} measurement.

4. Outlier is identified if the following two conditions

$$\begin{cases} \chi^2_{(k)} < \chi^2_{\text{THRESHOLD}}(M-N-1) \\ t_{(k)} > t_{\text{THRESHOLD}}(M-N-1) \end{cases}$$

are both met. $\hat{\mathbf{x}}$ and $\hat{\mathbf{P}}$ will be replaced by $\hat{\mathbf{x}}_{(k)}$ and $\hat{\mathbf{P}}_{(k)}$

The block diagram for the Studentized t test is shown in Figure B. If none of $t_{(k)}$, $k = 1, 2, ..., M$, is larger than $t_{\text{THRESHOLD}}(M-N-1)$ then we cannot determine which measurement z_k is outlying. In this case, $\hat{\mathbf{P}}$ will be adjusted and the associated UDRE will be increased. If an outlier is identified, downdated estimate will be used to replace $\hat{\mathbf{x}}$ and $\hat{\mathbf{P}}$ (Appendix C). An example of using the Studentized t test for outlier isolation is shown in Figure B.2.

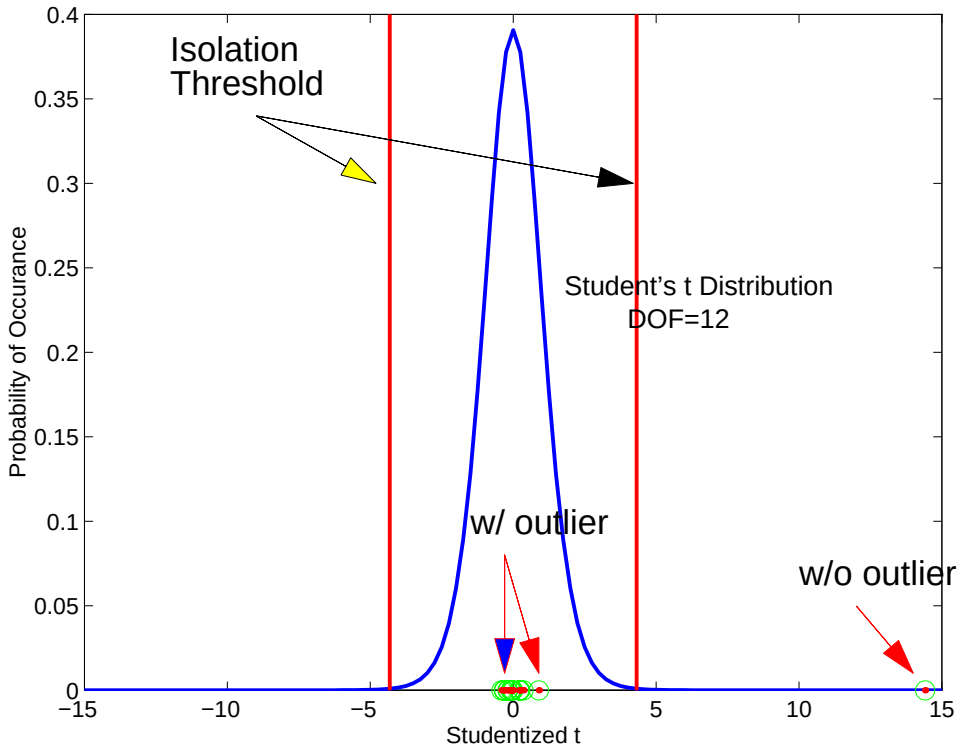

Figure B.2: An Example for Outlier Isolation Using a Studentized t Test

Isolation thresholds for a Student's t distribution are plotted as vertical lines. The number of degrees of freedom is 12 in this example. For a generated estimate which has no outlier, its computed "t" is outside the threshold.

Appendix C

General Formulas For Measurement Downdate

C.1 Introduction

A common practice in fault isolation is to compute the state estimate using only a subset of measurements. We will refer to this as "*measurement downdate*." This is always done after computing state estimate using all the available measurements, this is referred as "*measurement update*." This appendix will derive the general formula which relates measurement update and measurement downdate for the estimated states and covariance matrices. Given an over-determined linear system of equations, the general procedure is to use either least-squares (LS), weighted least-squares (WLS), or minimum variance (MV) to estimate the states and the corresponding covariance matrix. Therefore we will derive the formulas for these different algorithms.

The derivation is aimed at solving the general case, i.e., multiple measurement removal. They can be easily applied to single measurement removal case. In general,

derived formulas in the article have the following advantages:

- multiple measurement removal is possible.
- reduced computational cost by using the results from measurement update .
- easy coding in computer programming languages.

Problem Statement

An over-determined linear system of equations is given as follows

$$\mathbf{z} \;=\; \mathbf{H}\cdot\mathbf{x}+\mathbf{v} \tag{C.1}$$

with measurement noise covariance matrix $\mathbf{R}=E[\mathbf{v}\mathbf{v}^{\mathrm{T}}]$ and the *a priori* information,$\bar{\mathbf{x}}=E[\mathbf{x}]$ and $\bar{\mathbf{P}}=E[(\mathbf{x}-\bar{\mathbf{x}})(\mathbf{x}-\bar{\mathbf{x}})^{\mathrm{T}}]$. Number of measurements is M and number of unknowns is N. Let the state estimate to be $\hat{\mathbf{x}}$ and its covariance to be $\mathbf{P}$ based on all measurements. Now we want to delete m measurements from $\mathbf{z}$ and let the new state estimate to be $\hat{\mathbf{x}}_1$ and its covariance to be $\mathbf{P}_1$. Partition $\mathbf{z}$ into two parts

$$\mathbf{z}=\begin{bmatrix}\mathbf{z}_1\\ \\ \mathbf{z}_2\end{bmatrix}=\begin{bmatrix}\mathbf{H}_1\\ \\ \mathbf{H}_2\end{bmatrix}\cdot\mathbf{x}+\begin{bmatrix}\mathbf{v}_1\\ \\ \mathbf{v}_2\end{bmatrix} \tag{C.2}$$

where $\mathbf{z}_2$ contains the m measurements to be excluded. The *a priori* information, $\bar{\mathbf{x}}$ and $\bar{\mathbf{P}}$, will remain the same.

Assume that measurement noises are independent and uncorrelated such that we can partition the matrix $\mathbf{R}$ as follows:

$$\mathbf{R}=\begin{bmatrix}\mathbf{R}_1 & \mathbf{0}\\ \mathbf{0} & \mathbf{R}_2\end{bmatrix};\;\; \mathbf{R}^{-1}=\begin{bmatrix}\mathbf{R}_1^{-1} & \mathbf{0}\\ \mathbf{0} & \mathbf{R}_2^{-1}\end{bmatrix};$$

We will derive the relationship between $\hat{\mathbf{x}}$ and $\hat{\mathbf{x}}_1$, and the relationship between $\mathbf{P}$ and $\mathbf{P}_1$ for different types of estimation methods.

C.2 Minimum Variance Estimator

The minimum variance estimate, which is equivalent to measurement update in the well-known Kalman filter, can be written as follows:

$$\begin{aligned} \hat{\mathbf{x}} &= \bar{\mathbf{x}} + \bar{\mathbf{P}}\mathbf{H}^{\mathrm{T}}(\mathbf{R} + \mathbf{H}\bar{\mathbf{P}}\mathbf{H}^{\mathrm{T}})^{-1} \cdot (\mathbf{z} - \mathbf{H}\bar{\mathbf{x}}) && \text{(C.3)} \\ &= \bar{\mathbf{x}} + (\bar{\mathbf{P}}^{-1} + \mathbf{H}^{\mathrm{T}}\mathbf{R}^{-1}\mathbf{H})^{-1}\mathbf{H}^{\mathrm{T}}\mathbf{R}^{-1}(\mathbf{z} - \mathbf{H}\bar{\mathbf{x}}) && \text{(C.4)} \\ &= \bar{\mathbf{x}} + \mathbf{K} \cdot (\mathbf{z} - \mathbf{H}\bar{\mathbf{x}}) && \text{(C.5)} \end{aligned}$$

where $\mathbf{K}$ is the Kalman gain matrix. Note that there are two equivalent formulas in expressing the Kalman gain matrix. The covariance matrix after measurement update can be written as follows:

$$\mathbf{P} = (\bar{\mathbf{P}}^{-1} + \mathbf{H}^{\mathrm{T}}\mathbf{R}^{-1}\mathbf{H})^{-1} \quad \text{(C.6)}$$

Measurement downdate, as opposed to measurement update, is to estimate the state $\mathbf{x}$ while taking out some measurements. This is a general procedure during fault isolation.

The new estimate for the reduced system can be described as

$$\begin{aligned} \hat{\mathbf{x}}_1 &= \bar{\mathbf{x}} + (\bar{\mathbf{P}}^{-1} + \mathbf{H}_1^{\mathrm{T}}\mathbf{R}_1^{-1}\mathbf{H}_1)^{-1}\mathbf{H}_1^{\mathrm{T}}\mathbf{R}_1^{-1}(\mathbf{z}_1 - \mathbf{H}_1\bar{\mathbf{x}}) && \text{(C.7)} \\ &= \bar{\mathbf{x}} + \mathbf{P}_1\mathbf{H}_1^{\mathrm{T}}\mathbf{R}_1^{-1}(\mathbf{z}_1 - \mathbf{H}_1\bar{\mathbf{x}}) && \text{(C.8)} \end{aligned}$$

with its covariance matrix

$$\mathbf{P}_1 = (\bar{\mathbf{P}}^{-1} + \mathbf{H}_1^T \mathbf{R}_1^{-1} \mathbf{H})_1^{-1} \tag{C.9}$$

First let us find the relationship between $\mathbf{P}$ and $\mathbf{P}_1$.

$$\mathbf{P} = (\bar{\mathbf{P}}^{-1} + \mathbf{H}^T \mathbf{R}^{-1} \mathbf{H})^{-1} \tag{C.10}$$

$$= (\bar{\mathbf{P}}^{-1} + \mathbf{H}_1^T \mathbf{R}_1^{-1} \mathbf{H}_1 + \mathbf{H}_2^T \mathbf{R}_2^{-1} \mathbf{H}_2)^{-1} \tag{C.11}$$

$$= (\mathbf{P}_1^{-1} + \mathbf{H}_2^T \mathbf{R}_2^{-1} \mathbf{H}_2)^{-1} \tag{C.12}$$

The matrix inversion lemma [Kailath,a] will be used quite frequently in the following derivation. Therefore,

$$\mathbf{P}_1 = (\mathbf{P}^{-1} - \mathbf{H}_2^T \mathbf{R}_2^{-1} \mathbf{H}_2)^{-1} \tag{C.13}$$

$$= \mathbf{P} + \mathbf{P}\mathbf{H}_2^T (\mathbf{R}_2 - \mathbf{H}_2 \mathbf{P} \mathbf{H}_2^T)^{-1} \mathbf{H}_2 \mathbf{P} \tag{C.14}$$

Equation (C.14) has the advantage over equation (C.13) in terms of computational cost because matrix inversion is operated on the one with smaller size, except more matrix multiplication.

The next thing is to find the relationship between $\hat{\mathbf{x}}$ and $\hat{\mathbf{x}}_1$. Using the above equation, we can write

$$\hat{\mathbf{x}} - \bar{\mathbf{x}} = \mathbf{P}\mathbf{H}^T \mathbf{R}^{-1} (\mathbf{z} - \mathbf{H}\bar{\mathbf{x}}) \tag{C.15}$$

$$\hat{\mathbf{x}}_1 - \bar{\mathbf{x}} = \mathbf{P}_1 \mathbf{H}_1^T \mathbf{R}_1^{-1} (\mathbf{z}_1 - \mathbf{H}_1 \bar{\mathbf{x}}) \tag{C.16}$$

Pre-multiplying the above equations by their covariance matrix, we have

$$\begin{aligned} \mathbf{P}^{-1}(\hat{\mathbf{x}} - \bar{\mathbf{x}}) &= \mathbf{H}^{\mathrm{T}}\mathbf{R}^{-1}(\mathbf{z} - \mathbf{H}\bar{\mathbf{x}}) && \text{(C.17)} \\ &= \mathbf{H}_1^{\mathrm{T}}\mathbf{R}_1^{-1}(\mathbf{z}_1 - \mathbf{H}_1\bar{\mathbf{x}}) + \mathbf{H}_2^{\mathrm{T}}\mathbf{R}_2^{-1}(\mathbf{z}_2 - \mathbf{H}_2\bar{\mathbf{x}}) && \text{(C.18)} \\ \mathbf{P}_1^{-1}(\hat{\mathbf{x}}_1 - \bar{\mathbf{x}}) &= \mathbf{H}_1^{\mathrm{T}}\mathbf{R}_1^{-1}(\mathbf{z}_1 - \mathbf{H}_1\bar{\mathbf{x}}) && \text{(C.19)} \end{aligned}$$

The above equations have to be combined and manipulated to yield the following equation

$$\hat{\mathbf{x}}_1 = \hat{\mathbf{x}} - \mathbf{P}_1\mathbf{H}_2^{\mathrm{T}}\mathbf{R}_2^{-1}(\mathbf{z}_2 - \mathbf{H}_2\hat{\mathbf{x}}) \qquad \text{(C.20)}$$

Equations (C.14) and (C.20) summarize the measurement downdate and are the most general form to relate the new and old estimates.

It is not very meaningful to find the relationship between the Kalman gain matrices $\mathbf{K}$ and $\mathbf{K}_1$ since they are not of the same dimension because of measurement removal. It is important to note that the above equation only contains previous estimate and required information of deleted measurement(s).

Special Case, m=1

No matrix inversion is necessary at all for single measurement removal. $\mathbf{H}_2$ is simply an 1xN row vector. z_2 and R_2 are scalars. We have the downdated covariance matrix as follows:

$$\mathbf{P}_1 = \mathbf{P} + \frac{\mathbf{P}\mathbf{H}_2^{\mathrm{T}}\mathbf{H}_2\mathbf{P}}{R_2 - \mathbf{H}_2\mathbf{P}\mathbf{H}_2^{\mathrm{T}}} \qquad \text{(C.21)}$$

and the downdated state estimate

$$\hat{\mathbf{x}}_1 = \hat{\mathbf{x}} - \frac{\mathbf{P}\mathbf{H}_2^{\mathrm{T}}}{R_2 - \mathbf{H}_2\mathbf{P}\mathbf{H}_2^{\mathrm{T}}}(z_2 - \mathbf{H}_2\hat{\mathbf{x}}) \tag{C.22}$$

C.3 Weighted Least-Squares Estimator

With the weighted least-squares approach, neither $\bar{\mathbf{x}}$ nor $\bar{\mathbf{P}}$ is used. Derived equations (C.13) and (C.20) in the previous section can be used without any modifications. However, $\hat{\mathbf{x}}$ and $\mathbf{P}$ is different from previous section and therefore are written below

$$\hat{\mathbf{x}} = (\mathbf{H}^{\mathrm{T}}\mathbf{R}^{-1}\mathbf{H})^{-1}\mathbf{H}^{\mathrm{T}}\mathbf{R}^{-1} \cdot \mathbf{z} \tag{C.23}$$

$$\mathbf{P} = (\mathbf{H}^{\mathrm{T}}\mathbf{R}^{-1}\mathbf{H})^{-1}; \tag{C.24}$$

Note the presence of $\bar{\mathbf{P}}$ has no influence upon the downdated estimate and covariance. For special case when m=1, the formulas required for $\mathbf{P}_1$ and $\hat{\mathbf{x}}_1$ are completely the same as those for minimum variance estimator in equations (C.21) and (C.22).

C.4 Least-Squares Estimator

This is the simplest case. Measurement noise covariance matrix $\mathbf{R}$ is simply replaced by an identity matrix $\mathbf{I}$. Similar to weighted least-squares case, neither $\bar{\mathbf{x}}$ nor $\bar{\mathbf{P}}$ is used. The useful equations are summarized as follows:

$$\hat{\mathbf{x}} = (\mathbf{H}^{\mathrm{T}}\mathbf{H})^{-1}\mathbf{H}^{\mathrm{T}} \cdot \mathbf{z}; \quad \mathbf{P} = (\mathbf{H}^{\mathrm{T}}\mathbf{H})^{-1}; \tag{C.25}$$

$$\mathbf{P}_1 = \mathbf{P} + \mathbf{P}\mathbf{H}_2^{\mathrm{T}}(\mathbf{I} - \mathbf{H}_2\mathbf{P}\mathbf{H}_2^{\mathrm{T}})^{-1}\mathbf{H}_2\mathbf{P} \tag{C.26}$$

$$\hat{\mathbf{x}}_1 = \hat{\mathbf{x}} - \mathbf{P}_1\mathbf{H}_2^{\mathrm{T}}(\mathbf{z}_2 - \mathbf{H}_2\hat{\mathbf{x}}) \tag{C.27}$$

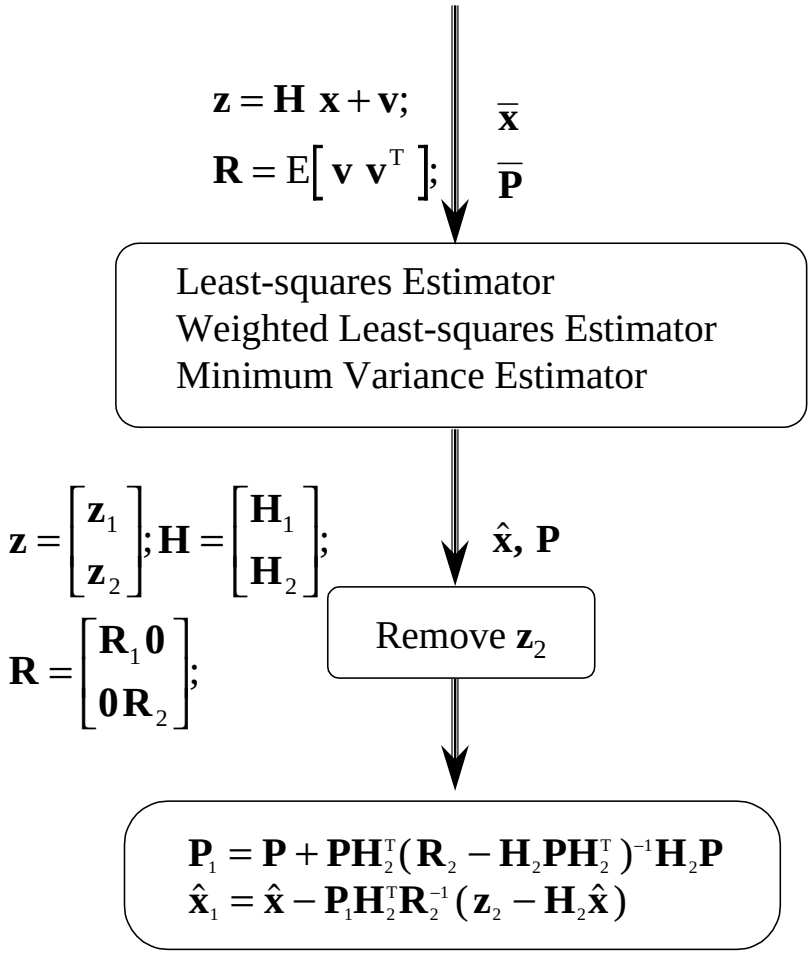

Figure C.1: Measurement Downdate

Special Case, m=1

Again, no matrix inversion is necessary for single measurement removal. $\mathbf{H}_2$ is simply an 1xN row vector. We have the downdated covariance matrix as follows:

$$\mathbf{P}_1 = \mathbf{P} + \frac{\mathbf{P}\mathbf{H}_2^\intercal\mathbf{H}_2\mathbf{P}}{1 - \mathbf{H}_2\mathbf{P}\mathbf{H}_2^\intercal} \tag{C.28}$$

and the downdated state estimate

$$\hat{\mathbf{x}}_1 = \hat{\mathbf{x}} - \frac{\mathbf{P}\mathbf{H}_2^\intercal}{1 - \mathbf{H}_2\mathbf{P}\mathbf{H}_2^\intercal}\left(z_2 - \mathbf{H}_2\hat{\mathbf{x}}\right) \tag{C.29}$$

The above formula agrees with the results in [Pervan].

Appendix D

Coping with Clock and Ephemeris Broadcast

D.1 Introduction

Broadcast ephemeris and clock parameters from GPS satellites are used to compute satellite positions and clock biases [SPS]. About every two hours, a new set of ephemeris and clock parameters are broadcast to the users. Computed satellite position and clock bias using "old" and "new" broadcast parameters could be different. These result in discontinuities in range and range rate corrections. The discontinuities need to be handled in the WAAS generated corrections.

Slow ephemeris and clock corrections (long-term corrections) are sent with an issue of data for ephemeris (IODE). WAAS users have to make sure the IODE used for satellite position computation and the IODE from WAAS broadcast are the same so as to take advantage of the WAAS generated corrections without suffering discontinuities in the range and range rate corrections. The details of how this is handled will be

described in this appendix.

D.2 Satellite Clock Errors

The master station algorithms must ensure the continuity of fast clock corrections during broadcast ephemeris change, especially when the broadcast ephemeris themselves are discontinuous. Satellite clock errors are described in this section.

True satellite clock rate at time t_k can be expressed as follows:

$$\begin{aligned} \dot{B}(t_k) &= \bar{\dot{B}}_{old}(t_k) + \dot{SA}(t_k) + (\Delta a_{f1})_{old}(t_k) \\ &= \bar{\dot{B}}_{new}(t_k) + \dot{SA}(t_k) + (\Delta a_{f1})_{new}(t_k) \end{aligned}$$

where $\bar{\dot{B}}$ is the satellite clock rate computed from GPS broadcast (subframe 1) and $\dot{SA}$ is velocity of SA (fast clock correction). The subscript "old" and "new" stand for previous and current ephemeris or clock broadcast. Slow clock frequency correction (Δa_{f1}) is the WAAS correction for broadcast a_{f1}. Second order and higher terms are neglected since GPS uses atomic clocks. The relationship between $(\Delta a_{f1})_{new}$ and $(\Delta a_{f1})_{old}$ can be written as

$$(\Delta a_{f1})_{new}(t_k) = (\Delta a_{f1})_{old}(t_k) - (\bar{\dot{B}}_{new}(t_k) - \bar{\dot{B}}_{old}(t_k)) \qquad \text{(D.1)}$$

Similarly, true satellite clock error can be expressed as

$$\begin{aligned} B(t_k) &= \bar{B}_{old}(t_k) + SA(t_k) + (\Delta a_{f0})_{old}(t_k) + (\Delta a_{f1})_{old}(t_k - t_o) \\ &= \bar{B}_{new}(t_k) + SA(t_k) + (\Delta a_{f0})_{new}(t_k) + (\Delta a_{f1})_{new}(t_k - t_o) \end{aligned}$$

where (Δa_{f0}) is the slow clock correction. t_o is the time of applicability of the WAAS slow satellite clock error corrections. It is not the t_{oc} and t_{oe} from the GPS satellite broadcast. Again the second order term is neglected because of the stable atomic clocks and constraints on the acceleration of SA.

We can write the relationship between $(\Delta a_{f0})_{new}$ and $(\Delta a_{f0})_{old}$ as

$$\begin{aligned}(\Delta a_{f0})_{new} &= (\Delta a_{f0})_{old} - (\bar{B}(t_k)_{new} - \bar{B}(t_k)_{old}) - \\ &\quad ((\Delta a_{f1})_{new} - (\Delta a_{f1})_{old})(t_k - t_o) \end{aligned} \tag{D.2}$$

The equation above can be further simplified to

$$(\Delta a_{f0})_{new} = (\Delta a_{f0})_{old} - (\bar{B}(t_k)_{new} - \bar{B}(t_k)_{old}) \tag{D.3}$$

because $((\Delta a_{f1})_{new} - (\Delta a_{f1})_{old}$ is small enough to be neglected.

D.3 Satellite Ephemeris Errors

Similar to the approach in dealing with satellite clock errors, we can express satellite ephemeris rate as follows:

$$\begin{aligned}\dot{\mathbf{R}}(t_k) &= \bar{\dot{\mathbf{R}}}_{old}(t_k) + \Delta\dot{\mathbf{R}}_{old}(t_k) \\ &= \bar{\dot{\mathbf{R}}}_{new}(t_k) + \Delta\dot{\mathbf{R}}_{new}(t_k)\end{aligned}$$

where $\bar{\dot{\mathbf{R}}}$ is satellite's velocity computed from broadcast ephemeris (new or old) and $\Delta\dot{\mathbf{R}}$ is the ephemeris error rate. Again only the first order effect is considered in the

derivation. From the above equation, we have

$$\Delta\dot{\mathbf{R}}_{new}(t_k) = \Delta\dot{\mathbf{R}}_{old}(t_k) + \dot{\mathbf{R}}_{old}(t_k) - \dot{\mathbf{R}}_{new}(t_k) \tag{D.4}$$

To correct for ephemeris errors, satellite position is expressed as follows.

$$\begin{aligned} \mathbf{R}(t_k) &= \mathbf{R}_{old}(t_k) + \Delta\mathbf{R}_{old}(t_k) \\ &= \mathbf{R}_{new}(t_k) + \Delta\mathbf{R}_{new}(t_k) \end{aligned}$$

Therefore,

$$\Delta\mathbf{R}_{new}(t_k) = \Delta\mathbf{R}_{old}(t_k) + (\mathbf{R}_{old}(t_k) - \mathbf{R}_{new}(t_k)) \tag{D.5}$$

Bibliography

[AIAAGPS] B.W. Parkinson and J.J. Spilker, *Global Positioning System:Theory and Applications*, AIAA Publication, 1996.

[Bevington] P. R. Bevington and D. K. Robinson, *Data Reduction And Error Analysis For The Physical Sciences*, 2nd Ed., McGraw-Hill, 1992.

[Bierman] Gerald J. Bierman, *Factorization Methods for Discrete Sequential Estimation*, Academic Press, 1977.

[Boguslavskij] I.A. Boguslavskij,*Filtering and Control*, Optimization Software, Inc., 1988.

[Bower] R.E. Bower and G.L. Dieter,"GPS Navigation Payload Scheduled Maintenance: An Explanation of Satellite Outage Time," Proceedings of ION-GPS 95, pp. 233-239, Palm Springs, CA., Sept. 12-15, 1995.

[Braasch] M.S. Braasch, "Multipath Effects," Chapter 14 of Global Positioning System: Theory and Applications, Volume I, edited by B.W. Parkinson and J.J. Spilker, AIAA Publications, 1996.

[Brown] R.G. Brown, *Introduction to Random Signal Analysis and Kalman Filtering*, John Wiley & Sons, Inc., 1983.

[Bryson] A.E. Bryson, "Optimal Control and Estimation," E207C Classnotes, Spring Quarter, 1994, Stanford University.

[Ceva] J. Ceva, W. Bertiger, R. Mullerschoen, T. Yunck and B. Parkinson, "Incorporation of Orbital Dynamics to Improve Wide-Area Differential GPS," Proceedings of ION-GPS 95, Palm Springs, CA., Sept. 12-15, 1995.

[Chao,a] Y.C. Chao, Y.J. Tsai, T. Walter, C. Kee, et.al., "The Ionospheric Delay Model Improvement for the Stanford WAAS Network," Proceedings of ION National Technical Meeting 95, Anaheim, CA., Jan. 18-20, 1995.

[Chao,b] Y.C. Chao, Y.J. Tsai, T. Walter, C. Kee, et.al., "An Algorithm for Interfrequency Bias Calibration and Application to WAAS Ionosphere Modeling," Proceedings of ION-GPS 95, Palm Springs, CA., Sept. 12-15, 1995.

[Chao,c] Y.C. Chao, S. Pullen, P.K. Enge, B.W. Parkinson, "Study of Ionospheric Integrity," Proceedings of ION-GPS-96, Kansas City, Missouri, September, 1996.

[Chao,d] Yi-Chung Chao, *Real Time Implementation of the Wide Area Augmentation System for the Global Positioning System with an Emphasis on Ionospheric Modeling,* Ph.D. Dissertation, Stanford University, June 1997.

[Chou] H. Chou, *An Adaptive Correction Technique For Differential Global Positioning System,* Ph.D. Dissertation, Stanford University, June 1991.

[Colombo] O. L. Colombo, "The Dynamics of Global Positioning System Orbits and the Determination of Precise Ephemeris," J. of Geophysical Research, vol.94, No.B7, July 1989.

[Comp] C. Comp, R. Gazit, T. Walter and P. Enge, "Improving WAAS Integrity And Availability: UDRE And GIVE Time Update," Proceedings of ION-GPS 97, p.p. 1315-1324, Kansas City, MI, Sept. 16-19, 1997.

[Crum] J.D. Crum, R.T. Smetek, "Welcome to the Machine: An Overview of GPS Master Control Station Anomaly Detection and Resolution Techniques," Proceedings of ION-GPS 96, p.p. 211-231, Kansas City, MI, Sept. 17-20, 1996.

[Dai] D. Dai, T. Walter, C.J. Comp, Y.J. Tsai, P.Y. Ko, P.K. Enge and J.D. Powell, "High Integrity Multipath Mitigation Techniques for Ground Reference Stations," Proceedings of ION-GPS 97, Kansas City, Missouri, Sept. 16-19, 1997.

[DoDOrbit] J. O'Toole and M. Merrogan, "Evaluation of DoD GPS Satellite Orbits Using NASA Laser Ranging Data," Proceedings of ION-GPS 95, pp. 45-54, Palm Springs, CA., Sept. 12-15, 1995.

[Enge,a] P.K. Enge, "The Global Positioning System: Signals, Measurements and Performance," The International Journal on Wireless Information Networks, March, 1994.

[Enge,b] P.K. Enge and A.J. Van Dierendonck, "The Wide Area Augmentation System," Proceedings of the Eighth International Flight Inspection Symposium, Denver, June 1994.

[Enge,c] P.K. Enge, "WAAS Messaging System: Data Rate, Capacity, and Forward Error Correction," Navigation, Vol.44, No.1, Spring 1997.

[FRP1992] Anonymous, *1992 Federal Radionavigation Plan*, Published by Department of Transportation and Department of Defense, 1992.

[Fuller] R.A. Fuller, T. Walter, S. Houck and P. Enge, "Flight Trials of a Geostationary Satellite Based Augmentation System at High Latitude and Dual Satellite Coverage," Proceedings of the ION National Technical Meeting, San Diego, CA, January 1999.

[Gelb] A. Gelb, editor, *Applied Optimal Estimation*, M.I.T. Press, 1974.

[Hansen,a] A. Hansen, Y.C. Chao, T. Walter and P. Enge, "Ionospheric Correction Using Tomography," Proceedings of ION National Technical Meeting, Santa Monica, CA, January. 16-19, 1997.

[Hansen,b] A. Hansen, T. Walter and P. Enge, "Ionospheric Correction Using Tomography," Proceedings of ION-GPS 97, Kansas City, Missouri, Sept. 16-19, 1997.

[Hegarty] C.J. Hegarty, "Optimal Differential GPS for a Data Rate Constrained Broadcast Channel," Proceedings of the Sixth International Technical Meeting of the Satellite Division of the Institute of Navigation, Salt Lake City, pp. 1527-1535, September 1993.

[IGS] Annonymous, "Resource Information," International GPS Service For Geodynamics, January 1997.

[JHU] Annonymous, "GPS Risk Assessment Study," Applied Physics Laboratory, The John Hopkins University, January 1999.

[JPL] T.P. Yunck, Y.E. Bar-Sever, W.I. Bertiger, B.A. Iijima, S.M. Litchen, U.J. Lindqwister, A.J. Mannucci, R.J. Muellerschoen, T.N. Munson L. Romans, and S.C. Wu, " A Prototype WADGPS System for Real Time Sub-Meter Positioning

Worldwide," Proceedings of ION-GPS 96, p.p. 1819-1826, Kansas City, MI, Sept. 17-20, 1996.

[Kailath,a] T. Kailath, *Linear Systems*, Prentice-Hall, Englewood Cliffs, N.J., 1980.

[Kailath,b] T. Kailath, *Lectures On Wiener And Kalman Filtering*, Spring-Verlag, New York, 1981.

[Kaplan] E.D. Kaplan, *Understanding GPS: Principles and Applicaions*, Artech House, 1996.

[Kee,a] C. Kee, B.W. Parkinson, and P. Axelrad, "Wide Area Differential GPS," Navigation, Journal of the U.S. Institute of Navigation, vol. 38, no. 2, Summer 1991.

[Kee,b] C. Kee, *Wide Area Differential GPS*, Ph.D. Dissertation, Stanford University, December 1993.

[Kee,c] C. Kee, T. Walter, Y.C. Chao, Y.J. Tsai, et.al., "Comparison of Full Vector and Common View WAAS Algorithms," Proceedings of the Annual Meeting of the Institute of Navigation, Colorado Springs, June 1995.

[Kelly] R.J. Kelly and J.M. Davis, "Required Navigation Performance (RNP) for Precision Approach and Landing GNSS Application," Navigation, Journal of the Institute of Navigation, Vol.41, No.1, Spring 1994, pp.1-30.

[Klobuchar] J.A. Klobuchar, "Ionospheric Effects on GPS," Chapter 12 of Global Positioning System: Theory and Applications, Volume I, edited by B.W. Parkinson and J.J. Spilker, AIAA Publications, 1996.

[Lala] J. Lala and L. Burkhardt, "GPS Operational Control System Modernization: Alternative Architectural Concepts," Proceedings of ION-GPS 96, pp. 449-459, Kansas City, MI, Sept. 17-20, 1996.

[Lawrence] D.G. Lawrence, "Aircraft Landing Using GPS," Ph.D. Dissertation, Stanford University, September 1996.

[Litchen] S. M. Lichten and J. S. Border, "Strategies for High Precision Global Positioning System Orbit Determination," Journal of Geophysical Research, Vol.92, No.B12, pp.12.751-12,762, Nov. 1987.

[Luenberger] D.G. Luenberger, *Optimization by Vector Space Methods*, John Wiley & Sons, Inc., 1969.

[Matchett] G. Matchett, "Stochastic Simulation of GPS Selective Availability," TM, FAA Contr. DTRS-57-83-C-00077, June 1985.

[McCaskill] T.B. McCaskill, W.G. Reid, O.J.Oaks, R.L. Beard, J.A. Buisson and H.E. Warren, "Performance of GPS Monitor Station Time Reference And On-board NAVSTAR Clock," Proceedings of ION-GPS 95, pp. 241-249, Palm Springs, CA., Sept. 12-15, 1995.

[Mitre] M.B. El-Arini, P.A. O'Donnell, P.M. Kellan, J.A. Klobuchar, T.C. Wisser and P.J. Doherty, "The FAA Wide Area Differential GPS(WADGPS) Static Ionospheric Experiment," Proceedings of the 1993 National Technical Meeting of the Institute of Navigation, San Francisco, January 1993.

[MOPS] Anonymous, "'Minimum Operational Performance Standards For Global Positioning System/Wide Area Augmentation System Airborne Equipment,' RTCA Document No. RTCA/DO-229A, June 8, 1998

[Neter] J. Neter, W. Wasserman and M.H. Kutner, *Applied Statistical Models*, Third Edition, Irwin, INC. 1990.

[Parkinson] B. W. Parkinson, "Differential GPS," Chapter 1 of Global Positioning System: Theory and Applications, Volume II, edited by B.W. Parkinson and J.J. Spilker, AIAA Publications, 1996.

[Pervan] B. Pervan, *Navigation Integrity for Aircraft Precision Landing Using the Global Positioning System*, Ph.D. Dissertation, Stanford University, March 1996.

[Pogorelc] S. Pogrelc, M. Lorenz, K. Murdock, B. Harding,T. Cashin and D. Kraus, "National Satellite Testbed (NSTB) GPS Satellite Clock/Ephemeris Determination Analysis and Results," Proceedings of ION-GPS 95, p.p. 247-256, Palm Springs, CA, Sept. 12-15, 1995.

[Pullen] S. Pullen, P.K. Enge and B.W. Parkinson, "A New Method for Coverage Prediction for the Wide Area Augmentation System (WAAS)," Proceedings of the Annual Meeting of the Institute of Navigation, Colorado Springs, June 1995.

[Spilker,a] J.J. Spilker Jr., "GPS Signal Structure and Theoretical Performance," Chapter 3 of Global Positioning System: Theory and Applications, Volume I, edited by B.W. Parkinson and J.J. Spilker, AIAA Publications, 1996.

[Spilker,b] J.J. Spilker Jr., "Tropospheric Effects on GPS," Chapter 13 of Global Positioning System: Theory and Applications, Volume I, edited by B.W. Parkinson and J.J. Spilker, AIAA Publications, 1996.

[Studenny] Studenny, J., "Simulation of a Second-Order Gauss-Markov Process," RTCA Paper No.148-93/SC159-424, March 17, 1993.

[SolarP] H. Fliegel, T. Gallini and E. Swift, "Global Positioning System Radiation Force Model for Geodetic Applications," J. Geophysical Research, vol.97, No.B1, January 1992.

[SPS] Anonymous,"Global Positioning System Standard Positioning Service Signal Specification," 2nd Edition, June 2, 1995.

[Swider] R. Swider, D. Miller, A. Shakarian, S. Flannigan and J. Fernow, "Development of Local Area Augmentation System Requirements," Proceedings of ION-GPS 96, pp. 35-49, Kansas City, MI, Sept. 17-20, 1996.

[Tsai,a] Y. Tsai, Y. Chao, T. Walter, C. Kee, D. Powell, P. Enge and B. Parkinson, "Evaluation of Orbit and Clock Models for Real Time WAAS," Proceedings of the National Technical Meeting of the Institute of Navigation, Anaheim, CA, pp. 539-547, January 1995.

[Tsai,b] Y. Tsai, P. Enge, Y. Chao, T. Walter, C. Kee, J. Evans, A. Barrows, D. Powell and B. Parkinson, "Validation of the RTCA Message Format for WAAS," Proceedings of ION GPS 95, pp. 661-670, Palm Springs, CA, Sept. 12-15, 1995.

[Tsai,c] Y. Tsai, T. Walter, P. Enge, "Integrity Monitoring for WAAS Clock/Ephemeris Error Estimation," Proceedings of ION-GPS 97, Kansas City, Missouri, Sept. 16-19, 1997.

[TSOC129a] Anonymous, "Technical Standard Order-C129a, Airborne Supplemental Navigation Equipment Using global Positioning System (GPS)," Federal Aviation Administration, Department of Transportation, Feb. 20, 1996.

[van Graas] F. van Graas amd M.S. Braasch, "Selective Availability," Chapter 17 of Global Positioning System: Theory and Applications, Volume I, edited by B.W. Parkinson and J.J. Spilker, AIAA Publications, 1996.

[Walter,a] T. Walter, C. Kee, Y.C. Chao, Y.J. Tsai, et.al., "Flight Trials of the Wide Area Augmentation System (WAAS)," Proceedings of ION-GPS 94, Salt Lake City, Utah, Sept. 22-24, 1994, pp.1245-1254.

[Walter,b] T. Walter and P. Enge, "Weighted RAIM for Precision Approach," Proceedings of ION-GPS 95, Palm Springs, CA, Sept. 12-15, 1995.

[WG2] "Wide-Area Augmentation System Signal Specification," RTCA Special Committee 159 Working Group 2, March 1994.

[Wullschleger] V.T. Wullschleger, D.G. O'Laughlin and F.M. Haas, "FAA Flight Test Results for GPS Wide Area Augmentation System (WAAS) Cross Country Demonstration," Proceedings of the 50^{th} Annual Meeting of the Institute of Navigation, June 6-8, 1994.

[Zumberge] J.F. Zumberge and W.I. Bertiger, "Ephemeris and Clock Navigation Message Accuracy," Chapter 16 of Global Positioning System: Theory and Applications, Volume I, edited by B.W. Parkinson and J.J. Spilker, AIAA Publications, 1996.